

Max-Planck-Institut für Biochemie
Abteilung für Membran- und Neurophysik
Arbeitsgruppe Hermann Heumann

Time-Resolved Small Angle Scattering of Proteins

The structural intermediates of the Chaperonin GroEL and GroES upon ATPase cycle

Manfred Rössle

Vollständiger Abdruck der von der
Fakultät für Physik der Technischen Universität München
zur Erlangung des akademischen Grades eines

Doktors der Naturwissenschaften

(Dr. rer. nat)

genehmigten Dissertation.

Vorsitzender: Univ.-Prof. Dr. J. L. van Hemmen

Prüfer der Dissertation: 1. Univ.-Prof. Dr. E. Sackmann

2. Univ.-Prof. Dr. P. K. Böni

Die Dissertation wurde am 30.01.2001 bei der
Technischen Universität eingereicht und durch die
Fakultät für Physik am 30.05.2001 angenommen.

for Silvia & Leo

You are under the impression,
that when your a walking forward
then you end up further onward
but things ain't quite that simple

The Who from "Quadrophenia"

CONTENTS

1. Introduction	5
1.1 Molecular Motors and Working Proteins	5
1.2 Cooperative Control of Protein Activity	6
1.3 Time-Resolved Experiments: Dynamics vs. Steady State	6
2. The molecular Chaperones	8
2.1 Protein Folding	8
2.2 The Concept of Chaperone Mediated Protein Folding	8
2.3 The Chaperonin System GroE from <i>E.coli</i>	10
3. Time Resolved Small Angle Scattering of Proteins	15
3.1 Small Angle X-ray Scattering	15
3.2 Beamlines for Small Angle Scattering	17
3.3 The Stopped Flow Device	21
3.4 The Radiation Damage Problem	23
3.5 Model calculations	24
3.6 Detectors for Time-Resolved Small Angle Scattering	26
3.6.1 Gas-filled Detectors	26
3.6.2 X-ray CCD detector	27
3.6.3 Image plates	28
4. Data Reduction, Treatment and Analysis	30
4.1 Small Angle Scattering Data	30
4.2 Error Estimation	35
5. Sample Preparation	37
5.1 Bacteria Growing and Protein Purification	37
5.2 Control of the Protein Purity	37
5.3 Control of the Protein Activity	38
6. Results	40
6.1 The main Chaperonin GroEL nucleotide cycle - without GroES	44
6.1.1 GroEL mixed with ADP	44
6.1.2 GroEL mixed with ATP	48
6.2 The GroEL-GroES nucleotide cycle	55
6.2.1 Formation of the asymmetric GroEL-GroES complex	55
6.2.2 Dynamics of the asymmetric GroEL-GroES complex in the presence of ATP	64

6.3	Time-Resolved Small Angle Neutron Scattering - First Results	69
7.	<i>Discussion</i>	71
7.1	Time Resolved Small Angle Scattering - A Proper Method for Protein Kinetics and Dynamics?	71
7.1.1	Short Times, Low Contrast and a Lot of Photons: Time Resolved Small Angle X-ray Scattering	71
7.1.2	Short Times, High Contrast and Dripping Neutrons: Time Resolved Small Angle Neutron Scattering	72
7.2	The ATP-ase Activity of GroEL	73
7.2.1	Allosteric Effect of the Cooperative ATP Binding	73
7.2.2	Comparison of the Small Angle Scattering Data for the GroEL-ATP Complex with Structures from X-ray Crystallography and Electron Microscopy	75
7.3	The GroEL-GroES nucleotide cycle	76
7.3.1	Asymmetric binding of the GroES in the presence of ADP	76
7.3.2	The Chaperonin Two-Stroke Mechanism and its Structural Intermediates	77
7.3.3	Functional Relevance of the Intermediate GroEL-GroES-Nucleotide Complexes	80
8.	<i>Conclusions and Summary</i>	83
8.1	Time-Resolved Small Angle Scattering: Kinetic and Structural Data from Proteins in Solution	83
8.2	The Chaperonin "two-stroke" Engine at Work	84
9.	<i>Outlook</i>	87
	<i>Appendix</i>	95

1. INTRODUCTION

Working proteins. Time Scale of Biological Processes. Allosteric Effect. Cooperativity and Concerted Movements. Dynamics and Kinetics vs. Steady State. Time resolved methods for investigation of kinetics and dynamics.

1.1 Molecular Motors and Working Proteins

The machines of life are the proteins. These molecules are involved in all the processes and reactions inside a living organism. Dependent on their function and tasks, proteins can be classified into two major groups: Firstly the structure proteins, which are responsible for the formation of passive overall structures such as hair fibres or the cytoskeleton of the cell. The second group are function related proteins, which facilitate the cell metabolism and regulation. Each protein has at least one three dimensional structure in which it is stable and active under biological conditions. However, proteins are no rigid bodies, and the stable protein structure can be transformed to other stable states[1, 2]. The transition between the distinct protein conformations is induced thermal or by specific binding of ligands or substrates, whereas several structural intermediates can be passed through. The protein can perform work if energy is released by these processes. This protein dynamics occur on different time scales with different spatial extents. The different parameters of protein movements are listed in tab. 1.1

Motion	Spatial extent (Å)	Characteristic time scale (s)
Vibrations of bonded atoms	2-5	$10^{-14} - 10^{-13}$
Elastic vibration of globular regions	10-20	$10^{-12} - 10^{-11}$
Rotation of sidechains at surface	5-10	$10^{-11} - 10^{-10}$
Relative motions of globular regions	10-20	$10^{-10} - 10^{-7}$
Allosteric transitions	5-50	$10^{-4} - 10^0$
Protein folding		$10^{-5} - 10^1$

Tab. 1.1: The spatial extent and the time scales of movements which occur in proteins. (adapted from S. Cusack in [3])

A special group of function related proteins are motor proteins. In contrast to enzymes, which catalyze chemical reactions, working or motor proteins are able to provide mechanical energy. These molecules bind nucleoside-triphosphate (NTP) and converts it into nucleoside-diphosphate (NDP) by hydrolysis of one phosphate. The released energy is used for a processive or continuous motions[4, 5]. During this processive motion mechanical work can be performed. The more general term working protein is used, if the protein can provide mechanical work, but the motion itself is rather stepwise than continuous[6].

If the transition between the stable protein states requires a cascading process with several structural intermediates, a regulatory process has to be introduced. The simplest regulation is obtained by binding of ligands to the protein, which introduce the transition between the inactive and the active conformation. The ligand acts for the transition inactive \rightarrow active conformation as an activator, while it can also act as an inhibitor for the conversion from the active state to the inactive state. This regulation process is possible for monomeric proteins with one ligand binding site. If the protein is assembled from several identical subunits, a more complicated process takes place. An allosteric regulation process is introduced into a multi-meric protein, if every subunit of the protein can bind the ligand, but the whole protein multi-mer is only functional if all the subunits have bound the ligand. This allosteric regulation is often achieved by a special kinetics of the ligand binding[7, 8].

1.2 Cooperative Control of Protein Activity

As mentioned above, allosteric regulation is found in multi-meric protein assemblies. If these proteins provide more than one ligand binding site, but all binding sites have to bind the ligands before the whole protein is converted into the active state, a regulatory scheme is needed. An allosteric regulation scheme was proposed 1965 by Monod, Wyman & Changeux[9]. The main feature of this allosteric protein activity regulation is the enhancing of the affinity for ligand binding after the first ligand is bound. This behavior is called **cooperative** binding of ligands. The inversion of this behavior, where the binding of a ligand inhibits the binding of other ligands, is called negative or **anti-cooperativity**. In large protein assemblies, consisting of several subunits, the allosteric regulations can cause large conformational changes even over the whole protein[10]. In addition, cooperative and anti-cooperative behavior can occur at the same protein using the same ligand. In this reactions the cooperative binding favors subunits to bind the ligand (which are forced in the tense T-state), while it inhibits ligand binding on the other subunits (which stay in the relaxed R-state)[10]. The biological advantage of allosteric regulation is, that no additional control mechanism for the ligand is needed, because structural changes of the protein upon ligand binding control the reaction. The transition between the T- and the R-state can occur concerted, sequentially or a combination of both. Since the analysis of cooperative and allosteric protein activity gives insights into the reaction mechanism and its regulation scheme, the investigation of these processes is of major interest in biophysics and biochemistry.

The investigation of cooperative protein kinetics is often carried out by steady state methods. For instance, the steady state formation rate of molecules in the T-state at different ligand concentrations is measured. From this analysis the Hill coefficient, a parameter for cooperative ligand binding can be obtained. For the investigation of systems far from equilibrium, where the steady state assumptions are no longer valid, transient-state kinetics can be measured. For the analysis of a transient reaction mechanism, time-resolved techniques have to be used. If the transient intermediates can be identified by a structural signal, rate constants can be derived very simply, and direct informations about the protein structure upon the reaction cycle can be obtained.

1.3 Time-Resolved Experiments: Dynamics vs. Steady State

Protein structures can be analyzed with high resolution by several methods. X-ray crystallography or the nuclear magnetic resonance (NMR) methods are able to give insights in the Å-regime of a protein, while electron-microscopy (EM) provides a resolution of about 10-20Å. A lot of structural

and functional information of the "work" of proteins was obtained by these methods. The advantage of these high resolution techniques is to characterize the stable conformation of proteins, for instance the starting conformation before the reaction starts and the end conformation after the reaction is finished. But time-resolved methods have to be used in order to trace the reaction between the two conformations. Tab. 1.1 shows that the conformational changes of proteins can occur on different time scales and spatial extents. For the investigation of these structural changes capable time-resolved methods such as time-resolved crystallography, NMR or cryo-EM have to be chosen. However, these techniques are restricted to several experimental parameters such as the size of the protein, time scale of the reaction and the triggering of the reaction[11, 12]. For instance, time-resolved Laue crystallography monitors conformational changes in the ns time range with atomic resolution[13, 14], but is restricted to smaller proteins. In electron microscopy larger molecules can be investigated[15, 16], but the proteins have to be frozen after starting the reaction[17]. At least NMR provides time-dependent structural changes in detail, but it is also restricted to small proteins[18].

Time-resolved small angle scattering (TR-SAS) is a scattering method, where the proteins can be investigated in solution[19, 20, 21, 22]. As small angle scattering is a solution method, the environmental conditions can be changed very easily by simply mixing two reactants together. The disadvantage of scattering in solution is the reduced resolution, which limits the method to large proteins. The development of synchrotrons, providing a high flux of high energy X-ray photons, shifts the time resolution of small angle scattering into the 100ms time range. Therefore, time-resolved small angle X-ray scattering (TR-SAXS), using synchrotron radiation, is a method for the investigation of structural changes of large protein assemblies if the changes occur in the 1s time scale[19, 22].

It is the aim of this work, firstly to explore the applicability of time-resolved small angle X-ray scattering for the investigation of transient protein kinetics, and secondly to trace the reaction cycle and interplay of two proteins of the chaperonin system GroE of *E. coli* under ATP conditions.

2. THE MOLECULAR CHAPERONES

Protein folding. Folding of proteins supported by chaperonins. The chaperonin system GroE. The two stroke motor. ATPase cycle of the system. Dynamics of binding denatured proteins. Structure and functional implications

2.1 Protein Folding

One of the most fascinating processes of biochemistry is the folding of proteins. In this process the at first one-dimensional chain of amino acids is folded into a three dimensional conformation, which is unique for the protein function[23]. For this folding reaction a hierarchical, multi-step process can be proposed. In the first step, parts of the primary one-dimensional polypeptide chain are converted into secondary structural elements such as α -helices and β -sheets. Since these secondary structural elements are connected by flexible loop regions, α -helices and β -sheets can form particular protein domains. The final tertiary structure of the protein is assembled out of these domains. During the folding reaction more and more different inner molecular bonds (e.g. H- and salt-bridges) are formed and the folding energy is reduced. The one-dimensional polypeptide chain is in a state of high energy, whereas the folding intermediates are in a state of lower energy. Thus the protein folding is a spontaneous process.

This view is true for protein folding *in vitro*, but *in vivo* protein-protein interaction, which may disturb the spontaneous folding reaction, has to be taken into account. In *vivo*, proteins are synthesized at the ribosomes, which are located in the cytoplasm of a cell. For the metabolic pathway of the organism a various number of protein has to be synthesized simultaneously. For instance, an *E. coli* cell produces 1000 polypeptide chains of an averaged molecular weight of 40 kDa within one second[24, 25, 26]. This huge number results in a protein concentration of about 300mg/ml[27]. At this high protein concentration, interferences of non-folded or partly folded proteins are possible and would lead to non-functional protein aggregation[28, 26]. In order to avoid this unproductive dead-end in protein synthesis in all three kingdoms of life: eubacteria, procaryotic bacteria and archae bacteria, helper proteins assist the protein folding, if needed[29, 30, 31, 32]. The function of these helpers is, firstly to bind to the unfolded nascent polypeptide chain to prevent protein aggregation and secondly to facilitate their folding or re-folding. Since the helper proteins for the assisted protein folding bind to proteins in *statu nascendi*, they are called "molecular chaperones".

2.2 The Concept of Chaperone Mediated Protein Folding

Molecular chaperones are a class of unrelated families of proteins with the common ability to bind to any hydrophobic surface of other proteins to prevent protein aggregation. A second common feature of the chaperones is, that the binding of a denatured protein as a substrate to the chaperon is not restricted by the sequence, or the mass of the substrate protein[33, 34].

As described above, the protein folding in the cell often needs assistance. For instance the protein folding in eubacteria such as *E. coli*, is facilitated by two different groups of molecular chaperones. These two groups are, firstly chaperones of the DnaK/DnaJ family and secondly the proteins GroEL and GroES belonging to the chaperonin subfamily. These two groups show a cascading interplay during the chaperone mediated protein folding, where newly synthesized proteins are consigned from one group of chaperones to the other group. This folding cascade is shown in the next figure (fig. 2.1 left).

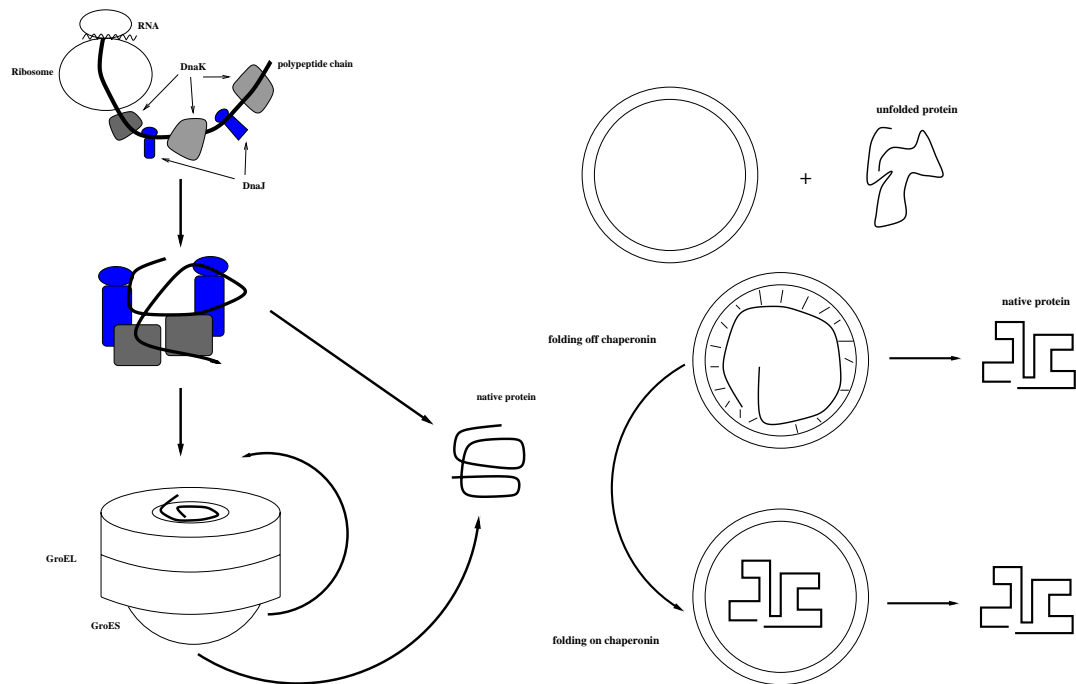


Fig. 2.1: Interplay of the chaperones. While specialized chaperones bind to the nascent polypeptide chain the chaperonin (GroEL-GroES) binds the newly synthesized protein only if the spontaneous re-folding fails. The re-folding of the protein can occur in the GroEL barrel (on chaperonin), as well as after the release of the completely unfolded protein in the surrounding (off chaperonin).

The chaperones of the DnaK/DnaJ group bind the protein while the polypeptide chain grows from the ribosome, and prevent the chain from aggregation. After the DnaJ/DnaK proteins are dissociated the, now fully synthesized, polypeptide chain can fold into the native conformation. The chaperonins GroEL/GroES are only involved, if this spontaneous folding fails. For the re-folding of the bound protein two possible pathways are proposed (see fig. 2.1 right). Firstly on the chaperone, where the chaperonin allows the protein to fold without interference with other proteins in the barrel, like in an "Anfinsen-cage"[35, 36, 37]. The second possible pathway is off the chaperone, where the protein is released fully unfolded and can re-fold spontaneously. These two pathways of protein re-folding are strongly dependent on the substrate protein, but the general parameters of the on or off chaperon re-folding are not quite clear yet.

A second task of the chaperonins is the protection of the cell from protein aggregation due to thermal or chemical stress[38]. Proteins are sensitive to denaturation by heat or chemicals. Denatured proteins show hydrophobic patches on their surface which would lead to protein aggregation. As in the folding cascade of newly synthesized proteins, the chaperonins bind to these hydrophobic sites,

avoiding protein aggregation by coverage of these patches, and facilitate the re-folding of the denatured, mis-folded protein.

In the assisted folding process, the substrate protein might have to bind and dissociate several times until it is folded in the native state[39]. It is known that no external energy is necessary for the re-folding of some substrate proteins, but the re-folding rate is very slow in this case. The barrel like chaperonins show an ATPase activity, and the re-folding rate of substrate proteins is increased in the presence of ATP[40]. Co-factors such as the GroES are also found to cause significant changes to the chaperonin re-folding process.

The subunits of the GroEL show a remarkable interplay between cooperativity and anti-cooperativity during their reaction cycle[41, 42]. Therefore the investigation of the reaction cycle by time resolved methods leads to a better understanding of the protein folding process as well as in the, maybe common, ATPase regulatory mechanism of the chaperonin mediated protein re-folding[43, 44, 45]. Since the ATPase reaction cycle was found to be in the sub-second time range, and the conformational changes of the chaperonin upon nucleotide binding and hydrolysis are proposed to be large, time resolved small angle scattering is the method of choice.

2.3 The Chaperonin System GroE from *E.coli*

The chaperonin system of the eubacteria *E. coli* are called GroEL and GroES. This special group of helper proteins was found as part of the heat-shock response of bacteria cells[46, 47, 48]. The proteins are mainly expressed during the heat-shock, but are also found in normal growing cells[49, 50]. Further investigations have shown that the main chaperonin GroEL is a hollow cylindrically shaped molecule, consisting of two heptameric rings. The rings are build of seven identical subunits with a molecular weight of 57 kDa. These two rings bind back to back to each other and form the GroEL cylinder[51]. The crystallographic structure[52] of the GroEL is shown in figure 2.2. The GroEL subunit can be divided into three domains, with different properties and tasks.

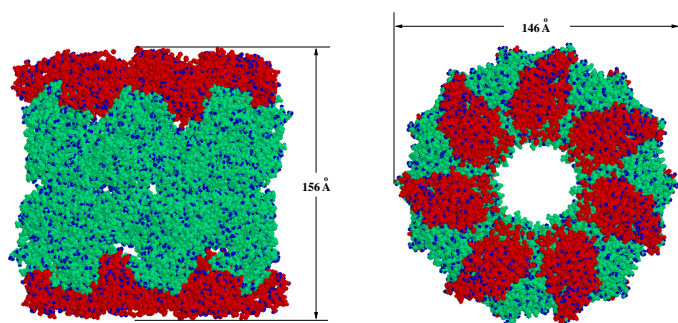


Fig. 2.2: The main chaperonin GroEL from the crystal structure. The hole in the middle has a diameter of 45Å. The C- and N-terminal ends of the amino acid chains were not resolved by crystallography.

The apical domain (highlighted red in fig 2.3 left) is the binding site for substrate proteins, and for GroES. This domain shows a high flexibility and can bind any protein with hydrophobic patches[53, 54, 55]. The domain is flexible within the domain itself, as well as flexible for en-block movements of the whole domain[55]. For the en-block movements small regions between the apical domain and the

intermediate domain (highlighted blue in fig. 2.3), and at the junction of the intermediate-equatorial domain, act as hinges.

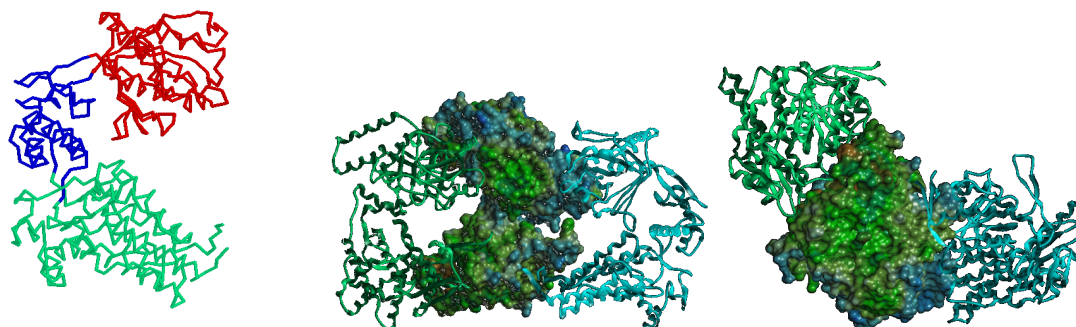


Fig. 2.3: Three domain model (left) and surface hydrophobicity of the GroEL subunits (middle and right). The inner surface of the subunit is highly hydrophobic in order to bind the substrate protein (middle). The bottom of the equatorial domain is also highly hydrophobic to facilitate the interring binding (right).

The equatorial domain (highlighted green in fig. 2.3) is the largest domain of the GroEL subunit. This domain provides the binding sites for the other subunits to form the GroEL heptameric ring. It also facilitates the formation of the whole GroEL cylinder by appropriate the ring to ring interactions. It also contains the nucleotide binding site. The inner wall of the GroEL ring shows a rather high hydrophobic surface (see fig. 2.3 middle and right¹). This surface is proposed to pull off the collapsed, non-native substrate protein to give the substrate a second chance to fold into the proper conformation.

It is known from small angle scattering[56, 57] and electron microscopy[51] data that the two GroEL heptameric rings are separated by the C- and N-terminal ends of the subunits, forming a plug between the two cavities. Therefore, the unfolding of the denatured protein cannot occur by threading the amino acid chain through the orifice between the two GroEL rings, as mentioned after the discovery of the GroEL. However, the re-folding of the substrate protein can occur in the GroEL barrel, as well as after dissociation from the GroEL. The separated cavities of the GroEL cover a volume of about $85\,000\text{\AA}^3$ [52]. Considering a specific mass density of $\rho = 0.82\text{Da}/\text{\AA}^3$ for folded proteins, an upper limit of about 70kDa can be derived for proteins completely covered in the cavity. For the re-folding of larger proteins a different process, including the co-chaperonin GroES, has to be assumed.

The co-chaperonin GroES consists also of seven identical subunits of 10kDa molecular weight. The dome-shaped GroES can bind in the presence of ADP to one end of the GroEL cylinder, forming the asymmetric GroEL-GroES complex[51, 58]. The structure of the GroES from crystallography [58] is shown in figure 2.4.

The GroES subunit can be divided into two main domains: First the core region, which forms the dome, and second the loop region. This region is a highly flexible loop of about 16 amino acids and is the main binding site to the GroEL[59, 58, 60]. The binding of the GroES to GroEL occurs in the presence of nucleotides. A stable GroEL-GroES complex is formed in the presence of ADP and the GroES binds at the same GroEL ring as the ADP (=cis ring). This asymmetric GroEL-GroES complex (fig. 2.5) shows a high affinity for unfolded substrate protein and plays an important role in the chaperonin mediated re-folding process. A second GroES binding occurs only as a intermediate in

¹ The hydrophobicity is color decoded: blue=low hydrophobic → green=high hydrophobic

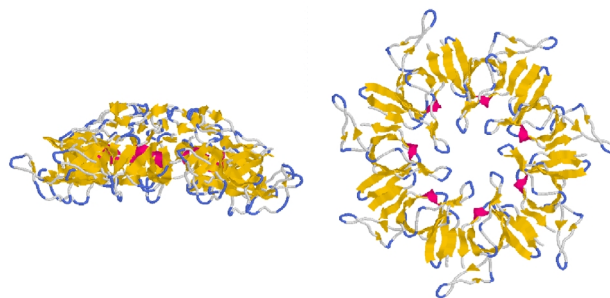


Fig. 2.4: Side and top view of the co-chaperonin GroES. The dome of the protein has a diameter of about 80Å and a height of 30Å

the presence of a high amount of ATP, and this symmetric complex is proposed to be a transient state in the chaperonin reaction cycle[61].

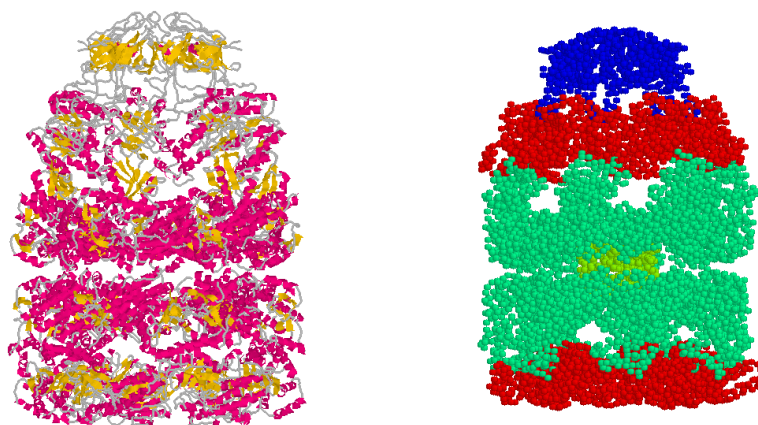


Fig. 2.5: The asymmetric GroEL-GroES complexes. Left: Crystal structure; right: Model derived from small angle neutron scattering

The asymmetric complex was co-crystallized with ADP[60]. The binding of GroES initiates large conformational changes of the GroEL *cis*-ring. First the apical domains are pivoted 60° upwards and rotated 90°. A second movement is the flapping of the apical domain inwards by pivoting the intermediate domain at the hinge between the intermediate and equatorial domain. The folding cavity enlarges by the binding of the GroES to 175 000Å³, more than double that of the GroEL cavity in the unbound state[60]. Finally, the shape of the GroEL 14-mer is slightly changed by an en-bloc inward tilting of the *cis*-GroEL ring, whereas the *trans*-GroEL ring is consequently tilted outward. The binding of GroES to only one side of the GroEL breaks the symmetry of the initially equal GroEL rings. This break in symmetry is connected with the cooperative binding of the nucleotides. The nucleotide binding and hydrolysis at the binding pockets of the GroEL show an interplay between positive cooperativity for one ring and negative cooperativity for the second ring[62, 63, 42].

Only one species of nucleotides, e.g. ADP can occupy the seven subunits of one ring, while the seven nucleotide binding sides of the second ring remain free or occupied by the other nucleotide (e.g. ATP). In the presence of K⁺ and Mg⁺⁺-ions the bound ATP can be hydrolyzed to ADP. Hence hydrolysis of the ATP can occur only in one ring, while the other is inhibited[41]. The energy gained by this

common biological process is used for the re-folding of substrate protein, and the different nucleotide-bound states produce different structural arrangements of the GroEL and/or the GroEL-GroES complex. Therefore, the nucleotides are not only used as an energy source, they also trigger conformational changes of the chaperonins during their working cycle. This feature of the chaperonins is reflected in the kinetic constants for the nucleotide binding, which show rather different values.

Nucleotide	apparent binding constant K_{App}	
	+ GroES	- GroES
ADP	70nM	2.5mM
ATP	10 μ M	6 μ M
AMP-PNP	290 μ M	110 μ M

Tab. 2.1: Apparent binding constants of nucleotides to the chaperonin GroEL. Adapted from[64]

The GroEL without GroES shows a factor 1000 higher affinity to ATP than for the ADP binding. The ADP is easily removed from the binding pockets by the ATP, reflecting that the ATP is the driving source in the chaperonin mediated protein folding. The whole interactivity between the nucleotides, GroES and GroEL is a highly coordinated process and can be expressed in a "two-stroke"-model for the chaperonin cycle[65]. This model takes the positive cooperativity in one GroEL heptameric ring, as well as the negative cooperativity between the two rings, into account.

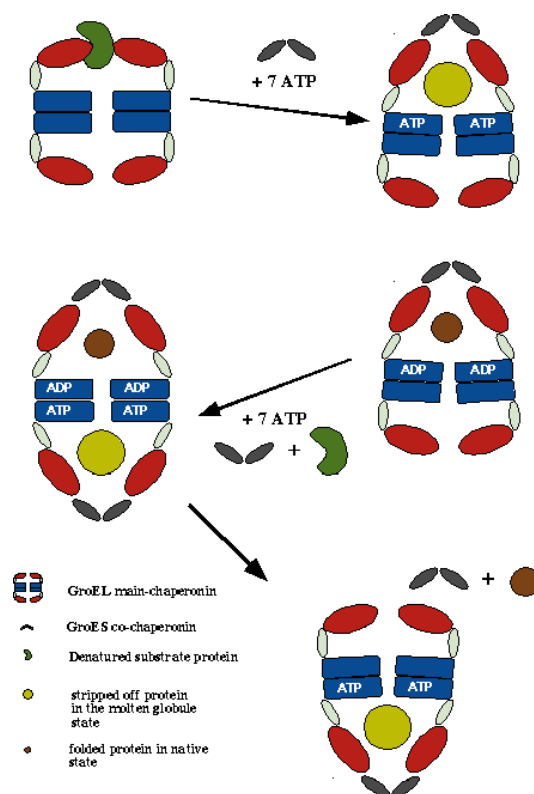


Fig. 2.6: The GroEL-GroES "two-stroke" re-folding cycle

Model of the GroEL-GroES-Substrate "two-stroke engine":

The initial step is the binding of the denatured substrate protein to the GroEL at the apical domains.

In the presence of GroES and ATP, the substrate slips into the enlarged cavity under the GroES. The hydrophobic walls strips off the substrate protein, processing the protein into a molten globule state. Under ATP hydrolysis the substrate can fold into its native conformation, and the second *trans* GroEL ring can now bind ATP. The ATP binding leads to substrate and GroES binding, forming the **symmetric** GroEL-(GroES)₂ complex. From this intermediate the *cis* bound GroES and the ADP dissociate and the re-folded substrate is released. If the substrate protein is not re-folded after one circle, it can be rebound and the re-folding cycle starts again[66].

3. TIME RESOLVED SMALL ANGLE SCATTERING OF PROTEINS

Synchrotron radiation, insertion devices, SAXS beamlines at ESRF and ELETTRA, Stopped flow device for fast mixing, Detection of X-rays: CCD vs. Gas filled detectors

3.1 Small Angle X-ray Scattering

The amplitude A_k of scattered X-ray photons and neutrons can be classically described as a plain wave scattered by an ensemble of atoms:

$$A_k = b_k e^{-i \frac{2\pi}{\lambda} (\vec{s}_0 - \vec{s}) \cdot \vec{r}_k} \quad (3.1)$$

b_k scattering density of the scatterer

λ wavelength

\vec{r}_k inner distance vector

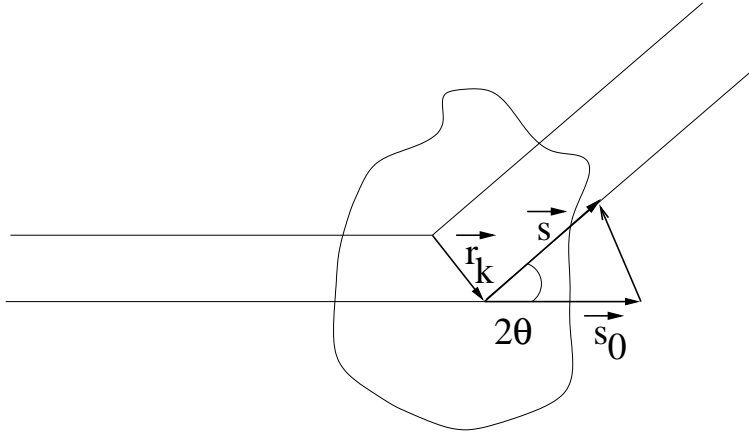


Fig. 3.1: Scheme of the scattering of X-rays and neutrons

The superposition of the A_k leads to

$$A(q) = \sum_k A_k = \sum_k b_k e^{-i \vec{q}_k \cdot \vec{r}_k} \quad (3.2)$$

while q_k defines the scattering vector with $|q| = \frac{4\pi}{\lambda} \sin\theta$ (using $\sin(2\theta) = 2\sin\theta$ which holds for small angle θ).

While the molecules are in an ideal solution randomly oriented the vectors \vec{q}_k and \vec{r}_k equation 3.2 have to be averaged over the 3-dim (see appendix), and the experimental measured scattering intensity $I(\vec{q})$

results in the **Debye formula**[67]:

$$I(q) = 4\pi \int_0^{D_{max}} p(r) \frac{\sin(qr)}{qr} dr \quad (3.3)$$

The scattering function depends only on the absolute value of q . Thus, the experimental result of a small angle scattering experiment is a centrosymmetric radial scattering pattern as shown in fig. 3.2. From this scattering pattern the 1-dim scattering intensity $I(q)$ is obtained by radial averaging.

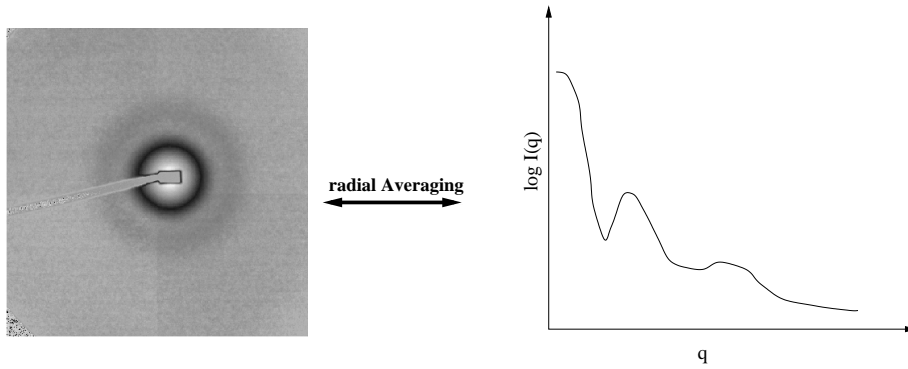


Fig. 3.2: Scattering pattern of a small angle X-ray experiment

The $p(r)$ function in the formula 3.3 can be extracted via Fourier transformation of the $I(q)$ function with the result:

$$p(r) = \frac{1}{4\pi} \int_0^{q_{max}} I(q) qr \sin(qr) dq \quad (3.4)$$

The $p(r)$ function, the pair distance distribution function, represents the distribution of distances within the molecule and provides direct structural information about the particle. The intensity distribution, as well as the $p(r)$ function, can be directly calculated from the atomic coordinates of the molecule. The reverse calculation of the atomic coordinates out of small angle scattering data is due to the loss of information not possible. Fig 3.3 shows the so called "inverse scattering problem":

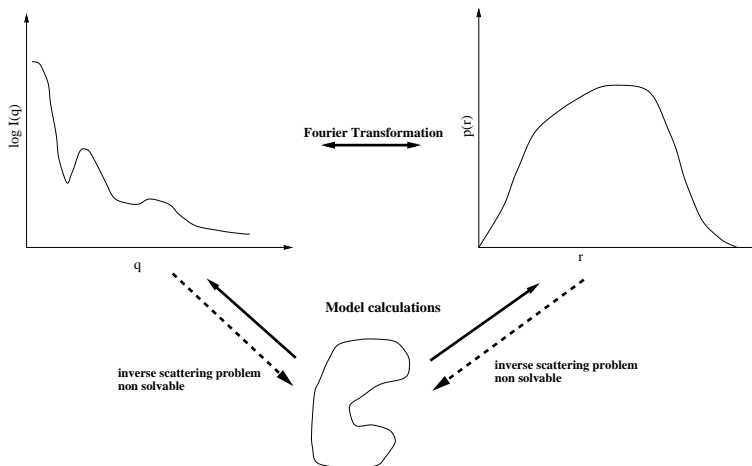


Fig. 3.3: The inverse scattering problem

Very sensitive information about the changes in the shape of a molecule is provided by the **Guinier radius** equivalent with the radius of gyration R_g . This parameter represents the second moment of the distance distribution function and can be easily calculated:

$$R_g^2 = \frac{\int_0^{r_{max}} p(r)r^2 dr}{\int_0^{r_{max}} p(r) dr} \quad (3.5)$$

The radius of gyration can also be calculated directly from the scattering function $I(q)$. By fractionizing the $\sin(qr)$ of the $I(q)$ function Guinier derived a theoretical description of the scattering function and a simple way to estimate the R_g -value (see appendix):

$$I(q) = I_0 e^{-\frac{(qR_g)^2}{3}} \quad (3.6)$$

In a special plot, $\ln I(q)$ vs. q^2 the inner part of the scattering function becomes a linear behavior and the Guinier radius can be estimated by simple line fit. In fig. 3.4 a so called Guinier plot shows the fitting procedure:

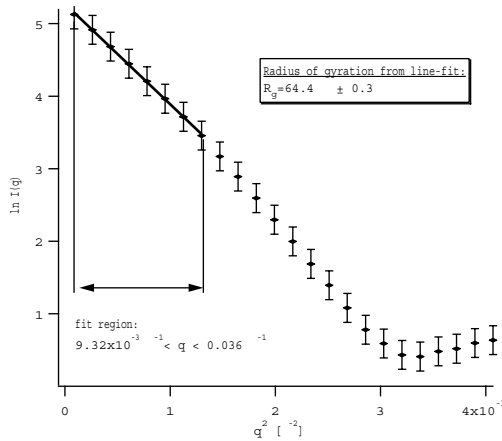


Fig. 3.4: Guinier plot

3.2 Beamlines for Small Angle Scattering

The small angle scattering techniques for X-ray were developed almost 50 years ago. At this time the X-rays were produced by X-ray tubes (Röntgenröhre). The development of electron accelerators and storage rings (synchrotrons) for particle and high energy physics led to so-called first generation X-ray sources. At these synchrotrons, relativistic electrons are bent by magnets onto a circle. If a relativistic electron ($v \approx c$) is deflected by a magnetic field electromagnetic radiation is emitted.

This radiation was first observed in 1947 at the e^- -synchrotron from General Electric Co. in Schenectady/USA. The main advantages of accelerator produced radiation are:

1. continuous spectra
2. high flux of photons
3. small beam size (relativistic electrons)

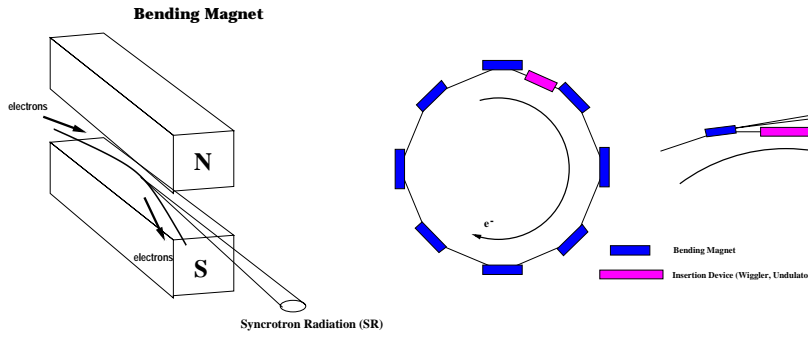


Fig. 3.5: Bending Magnet: The electrons are deflected by the magnetic dipole and can be bended onto a circular motion. In the case of relativistic electrons the synchrotron radiation (SR) is radiated tangentially from the electron beam and is strongly forward directed.

The first synchrotrons were dedicated for particle and high energy physics, and synchrotron radiation (SR) was a "waste-product" and could be only used "parasitically" for scattering experiments. The synchrotrons of the second generation sources were specially dedicated for SR users, and beamlines for synchrotron radiation were adapted to the bending magnets (see figures 3.5 and 3.6). A large improvement of the flux and the brilliance ($\frac{\text{photons}}{\text{mm}^2 \text{mrad}^2 0.1\% BW}$) of synchrotron radiation was the development of so-called insertion devices such as wigglers and undulators. These special devices were built into the straight sections of the storage ring between the bending magnets, and the synchrotrons were upgraded to the third generation sources. The Fig. 3.6 (left) shows an overview of the European Synchrotron Radiation Facility (ESRF) in Grenoble, a third generation X-ray source and the improvement of the flux for the different X-ray sources (right).

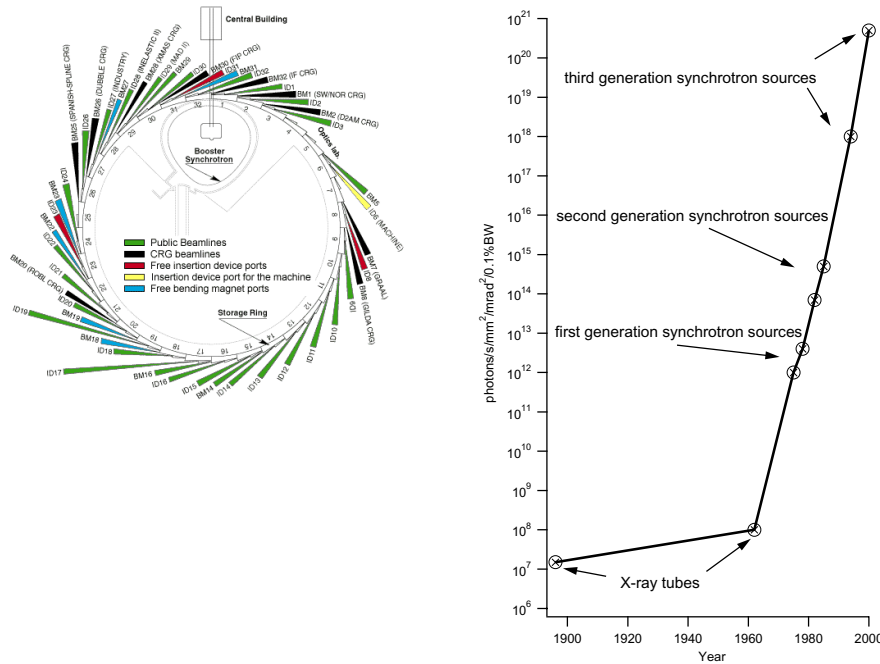
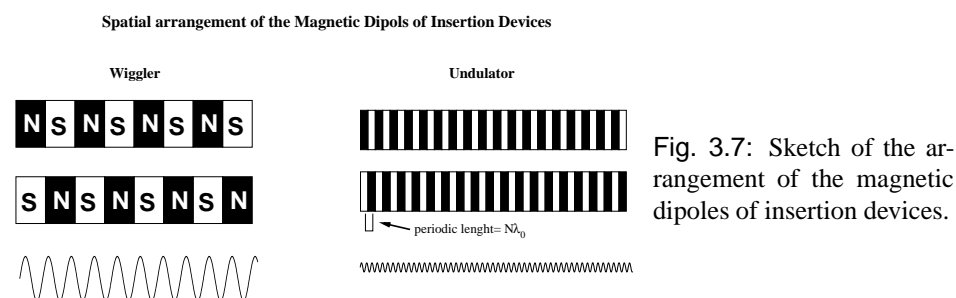


Fig. 3.6: Overview of the ESRF and the improvement of the photon flux from X-ray tubes to third generation synchrotrons. The improvement in the brilliance between the X-ray tubes and the third generation sources is in the order of 14 magnitudes!

Insertion devices such as wigglers and undulators are build of special sequences of the magnetic dipoles and produce synchrotron radiation with special properties. Figure 3.7 shows the spatial arrangement of a wiggler and an undulator.

The bunch of relativistic electrons ($v_{elec} \approx c$) traveling through the synchrotron vacuum tube is deflected by every dipole. The different arrangement of the magnets (see fig. 3.7) leads to different properties of the produced synchrotron radiation. While the deflection of the electrons in the magnetic



field of the wiggler produces a broad spectra of radiation, the spectra of the undulator shows a spiky structure. The reason is constructive interference of the photons at the harmonic wavelength λ_0 of the undulator. Fig. 3.8 shows two typical spectra of an undulator and a wiggler. Typical wigglers and undulators are the U46 at the ESRF and the wiggler at the ELETTRA SAXS beamline.

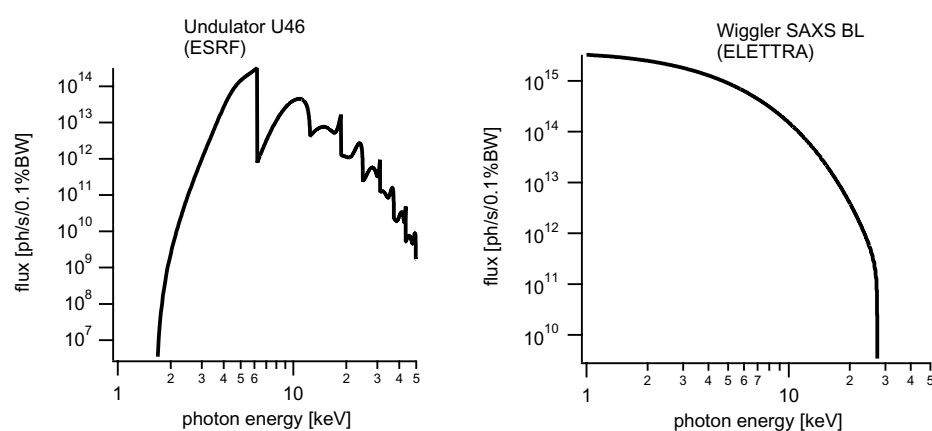


Fig. 3.8: Synchrotron radiation spectra of the ESRF U46 and the wiggler at the SAXS beamline at ELETTRA.

The different parameters for undulator and wiggler beamlines are listed in tab.3.1:

Parameter	Bending Magnet	Undulator U46 (ESRF)	SAXS BL (ELETTRA)
Magnetic Field	0.8T	$\approx 2T$	1.607T
Periodic length	—	46mm	70mm
Source Size (HxV)	$0.4 \times 0.3 \text{ mm}^2$	$1.03 \times 0.21 \text{ mm}^2$	$3.9 \times 0.26 \text{ mm}^2$
Divergence	$0.115 \times 0.005 \text{ mrad}^2$	$0.043 \times 0.027 \text{ mrad}^2$	$0.08 \times 0.05 \text{ mrad}^2$
Flux at sample	$10^{10} - 10^{11} \text{ ph/s}$	$8 \times 10^{12} \text{ ph/s}$	$5 \times 10^{12} \text{ ph/s}$
Beamsize at sample	$1 \times 1 \text{ mm}^2$	$0.6 \times 0.2 \text{ mm}^2$	$5.4 \times 1.8 \text{ mm}^2$
	(focused at sample)	(focused at sample)	(focus on the detector)

Tab. 3.1: Parameters of Insertion Devices

For the monochromatisation of the polychromatic SR, Bragg double monochromators are used. Relying on the Bragg effect at a silicon single crystal, a precise photon energy can be cut out of the SR spectra.

The spectral resolution of a X-ray monochromator crystal is determined by its degree of crystalline perfection. Deformation of the crystal by the head load induced by the radiation has to be taken into

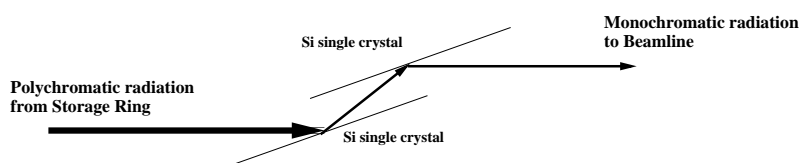


Fig. 3.9: Silicon single crystal double monochromator

account and the crystal has to be cooled by liquid nitrogen. Using the typically single crystals at the ESRF an energy resolution $\frac{\Delta E}{E} = 2.0 \times 10^{-4}$ (at 12keV) can be obtained. As described in the table above, the strongly forward directed synchrotron radiation shows, depending on the insertion device used, a more or less high degree of divergence. Without focusing of the radiation the beam size will be increasing within the distance from the source point at the insertion device or bending magnet. For the focusing special X-ray mirrors are used. These specially shaped mirrors consist of a Rh-coated (ESRF SAXS Beamline) double-focusing toroidal surface. It is optimized for obtaining a small beam size at the sample stage, typically between 50m to 60m behind the source point of the radiation.

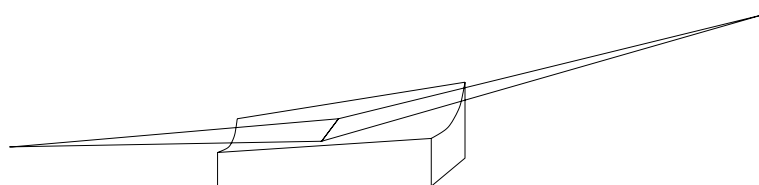


Fig. 3.10: Scheme of a toroidal mirror

A complete sketch of a typical SAXS beamline is shown in fig 3.11. The SAXS station of ELETTRA consists of a monochromator and a toroidal mirror, as described above. The second monochromator crystal is mounted above in order to guide the monochromatic beam to the optic hutches and the experimental station.

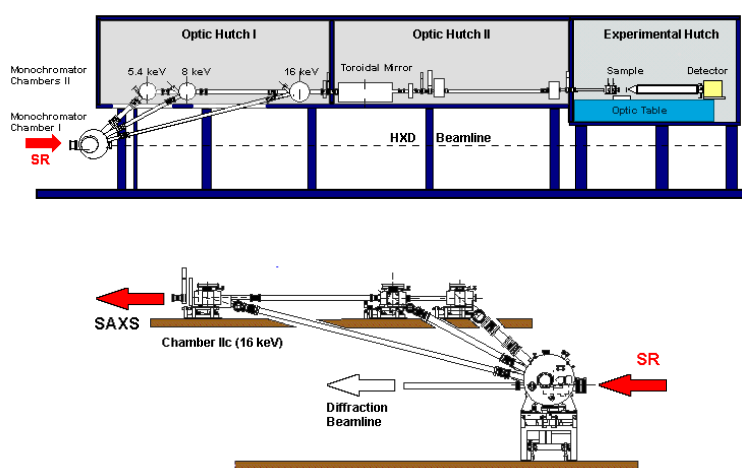


Fig. 3.11: Scheme of the Elettra SAXS beamline

3.3 The Stopped Flow Device

The main advantage of small angle scattering is that this technique allows one to perform very easy time-resolved experiments under native conditions. If the reaction can be triggered by mixing reactants together a simple mixing machine can be used. The rapid mixing of the reactants is achieved by a stopped-flow device driven by a stepping motor. This machine was developed in order to obtain fast, precise and reproducible mixing conditions. It consists of a controller and up to three stepping motor devices. The controlling and timing is done by a PC using LabView as a programming platform. This device was used at several synchrotron and neutron facilities for small angle scattering. The mixing volume are about $200\mu\text{l}$ and the dead-time for the mixing should not exceed 20ms in order to follow reactions in the sub-second time range. For this purpose, the stepping motor device has to fulfill the following conditions:

1. short response time and fast acceleration (see Fig. 3.12)
2. high precision in the number of steps
3. accurate and reproducible stepping length
4. exact timing
5. easy and flexible to mount at the beamline

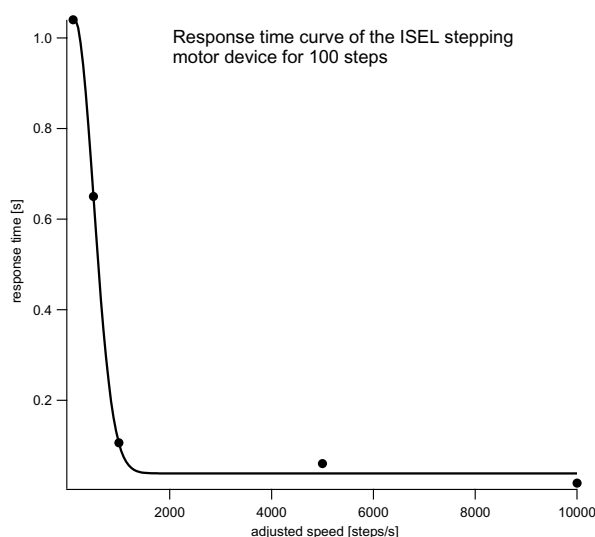


Fig. 3.12: Acceleration response curve of the stepping motor device.

The problem in the case of stepping motors is the acceleration. The motors need a certain number of steps to accelerate to the adjusted speed. On the other hand, the number of steps is limited by the mixing volume, which should be as small as possible. As the response curve in fig. 3.12 shows, the high speeds cannot be achieved within the small volumes. Since the response time levels off at a speed of 1200 steps/s, no faster response times (=mixing time) as $\approx 20\text{ms}$ can be obtained. The volume can be controlled by the number of steps and/or using different syringes. By decreasing the size of the syringe the number of steps can be increased, but speed is lost and the syringes have to be refilled more often. For example, 100 steps, using 1ml syringes leads to a mixing volume of about $40\mu\text{l}$ and 100 steps, using the 2.5ml syringe, gives $110\mu\text{l}$. A serious problem is the tight mounting of the syringes in the stopped-flow apparatus. In order to avoid problems with protein sticking to the surface which is in

contact with the solution, and damaging due to aggressive components, Teflon was chosen as material. However, Teflon is a very soft material. The thread of the syringes have therefore to be conducted by a harder material. This was achieved by a metal plate which was fitted into the Teflon block. In this plate the threads for the syringes were tapped, but the outlet orifice of the syringe was sealed by pressing it to the Teflon. The syringe is held by a cap-nut and can be fixed with a clip. In figure 3.13 schemes of the stopped-flow apparatus and the intake are shown. Further technical details can be found in the appendix.

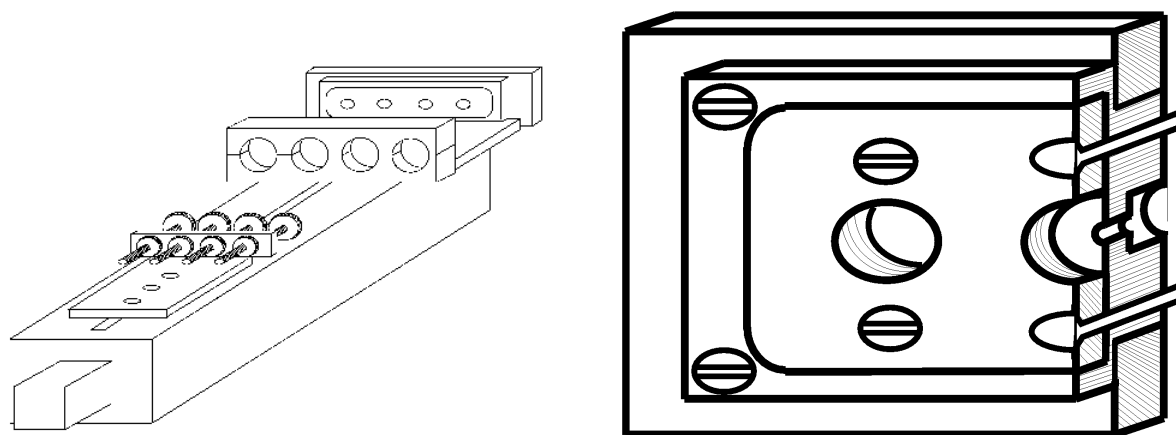


Fig. 3.13: Stopped-flow apparatus mounted on a ISEL linear drive. The syringes are mounted using a special intake (see sectional drawing right)

In the next figure the stopped-flow apparatus mounted on the ESRF small angle scattering beamline is shown.

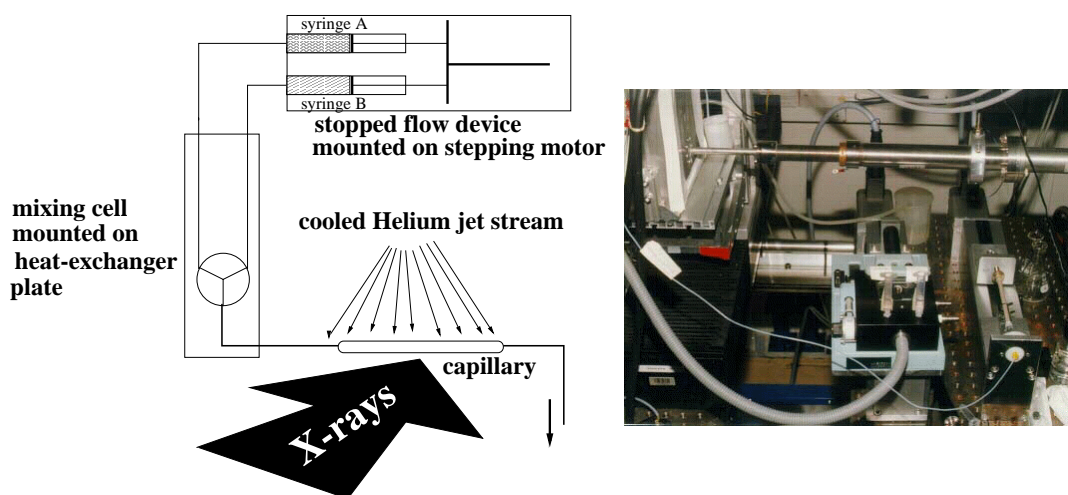


Fig. 3.14: Scheme of the stopped-flow device, and in use at the ESRF SAXS beamline

3.4 The Radiation Damage Problem

A serious problem of X-ray scattering at high flux facilities is the radiation damage of the proteins by the X-ray photons. The absorption of photons with an energy of 12keV ($\sim 1\text{\AA}$) in water is about 50% and the energy is mainly converted into heat. The heat-load at the sample on the ESRF SAXS beamline is in the order of 2W in a very small exposed volume (beam-size: $0.6\times 0.2\text{mm}^2$). This beam-heating leads to a thermally induced denaturation of the proteins, while a second process, the production of radicals by the ionizing radiation attacks the proteins directly. To avoid this effects two precautions have to be taken:

1. Avoidance of beam-heating by cooling of the sample
2. Use of glycerol as a radical quencher
3. Reduction of the total exposure time of the sample

Whereas the use of a radical quencher such as glycerol (10% V/V) does not cause problems, the cooling device for the sample is a technical challenge. However, for the investigation of a reaction the sample should be kept at a fixed temperature over the whole experiment. To achieve this a temperature controlled sample box was developed by Dr. Thomas Nawroth (Univ. Mainz). This box covers the fragile quartz capillary, pre-tempers the reactants and provides a jet-stream of tempered He-gas onto the capillary. Nevertheless, this set-up is not sufficient to follow a reaction over a period of more than 5s (see \blacklozenge Fig. 3.15 right). For a longer investigation a third syringe was introduced to the stopped-flow set-up. This buffer-filled syringe (syringe C in fig. 3.15 left) was connected to the flow lines directly behind the mixer. While the syringes A+B mix the reactants together in the reaction loop and the capillary, syringe C pushes the already mixed solution slowly through the X-ray beam. The speed of this third syringe was correlated between the total duration of the experiment and the mixed volume, so that each volume part of the sample was not irradiated longer than $\approx 1\text{s}$. Using this set-up we were able to investigate the reaction over 40s, whereas the total time of exposure (lifetime + dark-time/readout; see chapter "Detectors") was 8s. The radius of gyration of the proteins were stable throughout the whole experiment (solid line in fig. 3.15 right).

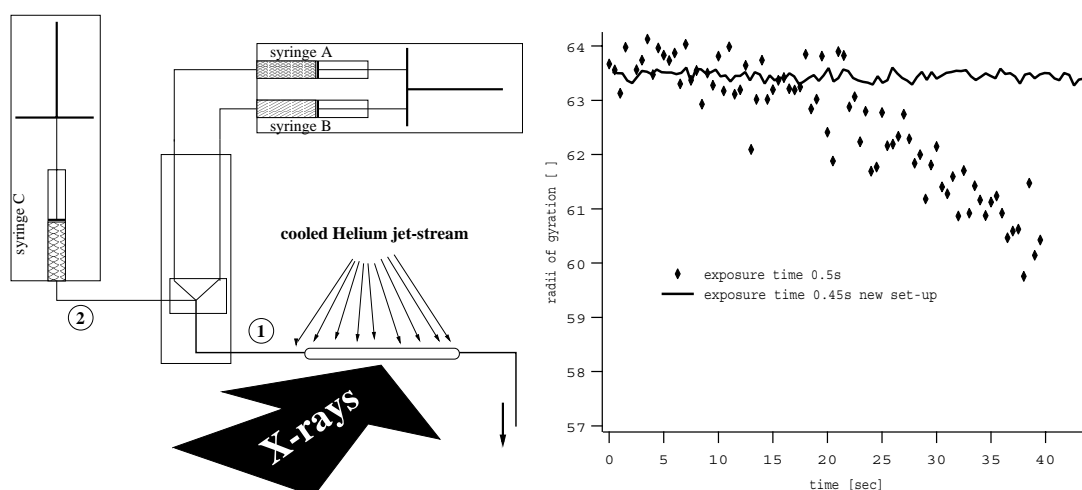


Fig. 3.15: Advanced set-up to prevent radiation damage

3.5 Model calculations

Due to the random orientation of the molecules in the solution atomic coordinates can not be recalculated directly out of the small angle scattering data. However, performing model calculations based on coordinates from crystal structures, and comparing the results with the experimental derived data, conformational changes of the molecules during the reaction cycle can be described. The analytical calculation of small angle scattering data is solved for geometrical compounds such as rods, cylinders and spheres. Using the **Rayleigh formula**, the scattering intensity $I_K(q)$ can be calculated for a single sphere:

$$I_K(q) = \phi_K(q) \cdot \phi_K(q)^* = \left[\frac{3(\sin(qr) - qr \cos(qr))}{(qr)^3} \right]^2 \quad (3.7)$$

Where r represents the radius of the sphere and q the norm of scattering vector \vec{q} .

Small angle scattering results in no atomic resolution. Therefore, proteins can be approximated by models consisting of spheres located at every C_α -atom of the protein backbone. The radius of the sphere can be estimated from crystallographic data for amino acid residues to $r=3.3\text{\AA}$ [68].

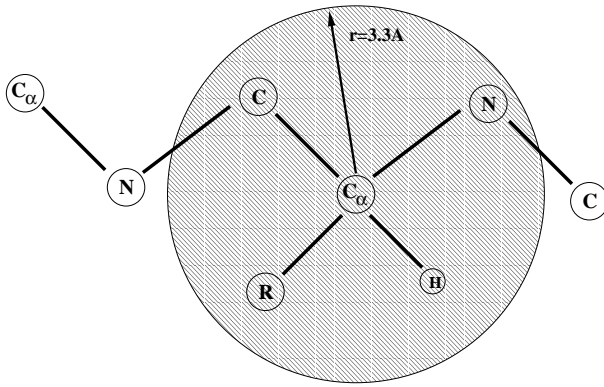


Fig. 3.16: Modeling of the amino acid backbone of a protein

The scattering intensity of the complete protein is calculated by superposition of the spheres over the whole ensemble using the Debye formula.

$$I(q) = \sum_{i=1}^N g_i^2 \phi_i^2(q) + 2 \sum_{i \neq k} g_i g_k \phi_i(q) \phi_k(q) \frac{\sin(r_{ik}q)}{r_{ik}q} \quad (3.8)$$

Where the g_i are the scattering density of the i -sphere with a scattering amplitude $\phi_i(q)$ and the r_{ik} represents the distance between the i -th and the k -th sphere.

These theoretical calculations were carried out using the program package MULIBODY from Otto Glatter[69].

The structural and the functional implication can be derived from small angle scattering data by calculating the initial structure of the protein using the crystal coordinates and by changing the coordinates, and comparing the resulting structure with the experimental data step by step. This strategy is shown in the next figure.

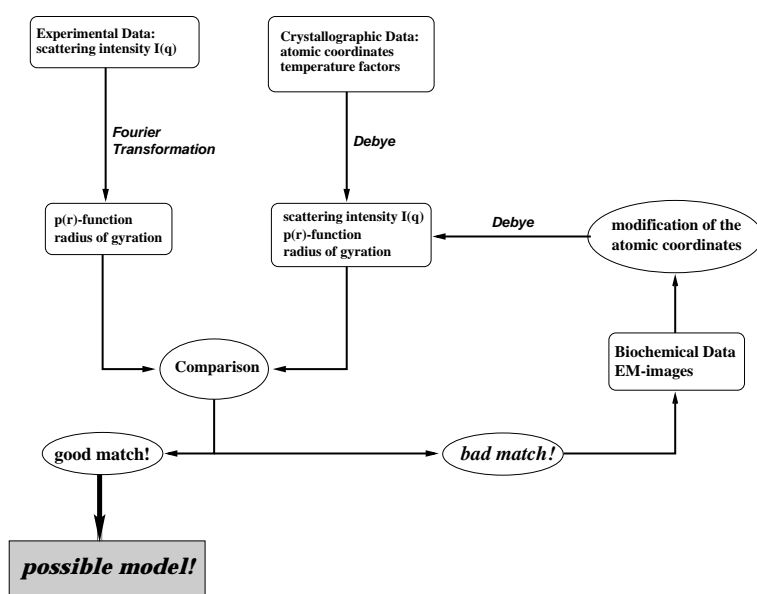


Fig. 3.17: Modeling strategy for small angle scattering data

3.6 Detectors for Time-Resolved Small Angle Scattering

Gas-filled delay-line detector, Radiolysis of the counting gas; The CCD camera "FRELO"; Image plates - an alternative?

As shown in the introduction, the flux of photons produced by synchrotrons has increased over the last ten years dramatically. While properties of the synchrotron radiation such as polarisation and continuous spectra are important for other methods, the detection of the full photon flux is most important for time-resolved small angle X-ray scattering. Unfortunately the improvement of detectors does not go hand in hand with the improvement of flux. Therefore, several detectors have to be tested to find out the proper conditions to use.

3.6.1 Gas-filled Detectors

At the beginning standard gas-filled wire detectors were used at the SAXS beamlines of ESRF and ELETTRA. While the detector at ESRF's ID2 was a two dimensional (2-d) area detector, at ELETTRA a 1-d single wire detector was used. The gas-filled wire detectors work on the principle of a proportional counter. An incident photon ionizes a gas molecule, which emits an electron. This electron ionizes other gas molecules in the electric field between the anode-wire and the cathode-wire and produces an avalanche of ionized particles. This avalanche creates current pulses at the charged wires. The pulses can be counted and directly converted into the position on the wire. So-called delay line detectors calculate the x and y positions from the delay time between the strong negative anode pulse ($=t_0$) and the position dependent runtime ($=t_{pos}$) of the positive cathode pulse (Fig. 3.18). As the counting gas of this **MultiWire Proportional Counter (MWPC)** a mixture of 90% xenon and 10% methane or carbon dioxide is used. Xenon has a good photoelectric absorption cross section for X-ray photons, and the polyatomic CH_4 or the CO_2 atoms are ionized by inelastic collisions to produce the second ionisation avalanche.

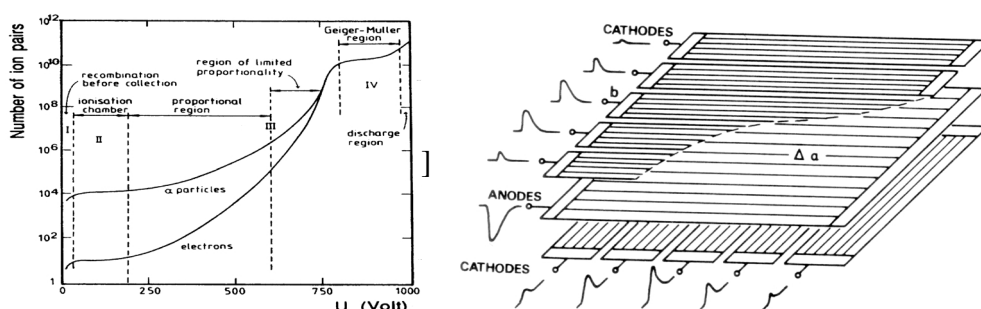


Fig. 3.18: The multi-wire proportional counter. Characteristic line of the Geiger-Müller counter and spatial layout of the wires.

However, a gas-filled detector can only stand 10^9 ph/s. The main reason is the local saturation of the absorbing gas by the high flux of incident photons; this is about $10^4 \text{ ph s}^{-1} \text{ mm}^{-1}$ (depending on the mixture of the absorbing gas), and is determined by space charged build-up in the local region of the counting gas. Further reasons are the indistinguishability of two coincidently detected photons. If the delay time counting is started and a second photon hits the detector before the counting is finished, it would lead to a superposition of the two photons. These coinciding photons have to be rejected. Another serious problem is the radiolysis of the counting gas, specially of the polyatomic component.

These gases are dissoziated under conditions of high radiation flux and built-up polymerized hydrogencarbons or carbon films on the anode wires. At 12keV photon energy ($=1\text{\AA}$ wavelength) the ESRF ID2 beamline produces about 1×10^{13} ph/s. The transmission of the sample at this energy, is about 60%. Taking the scattering cross section of the protein in the water environment of 10% into account, the detector has to stand 6×10^{11} ph/s, on the full 360° area angle. This huge amount of photons produces a non-linear and non-reproducible behavior of the detector, based on the problems of gas-detectors mentioned above (see figure 3.18 right).

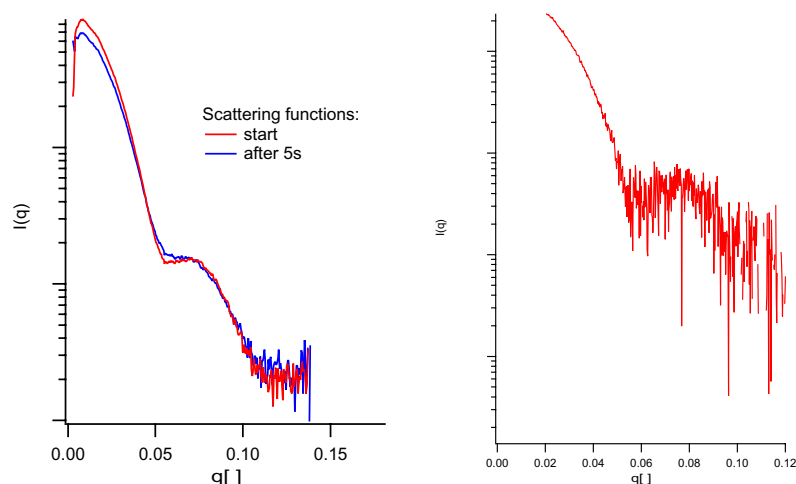


Fig. 3.19: Scattering functions recorded with proportional counters. Data obtained with a 360° 2-d area detector (left) and a 1-d wire detector (right).

Decreasing the flux in order to overcome these problems results in a reduction of the statistics of the scattering data. The 1-dim detector of the ELETTRA showed no deadtime and no radiolysis effects but the decreasing of the amount of detected photons from 1×10^{13} ph/s incident flux to 2×10^8 ph/s detected, produced scattering functions with very bad statistics (Fig. 3.19 right).

Nevertheless, the big advantage of the delay line detectors is the very fast readout in the ps range.

3.6.2 X-ray CCD detector

CCD (Charged Coupled Device) detectors which are photon accumulators are different to gas-filled detectors, which act as single photon counters. The photons hitting the CCD generate a set of free electrons and holes in the semi-conductive CCD pixel-array. The produced charge is proportional to the energy of the incident photon. Each CCD array consists of a serial and a parallel register. While the charge is stored in the pixels of the parallel register ($=2$ -d array of the CCD-chip), the serial register is used to unload these charges during the read-out of the array. For this, the charged parallel array is iteratively shifted to the serial register during the read-out. An analog-digital converter transforms the charged serial register into a digital signal. A high end CCD array such as the FRELON camera, consists of 1024×1024 pixel each having a size of $19\mu\text{m}$.

A problem for time-resolved small angle scattering is the read-out structure of the CCD detector. During the read-out of the CCD registers no photon has to hit the semi-conductive pixel-array. The read-out and the erasing of the CCD array takes 150ms (see fig. 3.20). This limits the capability of CCD detectors for time resolved analysis. Nevertheless, CCD arrays are the only "online" detectors which can stand the full flux of a third generation synchrotron sources at the moment. Small angle

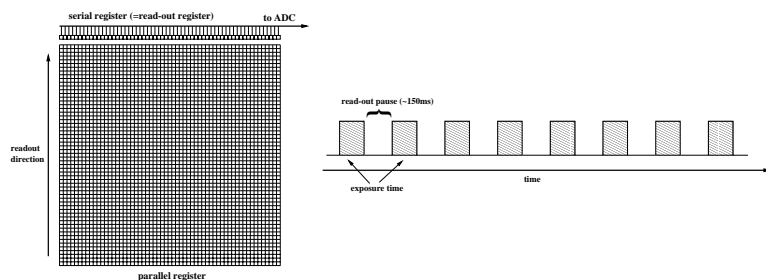


Fig. 3.20: Scheme of the serial and parallel registers of a CCD-array. The readout of this array takes 150ms (FRELON; ESRF), where no new image can be taken.

scattering functions can be recorded in the 100ms range with very good statistics using, the FRELON-CCD device available at the ID2 beamline at the ESRF. A typical SAXS pattern, and the resulting scattering function, are shown in figure 3.12.

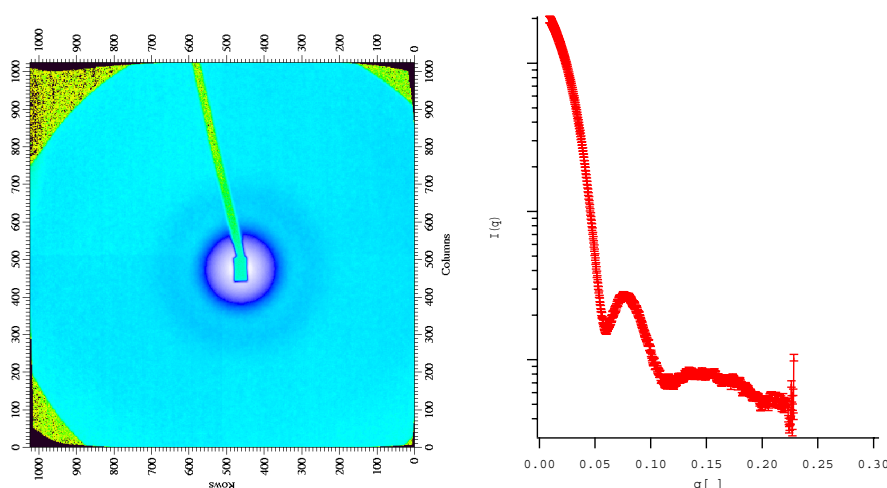
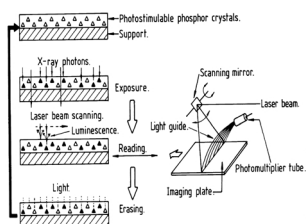


Fig. 3.21: Scattering pattern and evaluated scattering intensity function obtained by the FRELON CCD camera at an exposure time of 150ms.

The FRELON-CCD device was developed at the ESRF and specially adapted for high flux applications. The active area of the FRELON CCD chip is about 20mm^2 . This area is too small for obtaining scattering patterns. To overcome this problem a phosphor ($\text{Ge}_2\text{O}_2\text{S}$) coated screen is used to cover a much larger area. The emitted visible light is further enhanced by a photon amplification system, and projected over a system of optical lenses on the CCD array. A disadvantage of this converting and enhancing procedure is the spatial distortion of the recorded pattern. The pattern thus, has to be distortion corrected applying a plate with defined holes for calibration.

3.6.3 Image plates

A third type of photon-accumulating detectors are image plates. On an image plate the X-ray image is stored into a X-ray sensitive layer of photostimulable phosphor crystals. For the read-out the phosphor layer is scanned by a laser which excites the X-ray stimulated crystals. The resulting luminescence can be recorded on a diode or photomultiplier system with high spatial precision.



Recent developments (MAR Research) allow an online readout of the image plate without breaking the vacuum of the detector tube, but reading of one image takes about 2min. Therefore, for conventional time-resolved scattering techniques using a stopped flow apparatus, image plates are not practical. A possible application for image plates is time-resolved scattering experiments using a continuous flow of the sample for the time resolution. This method would allow the exposure a single time point, for a certain time and the read-out afterwards (see Chapter Outlook).

4. DATA REDUCTION, TREATMENT AND ANALYSIS

4.1 Small Angle Scattering Data

Radial averaging of detector pattern, Background subtraction using the POROD-law, Analysis of the Guinier-region, Calculation of the $p(r)$ -function using a direct Fourier-transformation

As discribed in the last chapter, the result of a small angle scattering experiment is a centro-symmetric scattering pattern. The area detectors described in the detectors section are able to record 2-dim scattering intensities with high accuracy. From this 2-dim pattern a 1-dim scattering function can be obtained by radial integration whereby the intensities, which belong to the same scattering angle θ , are integrated. This procedure, shown in figure 4.1, reduces the data and also enhances the statistic for every single data point by averaging over the same radiant. Thus, a 2-dim area detector the wider range on higher r -values can compensate the less scattering intensities on the wide margins of the detector.

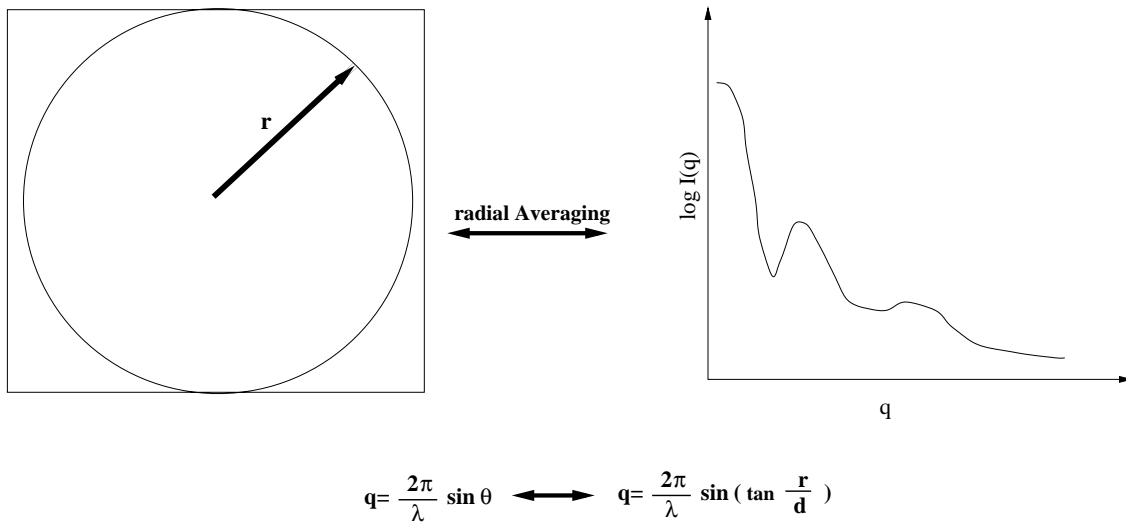


Fig. 4.1: Radial integration of the scattering pattern on a 2-dim area detector. (d =distance detector-sample)

In the next figure the recorded scattering pattern of the GroEL-GroES complex is shown. The pattern was taken at the ESRF ID02 beamline using the CCD-camera system FRELON, as described in the chapter detectors. The side maxima, produced by the central cavity of the GroEL hollow cylinder, produce concentric rings around the beam center. The inner part of the scattering pattern is protected by a beamstop, because of the highly forward directed, non scattered intensity which would saturate the detector within a short time. A serious problem of small angle scattering is the correct subtraction of the background scattering (capillary, windows, buffer e.g.). The scattering functions are normalized on the incident flux of X-ray photons, but nevertheless fluctuations of 5% have to be taken into account.

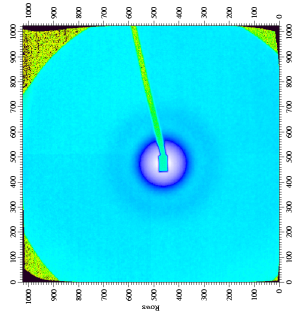


Fig. 4.2: Scattering pattern of GroEL, obtained at ESRF ID02 using the FRELON CCD camera.

The radial averaging of the data and the primary flux normalisation was done using the small angle scattering software available at the ESRF. This software was written and maintained by Peter Boesecke (ESRF ID01). Unfortunately, the data evaluation software includes **no** error estimation. This problem is discussed in the next chapter.

The scattering of the protein in the higher q -range is about 0.1% above the water scattering. Thus, subtraction of the scattering intensities needs further correction using **Porod's** law. In Porod's law, the scattering intensity is approximated at higher q -values by estimation of the interface particle-surrounding media. By using the Porod's approximation:

$$p = I(q)q^{-4} = pq^4 + k \text{ which holds for } q \gg D^{-1}$$

the "porod invariant" p can be calculated for the water-water interface in order to normalize the scattering function from this straight forward calculation. In fig. 4.3 the fitting procedure and the resulting p -values are shown.

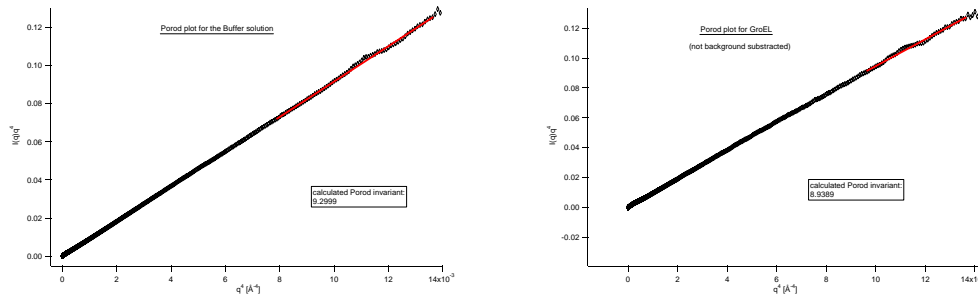


Fig. 4.3: In the porod plot ($q^4 I(q)$ vs. q^4) the region of higher q -ranges becomes linear. Using a linear fit, the porod invariant can be obtained directly.

The difference in the evaluated data is shown in figure 4.4. While some data points of the flux normalized data get lost due to wrong background subtraction (fig. 4.4 left), these data points remain using the porod invariant as a normalisation factor for the exact buffer subtraction (fig. 4.4 right). The lost data points at higher q -values are necessary for further analysis using the direct Fourier transformation.

From the buffer and background subtracted scattering intensities $I(q)$ the following data can be derived, as mentioned in the chapter "Small angle scattering":

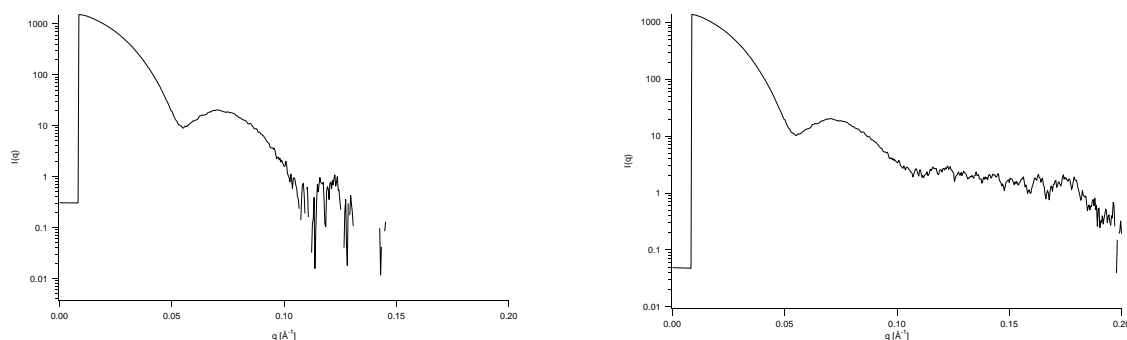


Fig. 4.4: In the porod plot ($q^4 I(q)$ vs. q^4) the region of higher q -ranges becomes linear. Using a linear fit, the porod invariant can be obtained directly.

1. The radius of gyration R_g (from the Guinier approximation)
2. The distance distribution function $p(r)$
3. The scattering intensity at $q=0$ (\sim molecular weight)

The radius of gyration

One of the easiest parameters derived from small angle scattering is the radius of gyration (R_g). This R_g -value can be calculated directly from the scattering function $I(q)$ by a straight forward linear fit procedure (fig. 4.5)[70]. The data analysis of the R_g was carried out using the macro language of IgorPRO (WaveMetrics, Lake Oswego, USA) running on a Macintosh. The analysis program runs automatically and calculates the values for every time point.

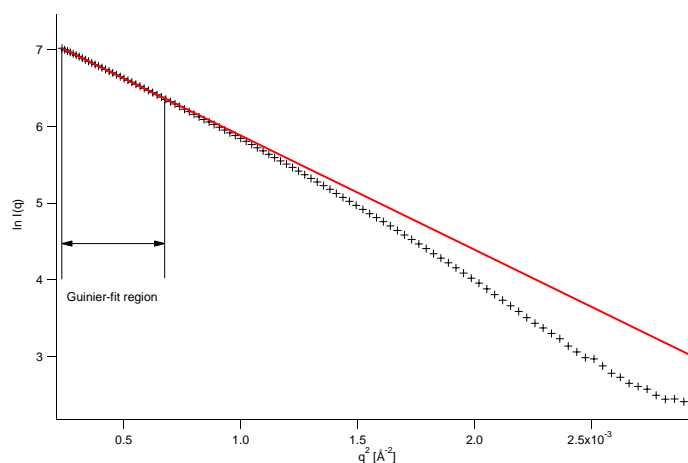


Fig. 4.5: Guinier fit of the GroEL-GroES complex. The R_g value was estimated directly by a linear fit procedure.

The final values for the radius of gyration were obtained by averaging the independent data-set for the single experiments. The figure 4.6 shows the results of four data sets, and the averaging for the GroEL reference (mixed with buffer).

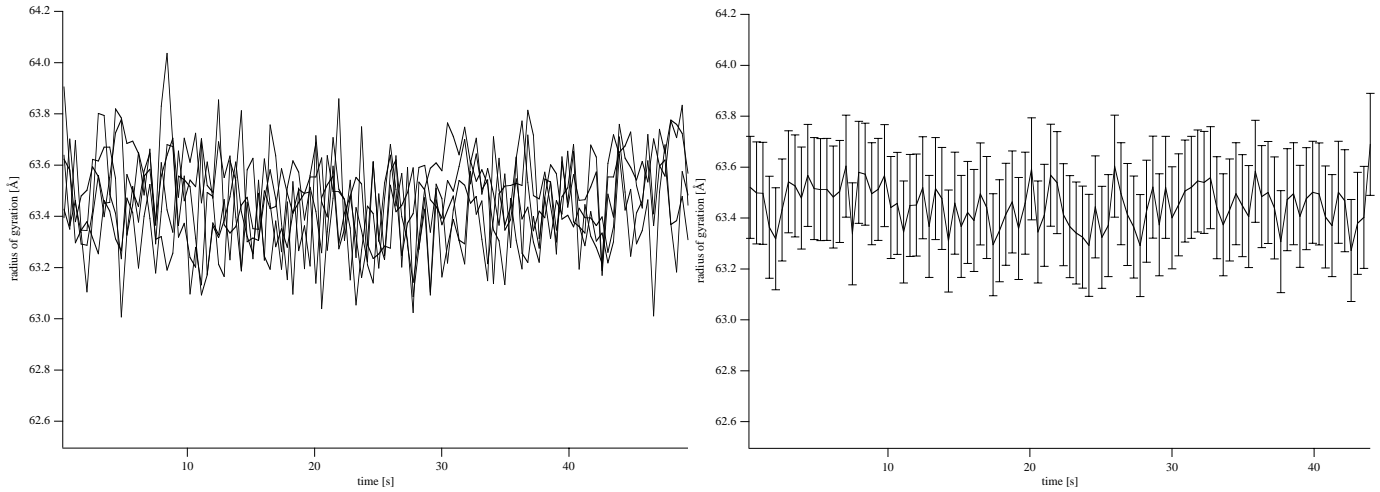


Fig. 4.6: Time progression of the Rg values for the GroEL mixed with buffer (reference). The picture left shows the analysis of five independent data sets. The right figure shows the averaged result with estimated errors.

The distance distribution function $p(r)$

The distance distribution function $p(r)$ is the most easy parameter to interpretate derived from small angle scattering. While the radius of gyration provides information about the shape of the particle, the $p(r)$ function provides information of the distribution on distances within the particle. Therefore, the $p(r)$ function contains direct structural information of the protein.

The $p(r)$ function can be calculated directly via Fourier transformation of the $I(q)$ function using the equation as follows:

$$p(r) = \frac{1}{4\pi} \int_0^\infty I(q) q r \sin(qr) dq$$

For the transformation of the experimentally derived scattering intensity function $I(q)$ via the formular above, a wide range of the $I(q)$ function has to be measured. While the outer part is easy to measure by changing the distance detector-sample, but with less intensity, the inner part of the scattering function is not measurable. The reason is the highly forward directed scattering due to the less scattering density of the protein in the water environment. To overcome this problem there are, in general, two strategies. First the indirect Fourier transformation developed by O. Glatter[69, 71], and the direct transformation method by interpolating the inner part of the scattering function using the radius of gyration as a parameter. The direct transformation procedure is used for the time resolved experiments presented here. The single steps for the direct transformation are described in figure 4.7:

The direct transformation procedure starts with background substracted scattering data from the Porod normalization described above. From this data the radius of gyration is calculated via the Guinier plot. The resulting Rg-value is used for the recalculation of the inner part of the $I(q)$ function by the Guinier approximation $I(q) = I_0 e^{-\frac{R_g^2}{3} q^2}$ which holds for small q -values (=inner part of the $I(q)$ function). This reconstructed part and the experimental data are put together to obtain the complete scattering function. The resulting function contains about 780 data points. In order to reduce this data for the numerical integration the experimental data were resplined by a cubic spline interpolation to 50 data points. This splined data was subjected to the numerical integration, whereby the upper integration limit was set to $r=D_{max}$, the maximal dimension of the protein.

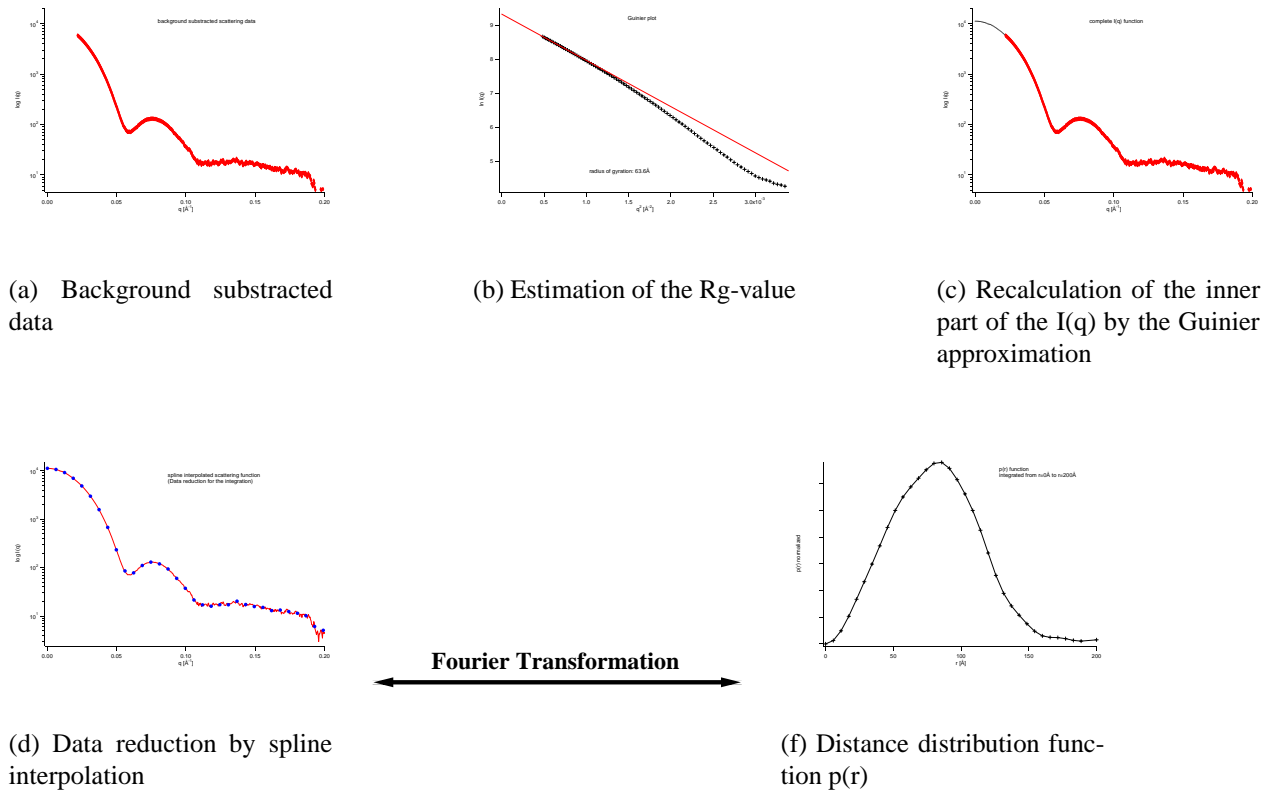


Fig. 4.7: The direct transformation method for time resolved small angle scattering data.

The $p(r)$ function calculated from this procedure was compared with a $p(r)$ function derived by the standard indirect fourier transformation from O. Glatter[71, 69]. The functions derived from the two different methods are shown in the fig. 4.8. Since the two $p(r)$ functions show no significant deviations,

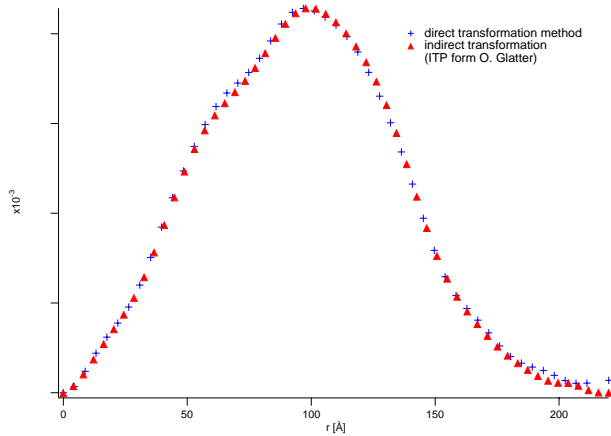


Fig. 4.8: Comparison of $p(r)$ functions derived from direct transformation (blue) and indirect transformation (red)

the direct transformation method is equivalent to the classical indirect transformation.

4.2 Error Estimation

A serious problem for the analysis methods described above is the error estimation. Unfortunately the radial averaging program for the small angle scattering data available at the ESRF contains no straight forward error calculation. Therefore it is essential for the further analysis to estimate the maximal errors. The scattering pattern recorded at a CCD detector contains 1024x1024 pixels on the CCD chip. While small angle scattering experiments using a "point-source" such as a third generation synchrotron, produce centrosymmetric scattering patterns, the area around the beamstop (=inner part of experimental scattering function) contains the highest amount of scattered photons. The statistics of the data at this area are thus rather high. The scattering intensities at the outer part is in the order of four magnitudes lower and produces data with bad statistics. On an area detector the radial averaging increases the statistics at this low counting area by simply adding a larger amount of pixels. The amount of radial averaged pixels is linear with the radius of the circle. For instance, the spatial resolution of the CCD-chip is $\approx 25\mu m$, therefore a circle at 10 pixels distance from the origin contains about ≈ 44 pixels. At the edge of the detector at 512 pixels distance from the origin this number of summed pixels goes up to 360. The variance of the scattering intensities per pixel increases from 3% in the inner part up to 10% in the outer area of the CCD-chip. Due to the increasing amount of counted pixels, the averaged errors for the mean value of the pixels in the outer part and the error for the averaged data for the inner part are nearly identical after the radial integration.

$$s_{inner} = \frac{0.03}{\sqrt{44}} \approx \frac{0.1}{\sqrt{360}} = s_{outer}$$

A scattering function with assigned errors is plotted in the following figure 4.7: The errors are printed for the upper and the lower limit as dotted lines.

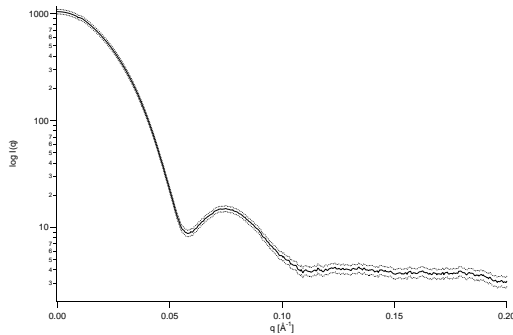


Fig. 4.9: Normalized scattering function $I(q)$ with assigned errors.

A second serious problem is the error propagation to the Fourier transformed $p(r)$ functions. While the error of the scattering intensity can be derived directly from the experimental data, the deviations of the $p(r)$ function is not a straight forward calculation. In order to obtain the variations of this important function three $p(r)$ functions were calculated:

1. $p(r)$ function from the $I(q)$ - errors (=lower limit)
2. $p(r)$ function from the $I(q)$ without errors

3. $p(r)$ function from the $I(q)$ + errors (=upper limit)

From these three Fourier transformed $p(r)$ functions (shown in fig. 4.8) the maximal deviation between the function was calculated and used as the maximal error.

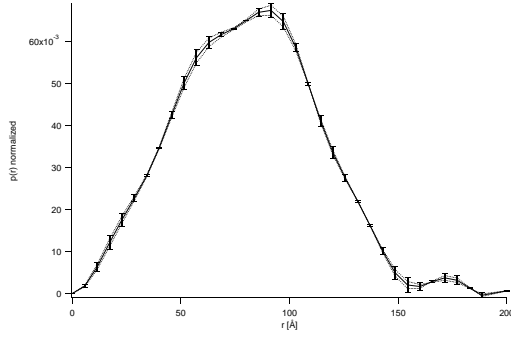


Fig. 4.10: Normalized $p(r)$ function $p(r)$ with assigned errors from the procedure mentioned above.

This procedure was carried out for only one of the scattering functions and the obtained maximal deviation was assigned as the standard error to all other data sets.

5. SAMPLE PREPARATION

The preparation of the chaperonin GroEL and GroES were carried out by Dipl. Chem. Elena Manakova at the Max-Planck-Institut für Biochemie in the group of Hermann Heumann. In this chapter only the basic steps of the sample preparation are shown. A more detailed description of the protein preparation and purification can be found in the appendix or described in literature[72, 73, 74].

5.1 *Bacteria Growing and Protein Purification*

The chaperonins GroEL and GroES were expressed in different *E.coli* strains (W3110, JM109, MRE600) bearing the multicopy plasmid p0F39. The cells were grown in LB media and collected by centrifugation. The deep frozen cells (-80°C) were thawed in lysis buffer and disrupted using a French Pressure Cell. The cleared lysate was applied to several chromatographic steps and the different fractions were controlled by gel-electrophoresis. The GroEL and the GroES fractions were separated and purified separately. The rather diluted GroEL fractions were re-concentrated by ultrafiltration, using a 10kDa cutoff-filter, and applied to a gel filtration. After a second re-concentration step the GroEL was finally purified by "active red" agarose column (available from Sigma).

The GroES fractions were incubated at 56°C 10-20min. The precipitated material was removed by centrifugation (20000 x g, 1hour, at 4°C). The remaining GroES in the supernatant is about 90% pure. The final purification was done using additional chromatographic steps.

The yields of the pure proteins are for the GroEL 10-20mg per 1g *E.coli* cells and for the GroES 3-4mg per 1g cells.

5.2 *Control of the Protein Purity*

The purification of the chaperonin is impeded by the ability of the GroEL to bind denaturated protein. These non-native proteins stick to the chaperonin and interfere with the binding properties of GroEL to nucleotides and substrate protein. For structural analysis these impurities have to be removed. Especially the last purification step, using the active red column, eliminates these damaged proteins, but the final GroEL has to be controlled before further experiments can be done. This quality control can be done by fluorescence measurements of the proteins.

Despite the large number of 548 amino acid residues per subunit the wild type GroEL contains no tryptophane residue. Assuming that the bound substrate proteins contain tryptophane, the fluorescence response of the protein at 280nm excitation wavelength can be used for the control. This procedure is based on the energy transfer from the excited tyrosine at 280nm to the tryptophane residue. Thus the ratio of the emitted light at 305nm to the emitted light at 350nm is a very sensitive value for the purity of the GroEL. The emission spectra of a GroEL fraction before the "active red" column and afterwards are shown in the figure 5.1.

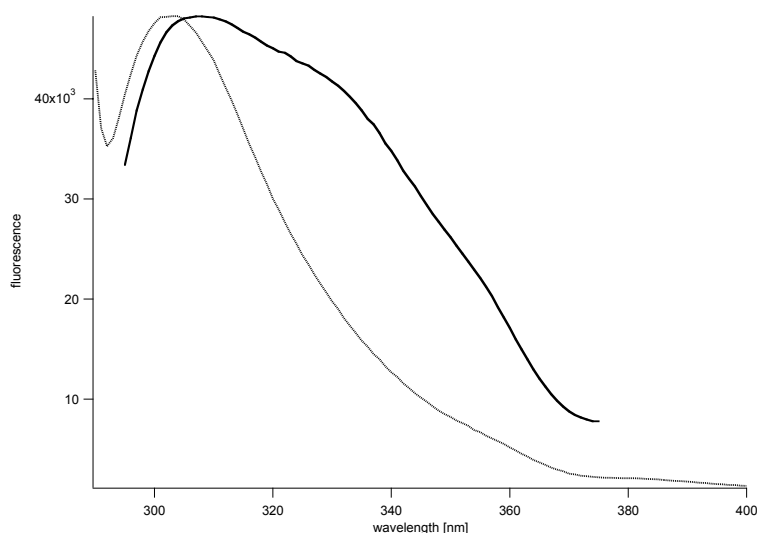


Fig. 5.1: Improvement of the purity of GroEL. The solid line indicates the emission spectra before the "active red" column and the dashed line afterwards.

The improvement of purity is indicated by the reduction of the ratio $\frac{f_{305}}{f_{350}}$ from 1.8 for non-purified to 5.8 for the purified GroEL.

5.3 Control of the Protein Activity

In order to exclude protein inactivation due to the different purification procedures the activity of the purified protein has to be proven. The following specifications were made for the activity of the chaperonins. Firstly the co-chaperonin GroES should still be able to bind to the GroEL, and secondly the GroEL ATP-ase activity should not be disturbed. The binding competency of the chaperonin system was monitored by gel-electrophoresis. GroEL was incubated in the presence of ADP with different concentrations of GroES. The ratio of GroES to GroEL was varied from 0 to a 3-fold excess and applied to a non-denaturing gel. The result of this analysis is shown in fig. 5.2.

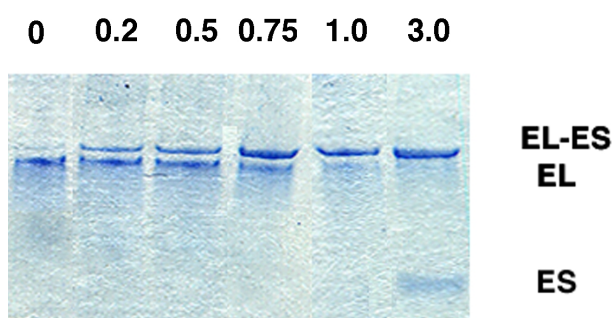


Fig. 5.2: Titration of GroEL and GroES. The ratio GroES to GroEL was varied from 0 to 3. The three visible bands indicate the complete binding at 1:1 ratio.

In the gel picture the three bands for the GroEL, the GroES and the asymmetric GroEL-GroES complex can be identified. The first band on the left is the GroEL band without GroES. The next lanes of the gel show the binding of the GroES to the GroEL, whereas all GroEL and GroES are formed

to the complex under a ratio of 1. From this data the competency of the two proteins for the binding reaction is proven.

The ability for the ATP-hydrolysis can be monitored by the production of ADP in the ATP-ase cycle of the GroEL. For this experiment radioactive labeled ATP was used. The radioactive label is on the α -phosphate, which is not subsected by the hydrolysis reaction. The nucleotide and the GroEL were mixed and the reaction was stopped after various time points by denaturing the protein. The nucleotides were separated by thin-layer chromatography, which was analysed on an image plate afterwards. The amount of produced ADP was re-calculated from the initial ATP concentration. The figure 5.3 shows the time progression of the ADP production within 17min.

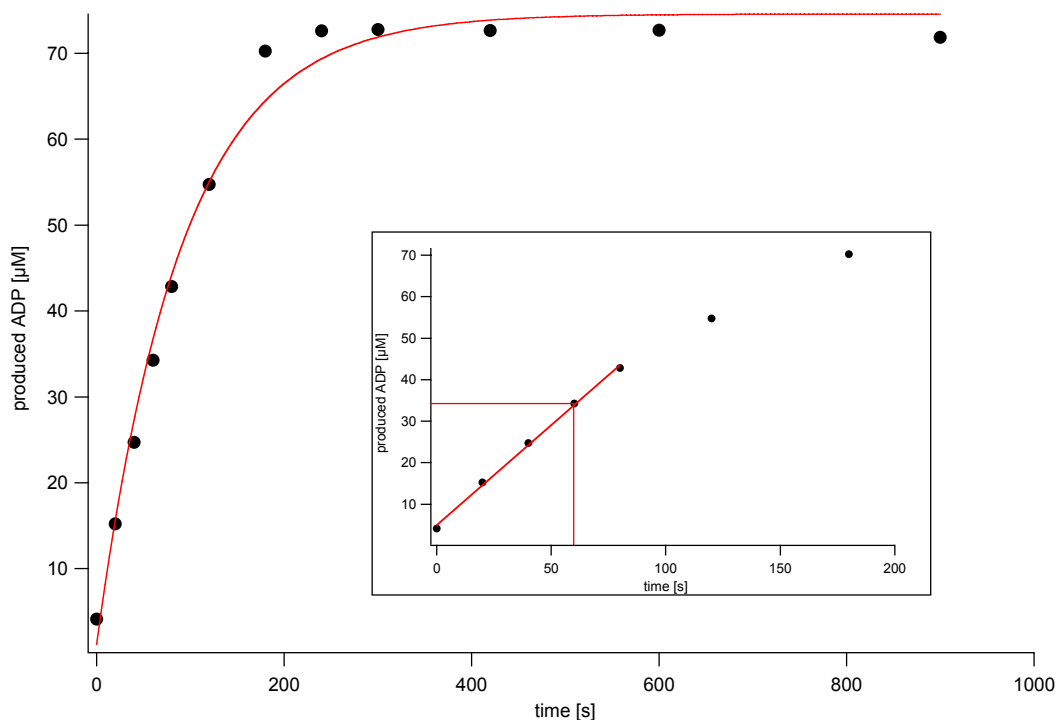


Fig. 5.3: Production of ADP by hydrolysis of ATP. The linear part of the data is shown in the inset.

The initial ATP concentration was $80\mu\text{M}$ and the GroEL was $0.7\mu\text{M}$ GroEL 14-mer. The inset in figure 5.3 shows the linear steady state phase of the hydrolysis reaction. From this plot an ADP concentration of $35\mu\text{M}$ after 60s could be derived. This led to a production rate of $0.58\mu\text{M ADP per s}$. Taking into account that only one heptameric ring can hydrolyse seven ATP in one cycle the derived rate is $\approx 0.12\text{s}^{-1}$. This finding is in line with other biochemical investigations.

The two quality controls showed that the proteins were in a fully functional state and could be used for further experiments.

6. RESULTS

The GroEL nucleotide cycle. Formation of the asymmetric GroEL-GroES complex. The asymmetric complex mixed with nucleotides, the system becomes dynamic

For the investigation of the chaperonin "two stroke motor", the kinetics of the chaperonin system with nucleotides was observed. For this the two syringes of the stopped-flow apparatus were loaded with different reactants, mixed rapidly and exposed to the X-ray beam as described above. Nucleotides were loaded together with the GroES, because GroES do not bind nucleotides and shows no ATP-ase activity. Therefore, two syringes for the mixing were sufficient. After radial integration and background subtraction the 1-dim data was averaged over four experimental datasets. This data was applied to an analysis procedure, calculating the radius of gyration (R_g), the scattering intensity at $q=0$ (\sim molecular weight) and the distance distribution function $p(r)$. These data for the first experiment, GroEL mixed with buffer as reference, is shown in the next pictures.

The Reference: GroEL mixed with buffer

The resulting scattering intensities are presented in Fig. 6.1. For a better overview the error bars were not printed, but are presented for one scattering function in Fig. 6.2.

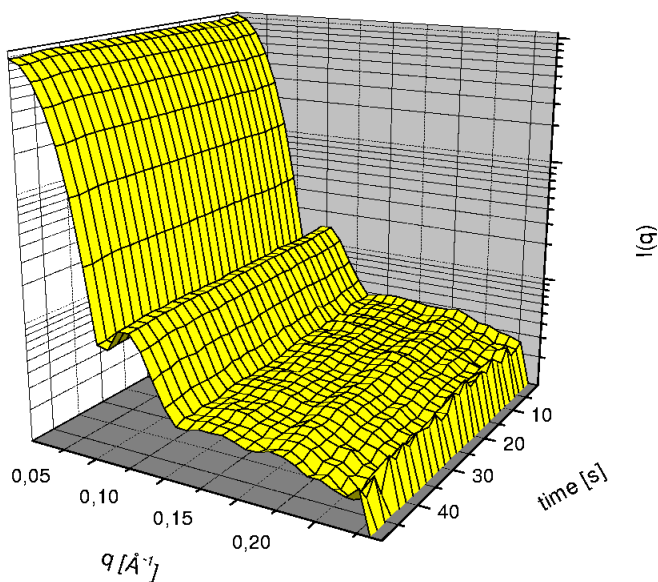


Fig. 6.1: Time resolved small angle X-ray scattering intensities for the GroEL-Buffer reference.

The scattering data show good statistics quality. The exposure time was 150ms for one single

scattering pattern. The characteristic minima at $\approx 0.07 \text{ \AA}^{-1}$, and the side maxima at $\approx 0.1 \text{ \AA}^{-1}$ are clearly visible. The estimated errors are in the range of 2%. This quality is as good as for data obtained at other SAXS beamlines with a factor of $10\text{-}10^4$ prolonged exposure times.

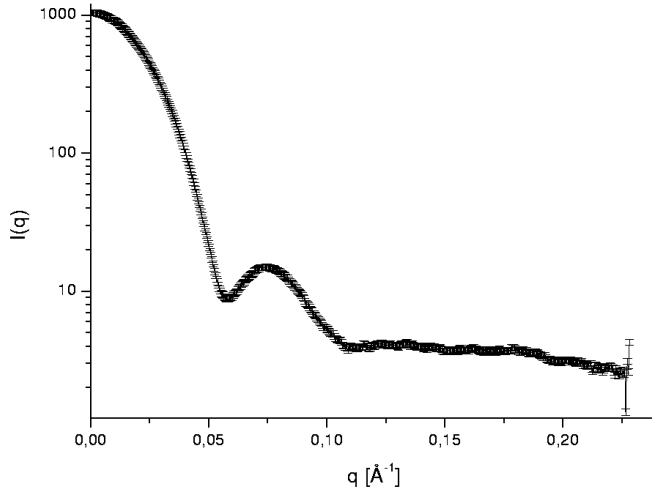


Fig. 6.2: Estimated errors for the scattering data in fig. 6.1.

From this data the radius of gyration and the molecular weight can be calculated using the straight forward Guinier approximation. The results from this linear fitting procedure versus time are presented in fig. 6.3 and 6.4.

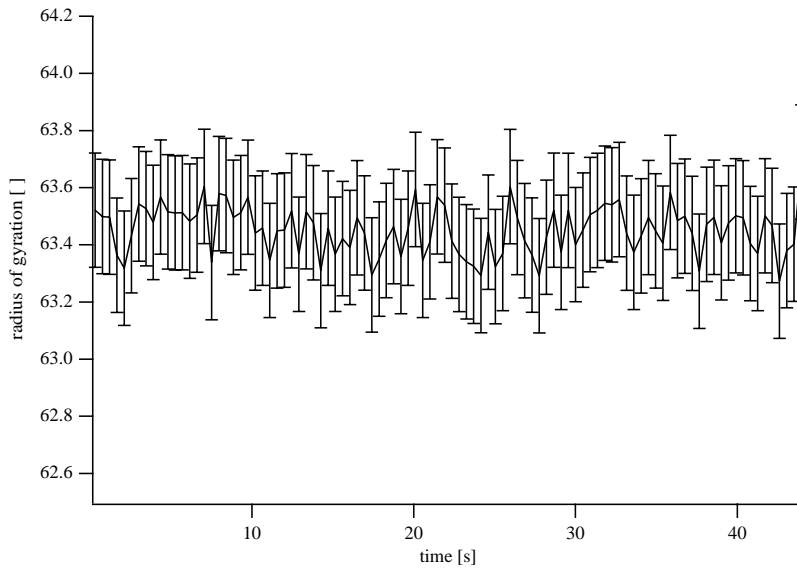


Fig. 6.3: The time progression of the radius of gyration for the GroEl-Buffer (reference)

The radius of gyration is stable over the whole time course within the errors ($R_g \approx 63.5 \text{ \AA} \pm 0.2 \text{ \AA}$). The radius of gyration is about 2% higher than known from small angle neutron scattering and from

model calculations. A possible reason for these deviations is small protein aggregations, as visible in the distance distribution function (see fig. 6.6).

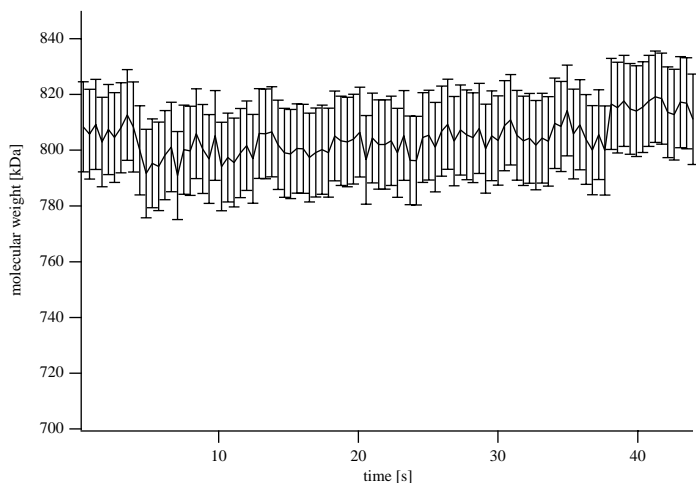


Fig. 6.4: The time progression of the molecular weight of GroEl-Buffer (reference)

The molecular weight is also stable ($MW \approx 800\text{kDa} \pm 20\text{kDa}$), but with large errors. The molecular weight was recalculated from the scattering intensity at $q=0$ using the Guinier approximation. The problem in this case is the less stable measurement of the flux. During the Guinier approximation the errors increased due to the logarithmic regime of the fit procedure. Therefore, the molecular weight was not analyzed in the further experiments. In the second step of the analysis the scattering intensities $I(q)$ were integrated using the **Debye** formular by the direct transformation method described in the chapter "Data Reduction, Treatment and Analysis". Fig. 6.5 shows the Fourier transformed scattering intensities from fig 6.1. One representative with the estimated errors, compared with a model calculation for GroEL, is shown on the right side of fig. 6.6.

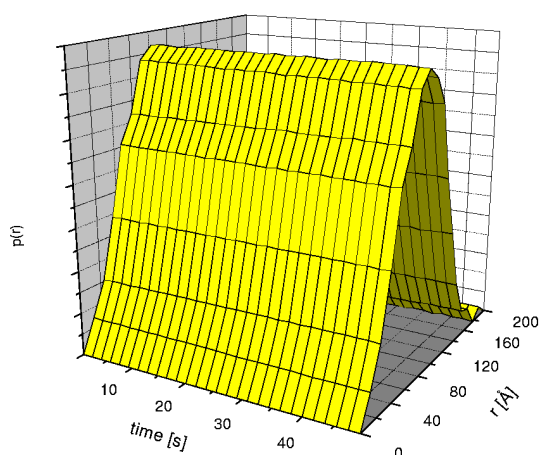


Fig. 6.5: Calculated distance distribution functions for the GroEL reference. The estimated errors are printed for one representative in figure 6.6.

The $p(r)$ -functions shows a smooth surface indicating no structural changes of the molecule by

mixing with buffer. This finding is in line with the results of the R_g -values and the molecular weight. A comparison of $p(r)$ functions derived from the experimental data, and from model calculations based on the crystal structure, shows a good agreement within the errors. In the higher r -region of the function (between 150\AA and 180\AA), a small amount of protein aggregation is visible.

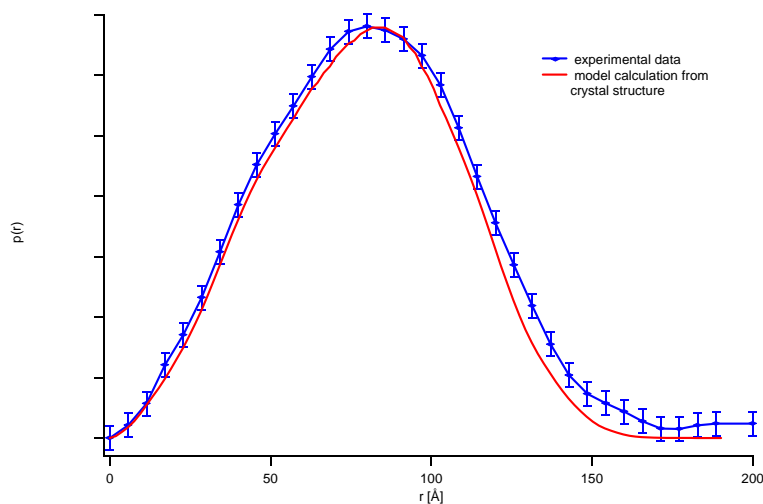


Fig. 6.6: $p(r)$ function with estimated errors from fig. 6.5. Also the comparison with a $p(r)$ calculated from the crystallographic model shows a good agreement.

6.1 The main Chaperonin GroEL nucleotide cycle - without GroES

For the investigation of the dynamic GroEL nucleotide cycle, the first step of the chaperonin "two-stroke" mediated refolding process, mixing experiments with the following nucleotides were performed:

1. GroEL mixed with ADP
2. GroEL mixed with ATP ($c_{ATP}=0.05\text{mM}$ final concentration = single turnover)
3. GroEL mixed with ATP ($c_{ATP}=0.5\text{mM}$ final concentration = 10-fold multiple turnover)

The final GroEL concentration after mixing was $c_{GroEL}=6.25\mu\text{M}$ (resp. $c_{subunit}=87.5\mu\text{M}$ for the GroEL subunits) in all three experiments. In order to explore a concentration dependent kinetic and binding behavior, the ATP concentrations were varied between 0.05mM and 0.5mM (final concentration). In these experiments one syringe of the stopped-flow apparatus was loaded with GroEL, and the second syringe with a mixture of GroES and nucleotide.

6.1.1 GroEL mixed with ADP

The binding of ADP to the GroEL heptadecamer is a fast process, with an apparent binding constant of $k_{App} = 2.5\mu\text{M}$. For this reason the binding of ADP to the GroEL is not visible by time resolved small angle scattering.

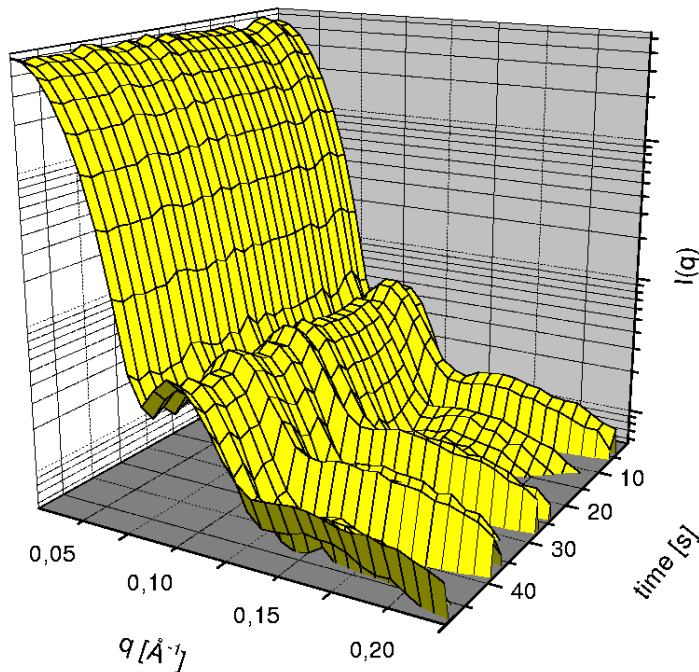


Fig. 6.7: Time resolved small angle X-ray scattering intensities for the GroEL mixed with ADP.

The scattering intensities were averaged over two experiments. Therefore the statistic is not as

good as for the GroEL reference. Hence, the typical minima and side maxima are still visible. Larger deviations are visible only in the outer part of the $I(q)$ at higher q -values (See fig. 6.7 & 6.8).

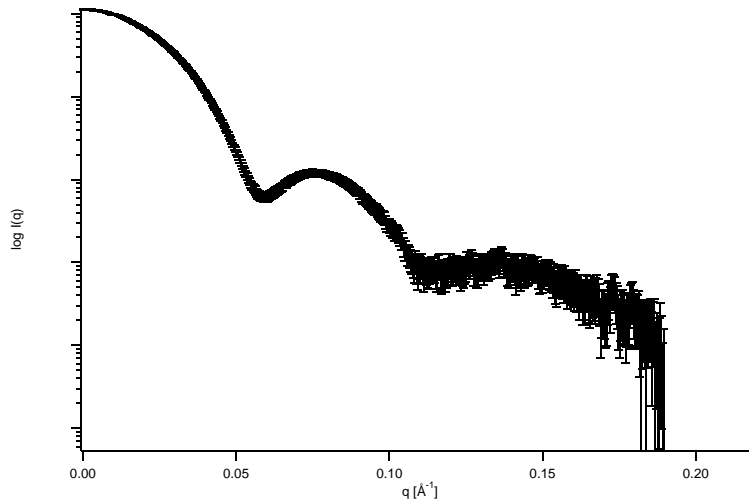


Fig. 6.8: $I(q)$ function from 6.7 with estimated errors. Due to the less number of independent experiments for the averaging the data show larger errors.

Nevertheless, the data was sufficient to calculate the R_g -values, as well as the $p(r)$ functions. The result of the direct Fourier transformation analysis is shown in the next figure (fig.6.9).

The estimated errors for one representative of the the distance distribution function from fig. 6.9 are shown in fig. 6.10.

Due to the bad statistics, the time progression of the radius of gyration in fig. 6.11 shows large errors, but is stable at about the same value as detected for the unbound GroEL ($R_g \approx 63.5 \text{ \AA} \pm 0.3 \text{ \AA}$).

For a better discrimination of the data of GroEL mixed with ADP and GroEL mixed with buffer, a differential $\Delta p(r)$ was calculated, by substracting the GroEL-ADP state from the GroEL-reference state. This $\Delta p(r)$ function is shown in figure 6.12.

The differentcial $\Delta p(r)$ functions only shows statistical deviations from the zero-level. This is in line with the values of the radius of gyration, which are in the same range for the two different states.

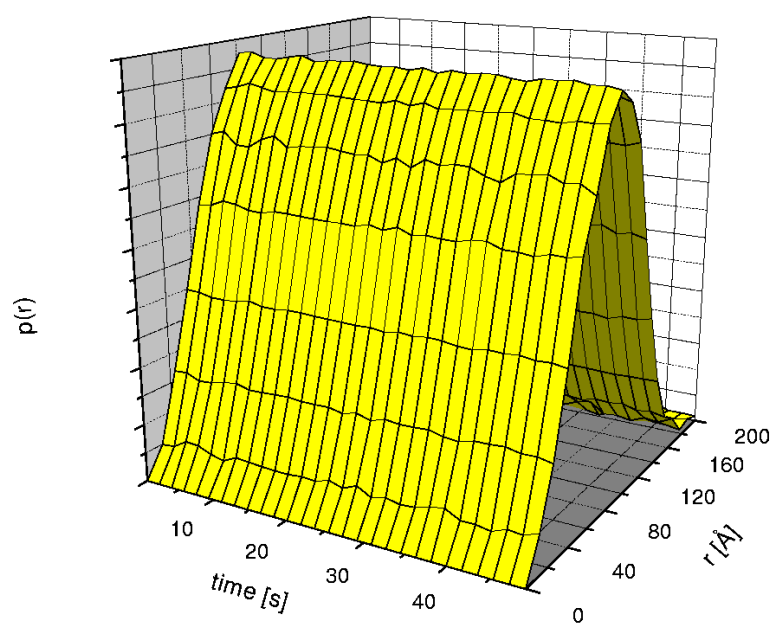


Fig. 6.9: The direct Fourier transformed $p(r)$ -functions calculated from the scattering intensities for fig 6.7.

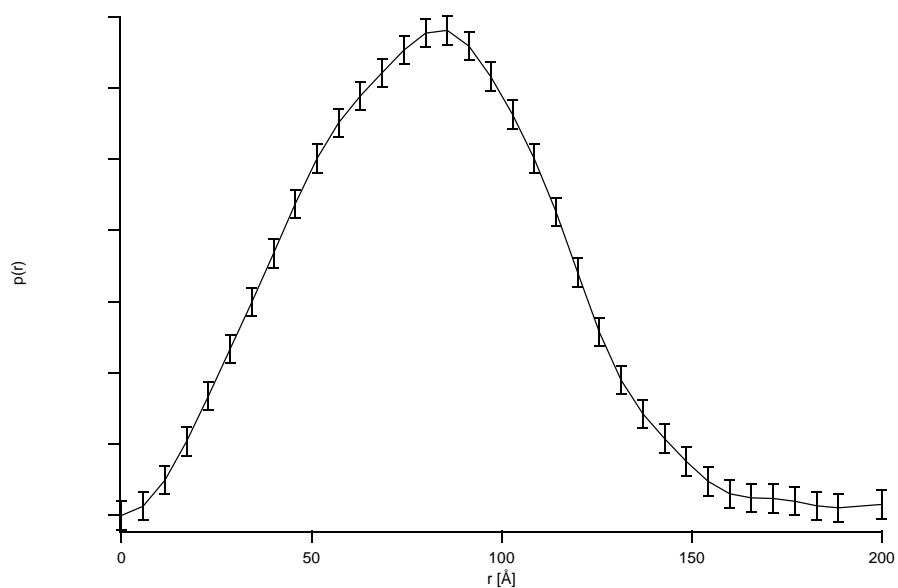


Fig. 6.10: $p(r)$ function with estimated errors for the mixing experiment GroEL+ADP.

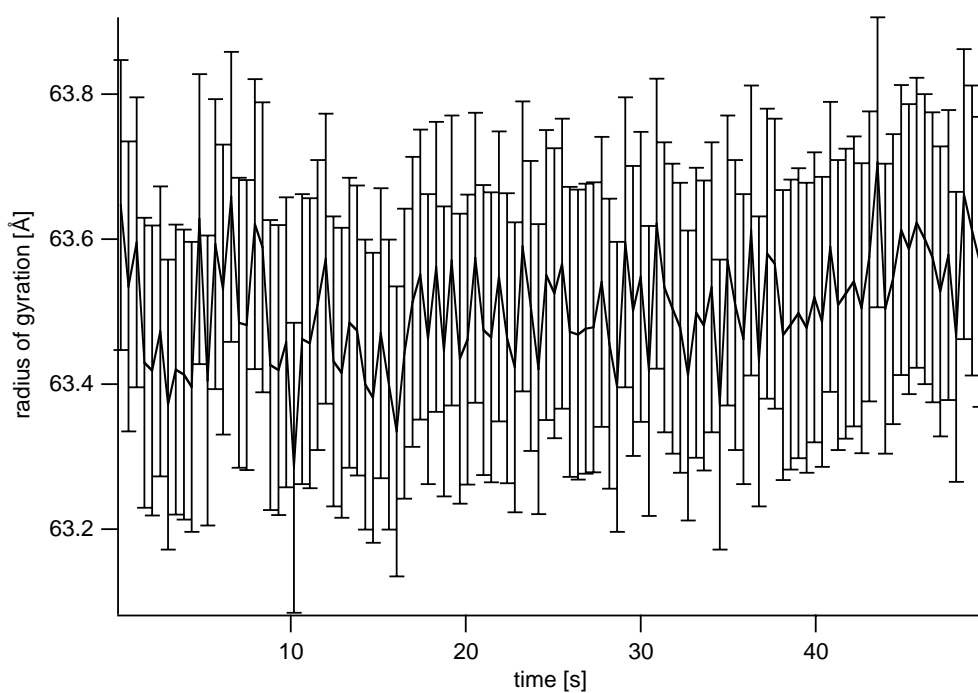


Fig. 6.11: Time resolved analysis of the radius of gyration for GroEL mixed with ADP.

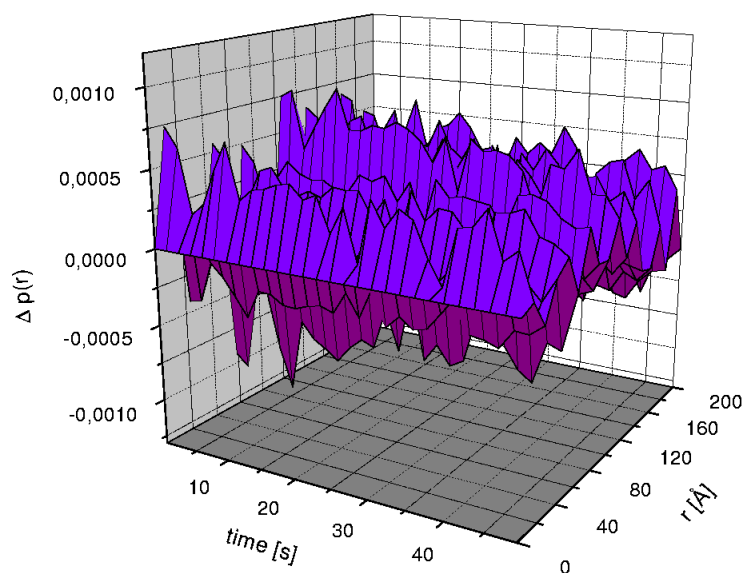


Fig. 6.12: Difference $p(r)$ function of the GroEL reference and the GroEL mixed with ADP. Only background noise is visible.

6.1.2 GroEL mixed with ATP

From biochemistry it is known, that the system GroEL-nucleotides becomes dynamic if ATP is bound to the GroEL nucleotide binding pockets instead of ADP. Furthermore, ATP introduce the cooperativity between the two heptameric rings of the GroEL barrel.

GroEL in the presence of a single turnover ATP concentration (0.05mM)

For the investigation of the GroEL hydrolysis cycle firstly a ATP concentration sufficient for only one hydrolysis cycle was chosen. Taking into account that only one GroEL heptameric ring is able to hydrolyse, while the other ring is blocked for hydrolysis, the ATP concentration of 0.05mM is sufficient for only one hydrolysis cycle (single turnover conditions). After the hydrolysis step the GroEL should remain in the ADP bound state. Four data sets were taken and averaged for getting better statistics. In figure 6.13 the averaged scattering intensities for this experiment are shown.

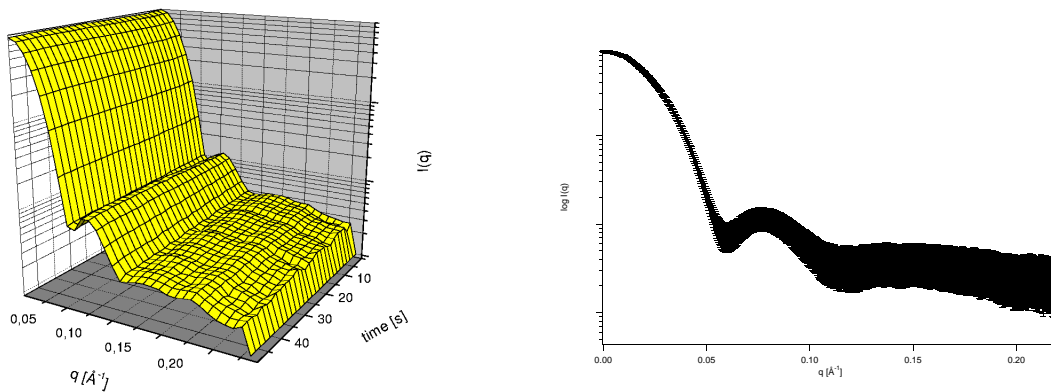


Fig. 6.13: $I(q)$ functions of GroEL mixed with a single turnover ATP concentration ($c_{ATP}=0.05\text{mM}$) after mixing.

The statistic of the experimental data is as good as for the data obtained for the GroEL reference. The extrema are visible with high precision. From this data sets for the R_g and the $p(r)$ were obtained. The $p(r)$ functions (fig. 6.14) derived using the direct transformation procedure shows a very good

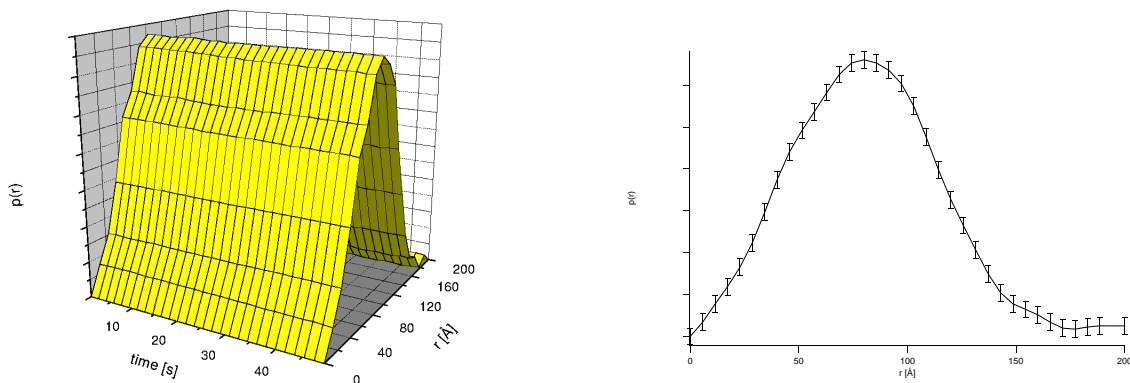


Fig. 6.14: $p(r)$ functions of GroEL mixed with a low ATP concentration ($c_{ATP}=0.05\text{mM}$) after mixing.

statistics.

The radius of gyration shows a bi-phasic behavior and is decreased immediately after mixing with ATP to $\approx 63.2\text{\AA}$ compared to the R_g -value of 63.5\AA for the non liganded GroEL. This conformational change of the GroEL shows no visible binding kinetics within the first seconds.

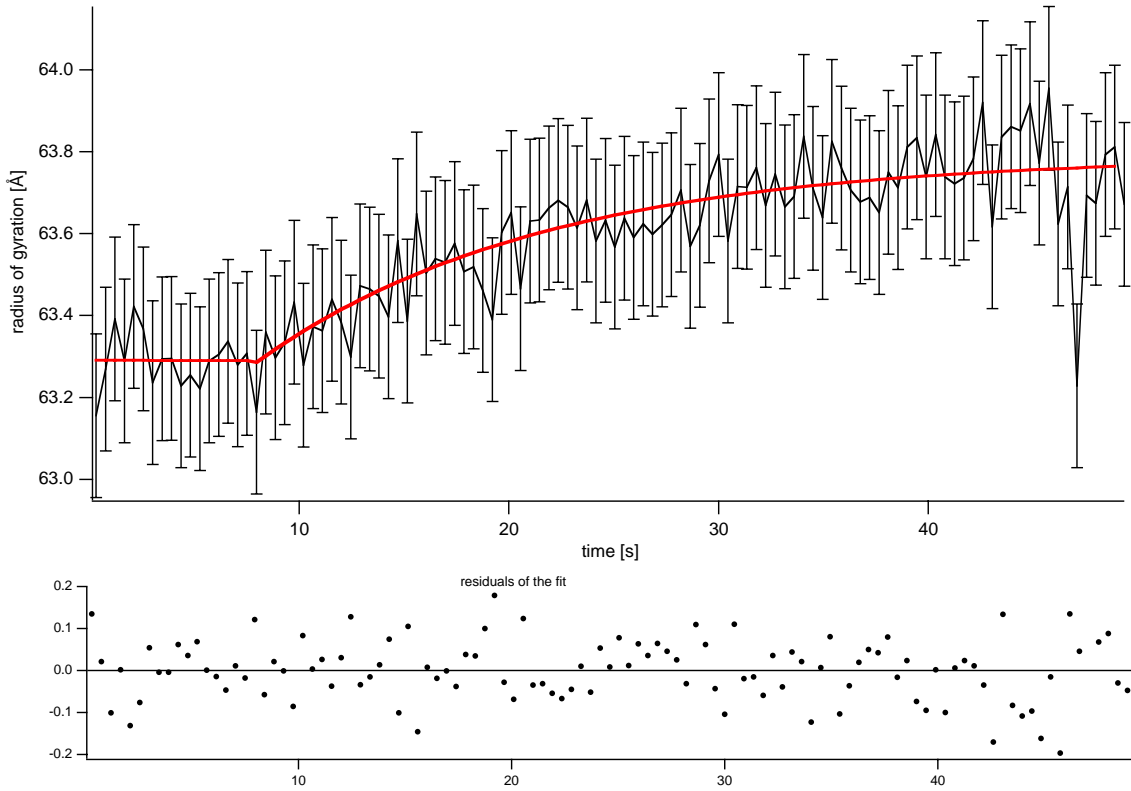


Fig. 6.15: Radius of gyration for GroEL mixed with a single turnover ATP concentration, calculated from the data from fig.6.13.

After a phase with stable R_g -values the systems relaxes back to $\approx 63.6\text{\AA}$, the value found for the GroEL-ADP₇ state. The relaxation reaction can be fitted to an exponential function, and a time constant of $k_{Rel} = 0.08\text{ s}^{-1}$ was obtained. From this bi-phasic data a hydrolysis cycle consisting of at least two different conformational states can be assumed. Firstly the ATP binding and hydrolysis state, which is formed immediately after the mixing and the GroEL_{ADP} relaxed ground state. It is remarkable, that the relaxation of the GroEL ATP binding and relaxation start after 8s. Since small angle scattering averages over a whole ensemble of molecules, the binding and the relaxation seems to be a highly coordinated and cooperative process.

As for the mixing experiment GroEL with ADP, the $p(r)$ data are sufficient to calculate the difference $\Delta p(r)$. As described above the GroEL reference (GroEL mixed with buffer) was used for the subtraction.

An interesting feature appears in the differential $p(r)$ function between GroEL-reference and GroEL with ATP. The $\Delta p(r)$ shows a modulation of distances at 120\AA . A peak at 120\AA rises immediately after the mixing and decays within the next 30s (see fig. 6.16).

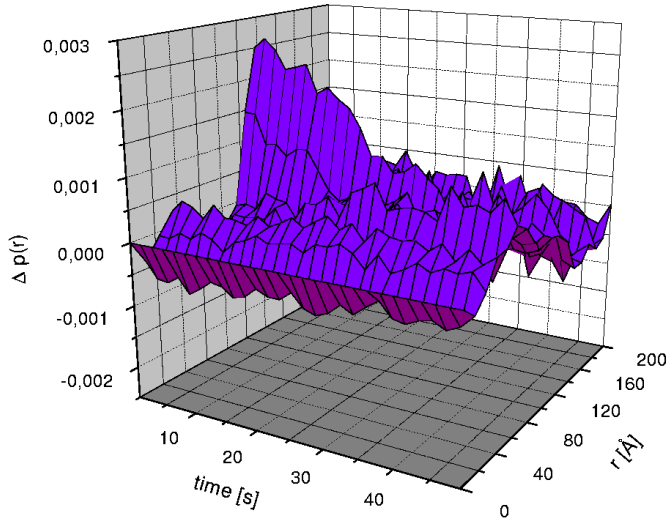


Fig. 6.16: Difference $p(r)$ function of the GroEL reference and the GroEL mixed with low ATP.

The next fig. 6.17 shows the detailed time drive of the distance at 120Å. The other distances are in the range of the zero-noise level.

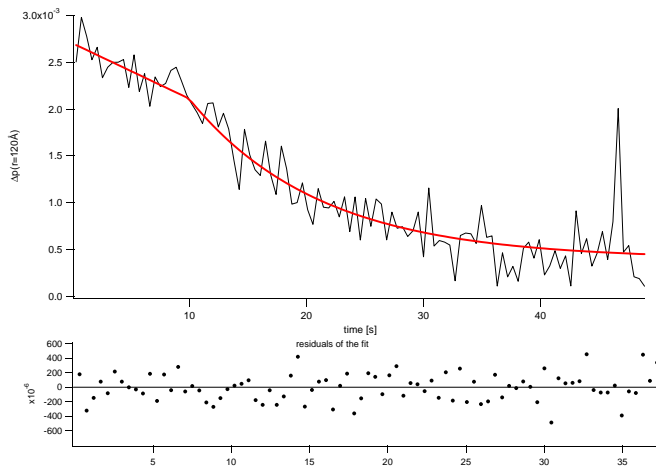


Fig. 6.17: Time progression of the distance $r=120\text{\AA}$.

The deviation of the distances show, such as the R_g -values no binding kinetics. The maximal deflection arise immediately after the mixing. This fast changes in the R_g -value and in the $\Delta p(r)$ indicates that all investigated GroEL molecules are switched to a different state within the first data point at 300ms. A linear decay starts directly, but a second phase of the decay can be observed after $\approx 10\text{s}$. The second phase was fitted to an exponential function, resulting in a ($k_{dec} = 0.09\text{s}^{-1}$) and levels of at $\approx 35\text{s}$. Also this bi-phasic behavior supports the existence of two different conformational state.

GroEL in the presence of a high ATP concentration (0.5mM=multi turnover)

The experiment with higher ATP concentrations ($c_{ATP}=0.5\text{mM}$), the GroEL subunits were allowed to make more than one ATP-hydrolysis cycle (10-fold multi turnover). After recording and averaging over four experimental sets the data were analyzed. Figure 6.18 and fig. 6.19 shows the $I(q)$ and the calculated $p(r)$ functions of this experiments.

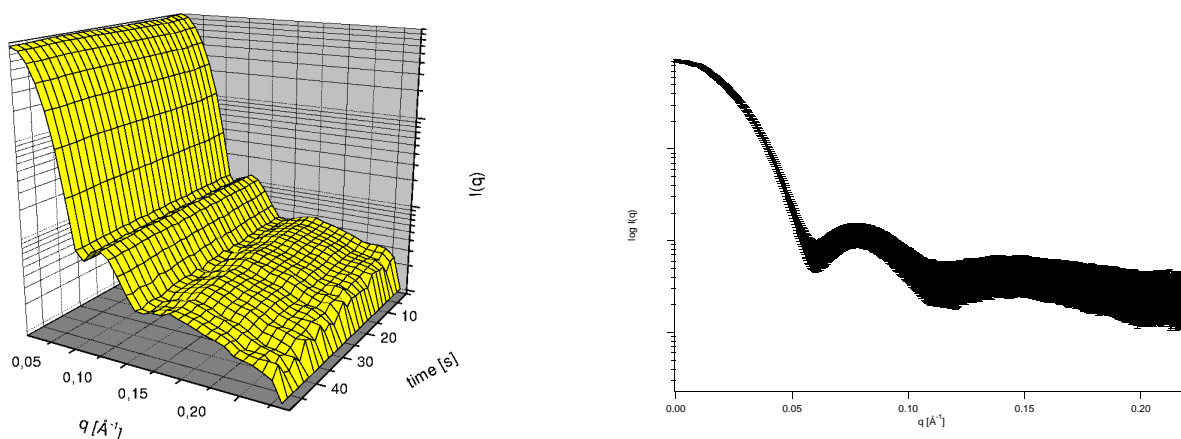


Fig. 6.18: $I(q)$ functions for GroEL mixed with a high ATP concentration.

The very good statistics of the scattering intensities $I(q)$ is reflected in a set of smooth $p(r)$ functions. From the $I(q)$ function the time drive of the radius of gyration was calculated. The smooth $p(r)$ function was analysed by calculating the $\Delta p(r)$ function between the GroEL-reference and the derived $p(r)$ data.

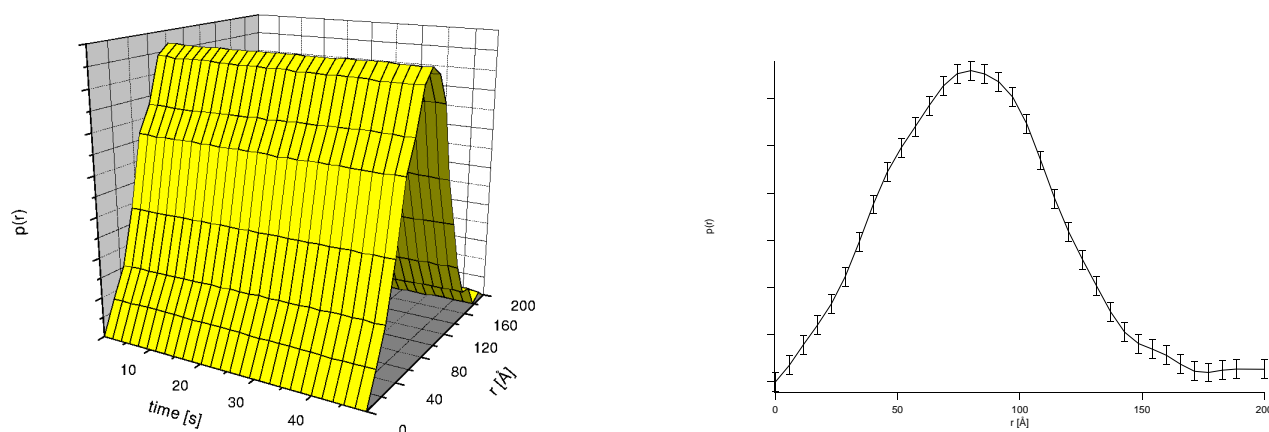


Fig. 6.19: $p(r)$ functions for GroEL mixed with a high ATP concentration.

The calculated R_g -values for this multiple ATP-cycling experiment shows an interesting modulation in time. Like the time progression for the single turnover experiment are the R_g -values decreased directly after the mixing and shows no binding kinetics.

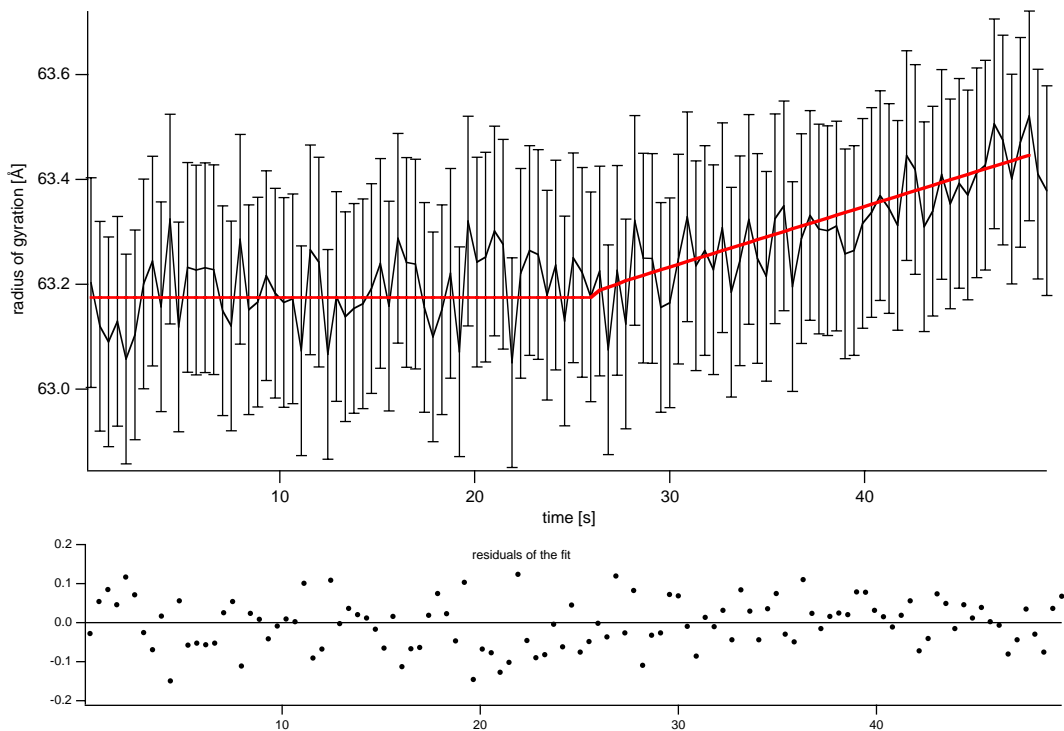


Fig. 6.20: Time drive of the radius of gyration of GroEL under high ATP concentration (0.5mM).

In the case of the multiple turnover, the relaxation is retarded to 30s. The starting of a relaxation starting after this pause and was fitted to an exponential function. For this relaxation an increased relaxation constant of $k_{Rel} \approx 0.03 s^{-1}$ was obtained. The fit function levels off at 63.6Å after $\approx 100s$ (data not shown).

Like for the mixing experiment with the low ATP concentration a differential $\Delta p(r)$ function was calculated. Using the GroEL/buffer data as reference the GroEL/high ATP experiment were subtracted.

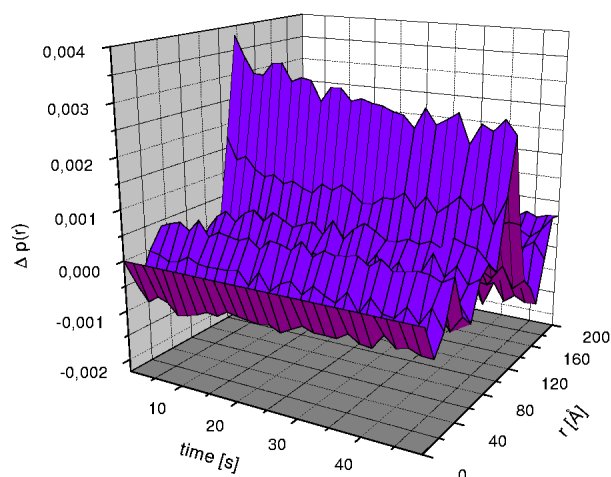


Fig. 6.21: Difference $p(r)$ function of the GroEL reference and the GroEL mixed with high ATP.

In the $\Delta p(r)$ a the peak at 120\AA arises also immediately after the mixing but does not disappear completely within the 50s experimental duration. This behaviour indicates that the complete ATP hydrolysis is not finished within the first 50s.

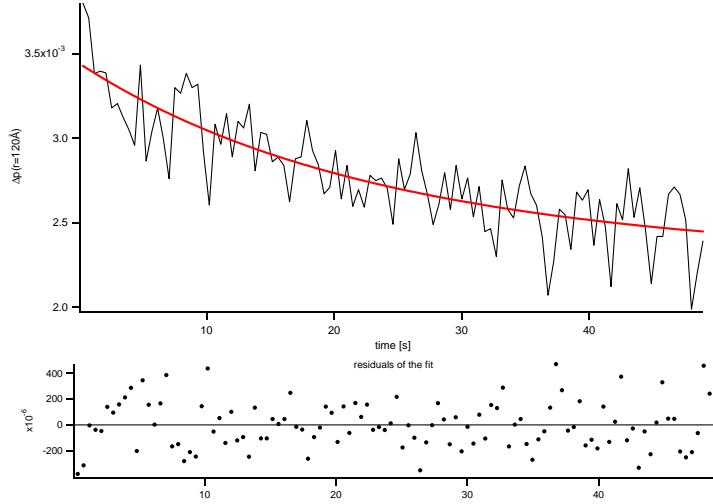


Fig. 6.22: Time drive of the distance $r=120\text{\AA}$

The data for the 10-fold ATP concentration can be fitted to a single exponential function ($k_{dec} = 0.02\text{s}^{-1}$), which is slower as found for the single turnover experiment ($k_{dec} = 0.09\text{s}^{-1}$). The devolution of the $\Delta p(r)$ function shows no multi-phasic behavior, such as the data for the single turnover. In the single turnover experiment a starting phase with stable Rg-values of 8s was found (fig. 6.15). From this a prolonged stable phase of 80s for the 10-fold extend of ATP can be assumed. However, the measured phase in this case is only 30s. Reason for this behavior might be the enhanced binding of of ATP to the nucleotide binding pockets.

If the distance of 120\AA can be assigned to a special distance, for instance the distances between the ATP binding pockets is difficult to interpret. The binding pockets for the ATP are located in the middle of the equatorial domain of the GroEL. The GroEL cylinder has a diameter of $\approx 140\text{\AA}$. From the crystal structure the ATP binding sites can be assumed to be located on circle of max. 140\AA diameter. The equivalent pseudo scattering particle for the isolated nucleotide binding sites would be a hollow cylinder of $\approx 140\text{\AA}$ outer diameter and a maximal thickness of 25\AA according to crystal structure. The distance distribution function of a hollow cylinder can be calculated analytically using the following formula¹:

$$p(r)_{\text{hollowcylinder}} = x_1(\arccos x_1 - x_1\sqrt{1-x_1^2}) - x_2(\arccos x_2 - x_2\sqrt{1-x_2^2})$$

with $x_1 = \frac{r}{2R_1}$ and $x_2 = \frac{r}{2R_2}$

Calculated $p(r)$ functions for hollow cylinders (thickness from 5\AA to 25\AA) are shown in figure 7.3.

¹ This formula is valid for infinitely thin plates. It is used only as a approximation for the hollow cylinder.

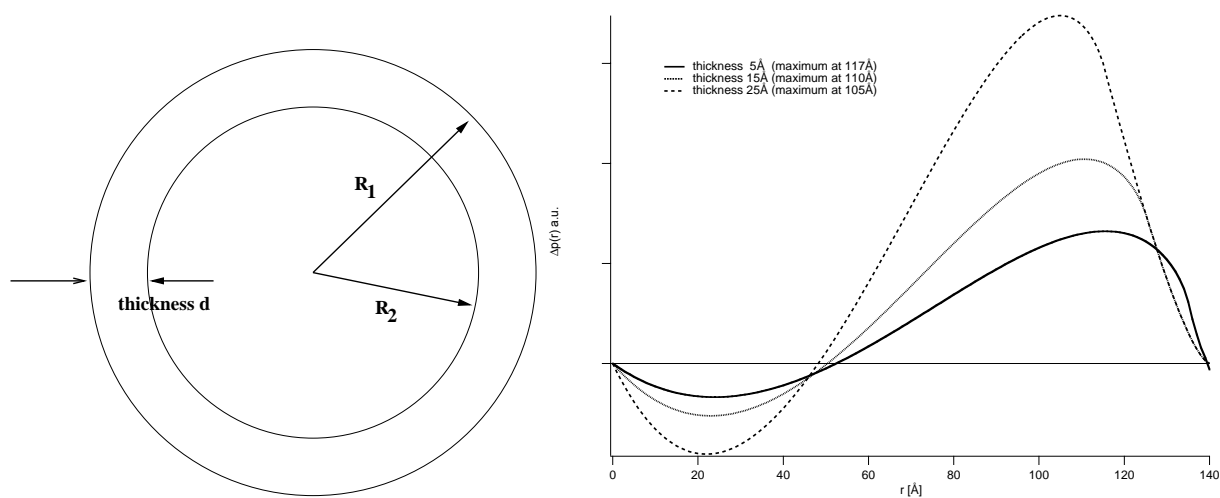


Fig. 6.23: Model calculation for the GroEL ATP binding pockets. Assuming a hollow cylinder as a model of the binding sites.

This model calculation shows that the maximum of the corresponding distance distribution function for the hollow cylinder with 5 Å thickness is ≈ 120 Å. Therefore the decay of distances at $r=120$ Å can be interpreted as changes on the ATP binding side during the hydrolysis reaction compared to the ADP bound GroEL state. For the more detailed analysis of the $\Delta p(r=120$ Å) data, crystallographic data and structures out of electron microscopy have to be used (see Discussion).

6.2 The GroEL-GroES nucleotide cycle

6.2.1 Formation of the asymmetric GroEL-GroES complex

From biochemical analysis the binding of the GroES to the GroEL in the presence of nucleotides is known. In the presence of ADP the static, asymmetric GroEL-GroES complex is stable formed, while hydrolysis of ATP should introduce a non-static and dynamic behavior. To explore this behavior the following experiments have been performed:

1. GroEL + GroES in the presence ADP
2. GroEL + GroES in the presence of single turnover ATP conditions ($c_{ATP} = 0.05mM$)
3. GroEL + GroES in the presence of multi turnover ATP conditions ($c_{ATP} = 0.5mM$)

Binding of GroES to GroEL under ADP conditions

In the presence of ADP the asymmetric GroEL-GroES complex is formed. The fast first step in this reaction is the binding of seven ADP to one GroEL heptameric ring. The binding of the GroES is the second step in this association reaction. From biochemical studies as well as from small angle neutron scattering is known that the asymmetric GroEL-GroES complex is stable several hours after the assembly. The binding reaction was followed over 50s and the data averaging over four independent sets. From this the $I(q)$, $p(r)$ as well as the radius of gyration were calculated.

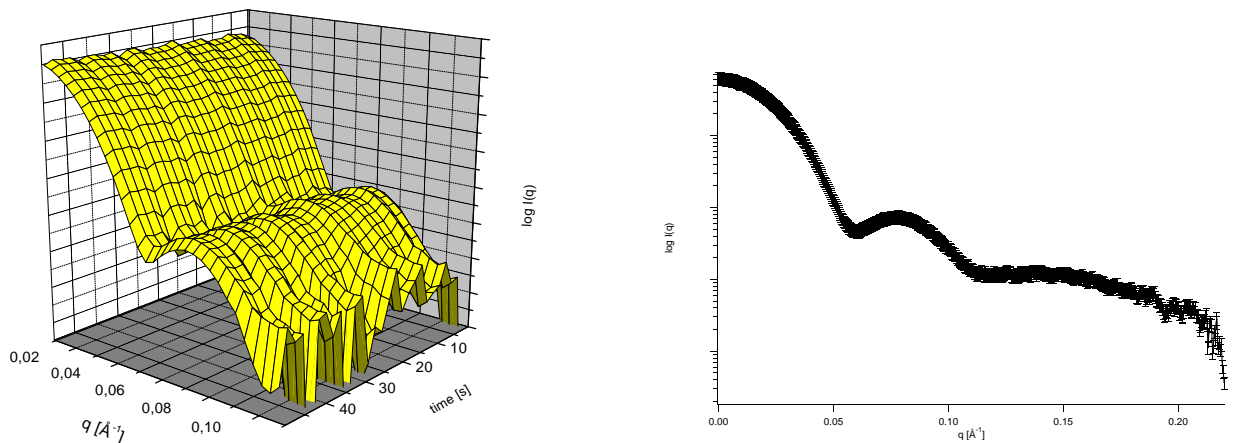


Fig. 6.24: $I(q)$ functions of GroEL mixed with GroES in the presence of ADP

The estimated errors for on scattering function obtained by this experiment is shown in the fig. 6.24. Also in this data sets the side maxima and minima are well pronounced. Based on this data the distance distribution function $p(r)$ was calculated. The result of the straight forward direct transformation is shown in fig. 6.25. Despite of the less quality of the scattering data, shows the $p(r)$ functions a smooth run.

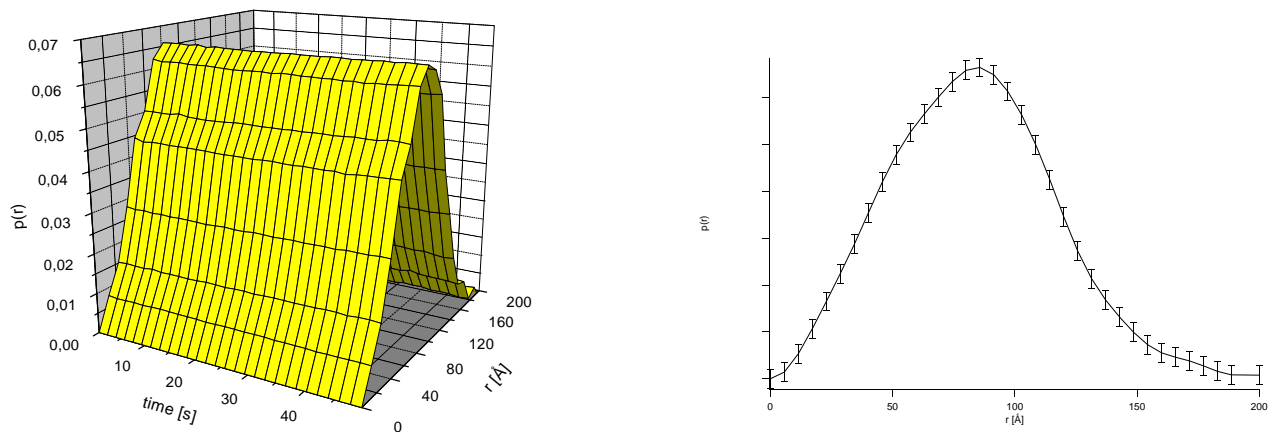


Fig. 6.25: $p(r)$ functions of GroEL mixed with GroES in the presence of ADP

The structure of the asymmetric GroEL_{ADP₇}-GroES was studied in detail with X-ray crystallography and small angle neutron scattering. A comparison of time resolved data and data from models derived from this structure is shown in fig. 6.26.

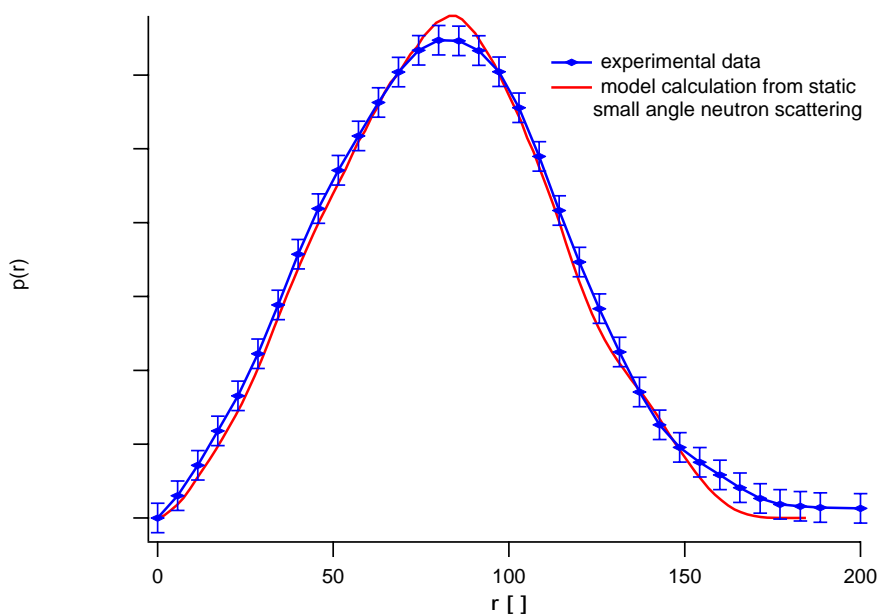


Fig. 6.26: Comparison experimental data of the GroEL-GroES complex and a model calculation based on small angle neutron scattering data.

Based on the experimental data the time dependence of the radius of gyration for the formation of the asymmetric chaperonin complex was calculated. Figure 6.27 shows this data applied to an exponential fit. The residuals indicate a proper fit and a mono-phasic binding behaviour can be estimated.

The radius of gyration increases rapidly in the first 8s from 65Å to 66.2Å, indicating the formation of the asymmetric complex. The initial Rg-value of 63.5Å for the unbound GroEL is not recordable due to a too slow data acquisition of the CCD-camera. After 8s the binding reaction is finished and the

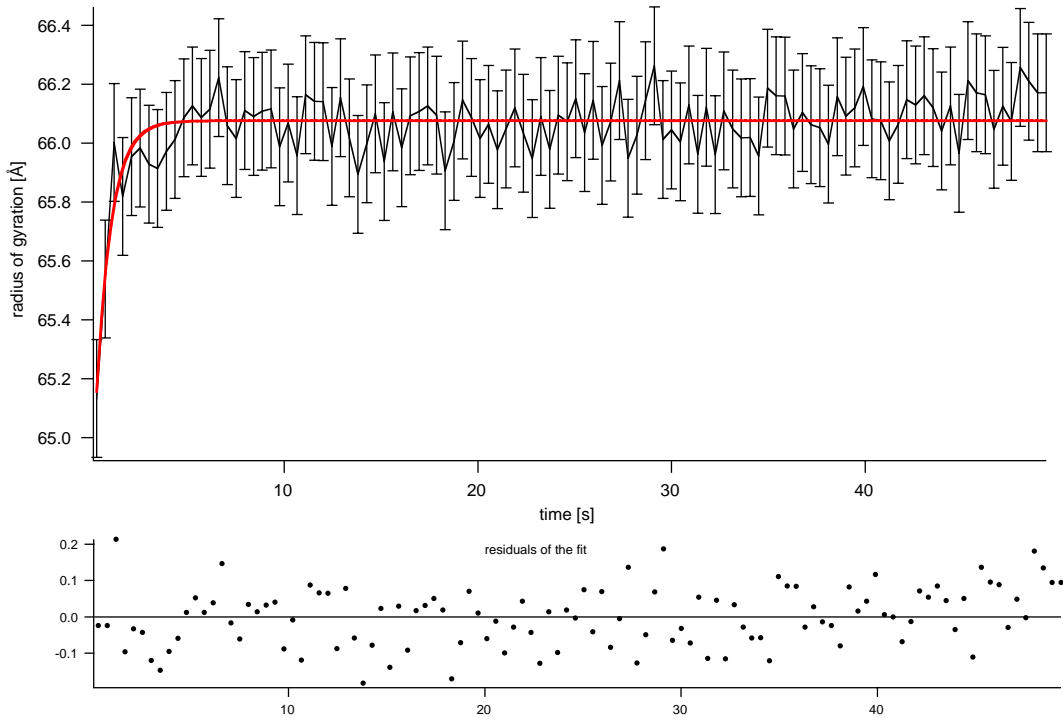
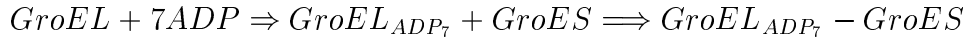


Fig. 6.27: Time drive of the radius of gyration for the conformation of the GroEL-GroES asymmetric complex.

radius of gyration remains stable (see fig. 6.27). The mono-phasic exponential fit indicates an first order reaction, which can be described by the following equations:



Whereas the first part of the reaction, the association of the ADP is not visible, can the second part be described by the following differential equation:

$$\frac{dp}{dt} = k_a b_0 a_0 =$$

$$\frac{a_0(b_0 - p)}{b_0(a_0 - p)} = e^{(b_0 - a_0)k_a t}$$

with p =concentration of the complex, k_a =first order rate constant
 b_0 and a_0 the initial GroEL/GroES concentrations

For the further analysis of this data the following assumption were made, i) the initial Rg-value is the Rg-value of the $GroEL_{ADP}$ ($=63.7\text{\AA}$) and ii) the contribution of the unbound GroES to the Rg-values is negligible. Under this assumption a *pseudo*-first order reaction can be described by the modified differential equation:

$$p(t) = b_0(1 - e^{-k_a b_0 t})$$

Applying this function to the experimental data the rate constant of this reaction can be derived by a fit procedure using a least-square fit (IgorPro; Wavemetrics). The result of this fitting procedure is shown in figure 6.28.

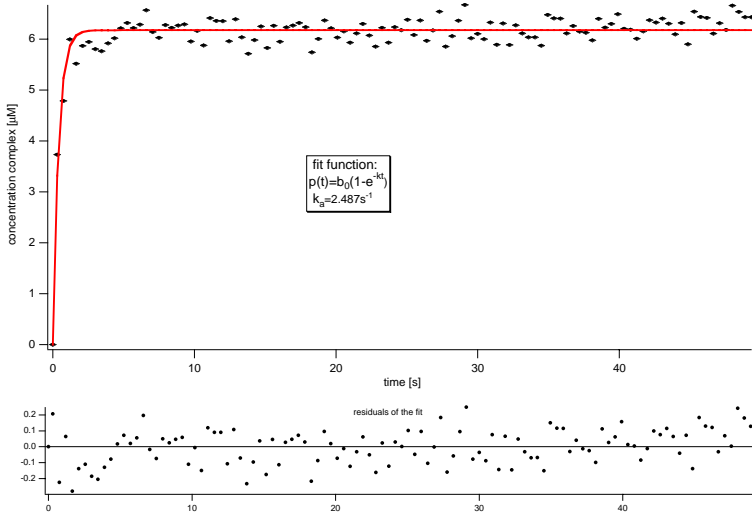


Fig. 6.28: Kinetic analysis for the formation of the asymmetric GroEL-GroES complex.

The fit results in an association constant of $k_a = 4 \times 10^5 M^{-1} s^{-1}$ ($t_{\frac{1}{2}} = 0.278 s$). This finding is in line with biochemical data.

The $\Delta p(r)$ functions were calculated from the $p(r)$ functions of the GroEL_{ADP₇}-GroES complex using the GroEL as reference. From the kinetic constants derived above a complex proportion of 60% for the first time slice at 0.306s and 90% after the second time slice at 0.756s can be estimated. Therefore the increase of the molecular weight from 800kDa (GroEL) to 870kDa (asymmetric complex) dominates the $\Delta p(r)$ from the first time point. The difference $p(r)$ between the GroEL-reference and the $p(r)$ for the formation of the asymmetric complex is shown in figure 6.29.

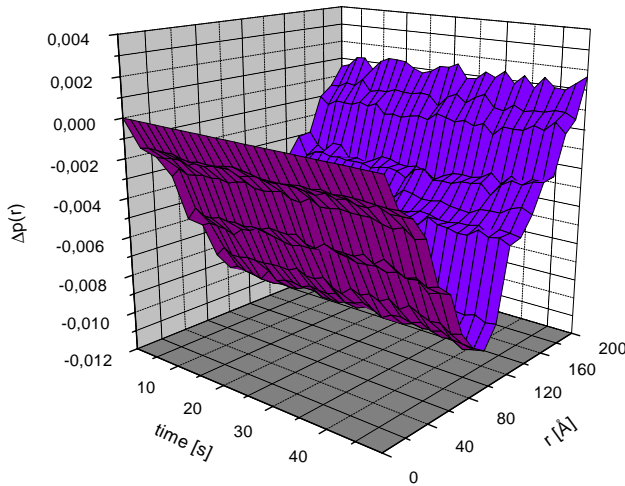


Fig. 6.29: Difference $p(r)$ function of the GroEL reference and the GroEL-GroES mixed with ADP experiment. The increase of the molecular weight from 800kDa (GroEL reference) up to 870kDa (asymmetric GroEL-GroES complex), enlarges the differences dramatically.

The differences of the GroEL and the GroEL-GroES complex are shown in the $\Delta p(r)$. The increase of the molecular weight from 800kDa to 870kDa produces huge difference between the two sets of

data. The formation of the complex can be remarked in the first $p(r)$ function only. The $\text{GroEL}_{\text{ADP}_7}$ -GroES complex was used as reference for further $\Delta p(r)$ analysis of the GroEL-GroES complexes in the presence of ATP.

Binding of GroES to GroEL in the presence a single turnover ATP concentration

While the binding of the GroES to the GroEL in the presence of ADP ends up in the static GroEL-GroES-ADP complex, this binding reaction should become a dynamic behavior in the presence of ATP. For this investigation the preformed GroEL-GroES-ADP complex was mixed with buffer containing an ATP concentration of 0.1mM. The final ATP concentration of 0.05mM was reached after the mixing; in analogy to the other experiments. Four independent experimental data sets were measured, averaged and analysed. The scattering intensities $I(q)$ as well as the Fourier transformed pair distance distribution functions $p(r)$ were presented in the figure 6.29 and 6.30. Like for the other experiments data with good

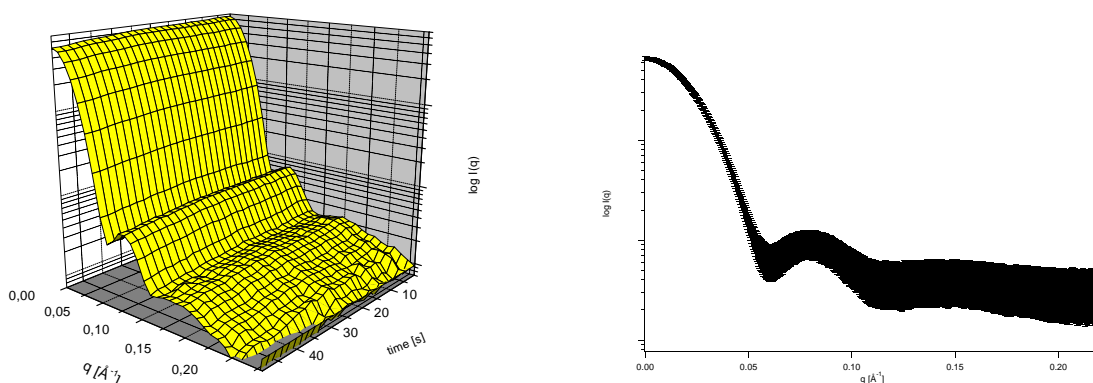


Fig. 6.30: $I(q)$ functions of GroEL mixed with GroES in the presence $0.05 \mu\text{M}$ ATP

statistics were obtained using the CCD detector set-up described in the chapter about detectors. The estimated errors are shown for one representative in the right figure.

For the further analysis the scattering intensities were Fourier-transformed and the distance distribution $p(r)$ functions are shown in fig 6.31.

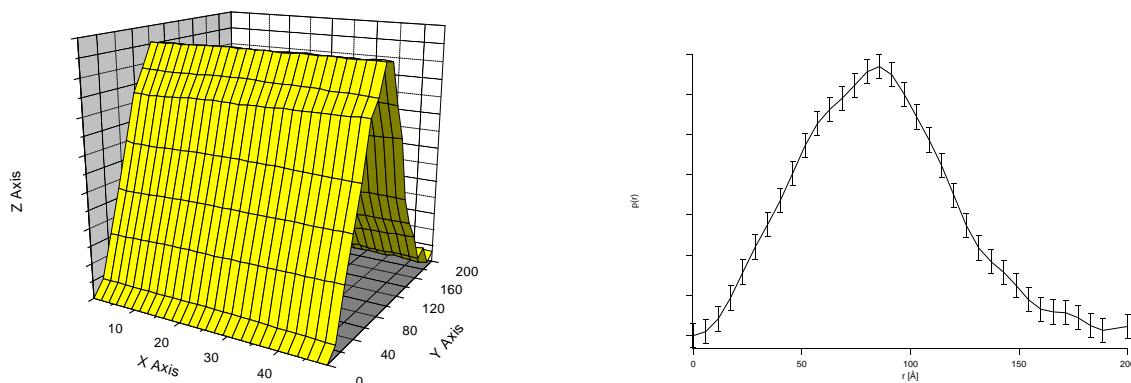


Fig. 6.31: $p(r)$ functions of GroEL mixed with GroES in the presence of single turnover ATP conditions

The radius of gyration was calculated out of the $I(q)$ functions. The result of this analysis is shown in figure 6.32.

In contrast to the binding reaction of the GroES in the presence of ADP, where the R_g -value remains stable after 8s at $\approx 66.1\text{\AA}$, the R_g -values for the binding of the two proteins in the presence of ATP show a modulation in time. While the value increases within the first 2s up to $\approx 66.8\text{\AA}$ decays this value within 26s to $\approx 66.2\text{\AA}$, and increases afterwards back to $\approx 66.6\text{\AA}$. The first phase in the multi-phasic

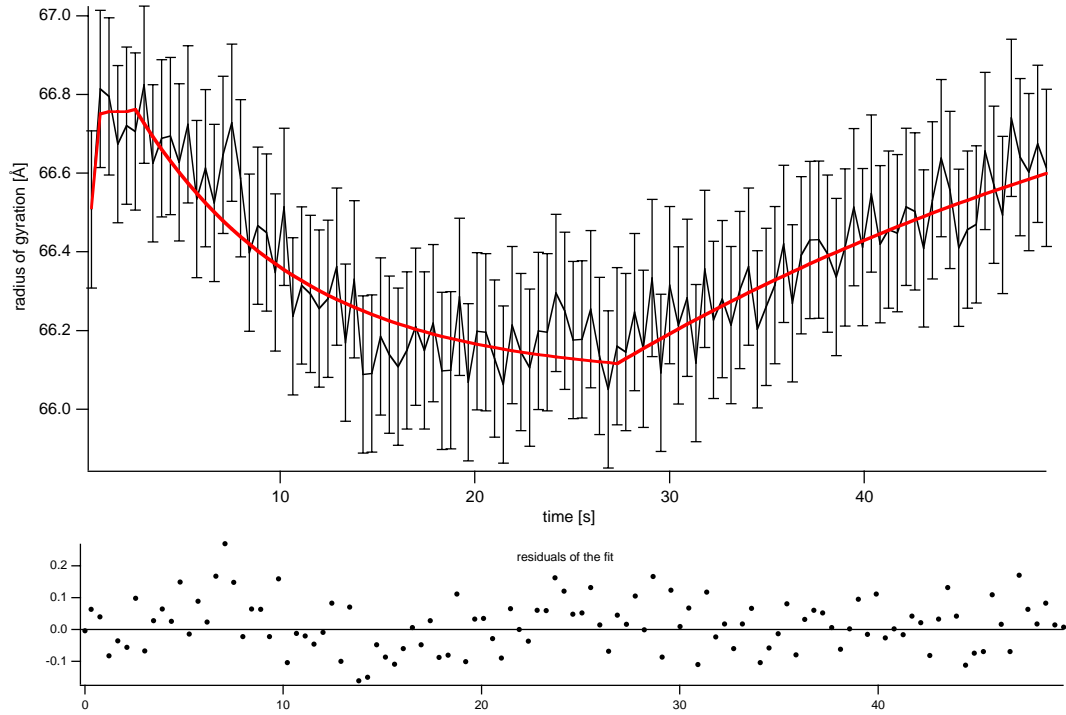


Fig. 6.32: Time progression of the radius of gyration for the conformation of the GroEL-GroES complex in the presence of a single turnover ATP concentration.

binding kinetics indicates the formation of the GroEL-GroES-ATP₇ state. After 8s this intermediate state decays within 20s to the GroEL-GroES-ADP₇ state at 66.2\AA . This decay is overridden by a slow increase up to 66.6\AA after 28s. For the kinetic constants of this binding reaction, a *pseudo*-first order reaction of the ATP and GroES can be assumed and the fit results in an association constant of $k_{Ass} = 13 \times 10^5 M^{-1} s^{-1}$. The following decay was fitted to an exponential function and a complex conversion rate of $k_{con} = 0.13 s^{-1}$ was derived. The dissociation of the GroES from the GroEL can not be observed. From the increase of the values after 28s, a rate constant $k_b = 0.05 s^{-1}$ was calculated. The end of the reaction after 50s can not be evidenced from the experimental data.

From the multi-phasic behavior of the R_g -values a multi-step process with at least three different intermediate states can be supposed. It is known from biochemical time resolved ATP-ase measurements on the GroEL-GroES complex, that the hydrolysis of the ATP starts directly after the mixing with ATP. Thus, the first transient formed structure can be identified as the ATP-hydrolysing state of the asymmetric complex. The state after the relaxation at 26s is the GroEL_{ATP₇}-GroES which appears at 66.2\AA . The formation of the third state is the rate limiting step of the ATP-cycling and arises after $\approx 50s$.

Due to the good statistics of the data a difference pair distance distribution function $\Delta p(r)$ was calculated using the asymmetric GroEL-GroES-ADP₇ complex as reference.

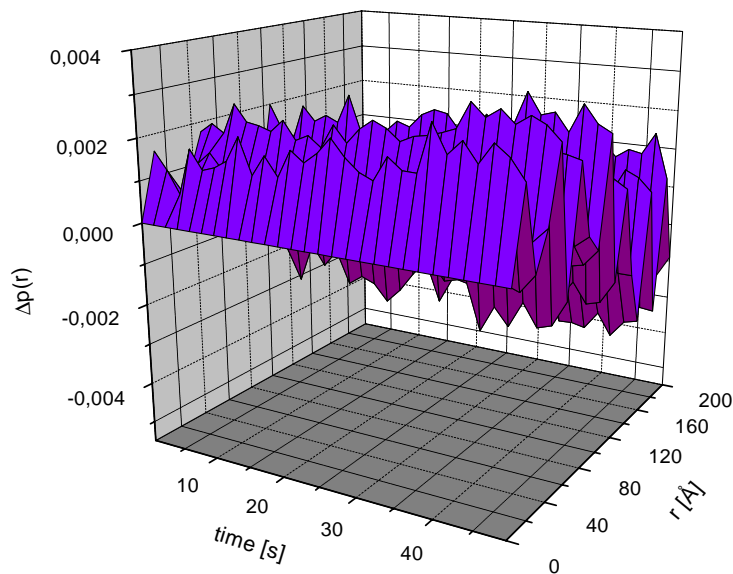


Fig. 6.33: Difference $p(r)$ function of the GroEL-GroES complex mixed with a low ATP concentration.

In the $\Delta p(r)$ function there are modulations in time at various distances r visible. Like for the decay of distance at the GroEL ATP cycle without GroES is the significance of one single time point not very high, but in the time progression the data show an interesting behavior of the GroEL-GroES-ADP₇ complex.

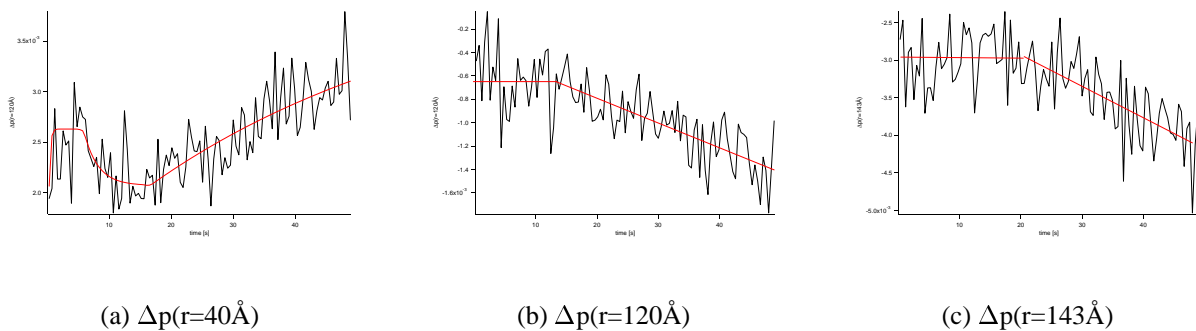


Fig. 6.34: Selected distances of the $\Delta p(r)$ function for the GroEL/GroES ATP cycle (single turnover experiment).

Binding of GroES to GroEL in the presence of a multiple turnover ATP concentration

The binding behaviour of the GroES to the GroEL was also investigated in the presence of a 10-fold ATP multiple turnover concentration. For this the GroEL and GroES were mixed together with a ATP solution ($c_{ATP} = 1mM$). Thus, the final ATP concentration was 0.5mM, as in the experiments of multiple ATP concentrations mentioned before. The data are represented in the next fig. 6.35, analyzed out of four independent data sets.

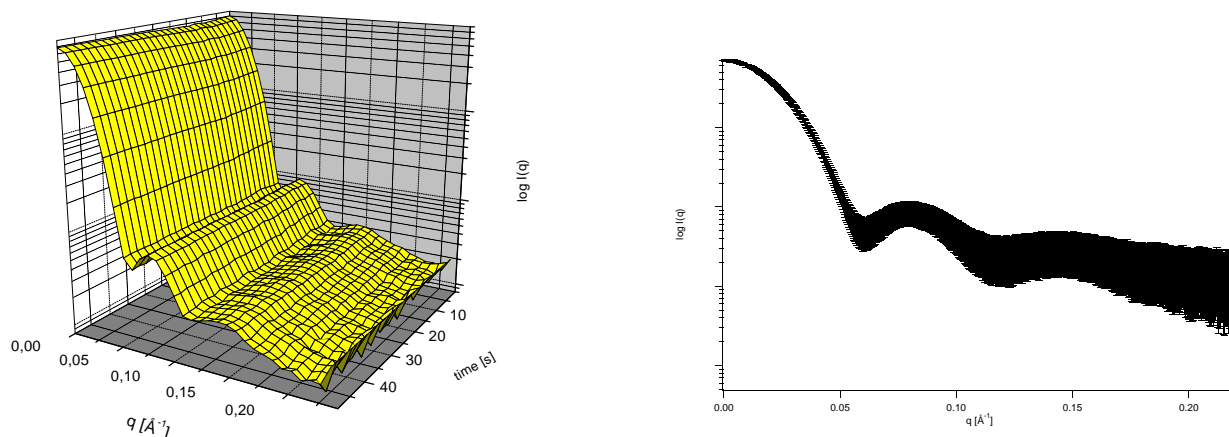


Fig. 6.35: $I(q)$ and $p(r)$ functions of GroEL mixed with GroES in the presence of high ATP

From the $I(q)$ function the radius of gyration and the $p(r)$ function were calculated for every time-point, as usual for the other experiments (fig. 6.36).

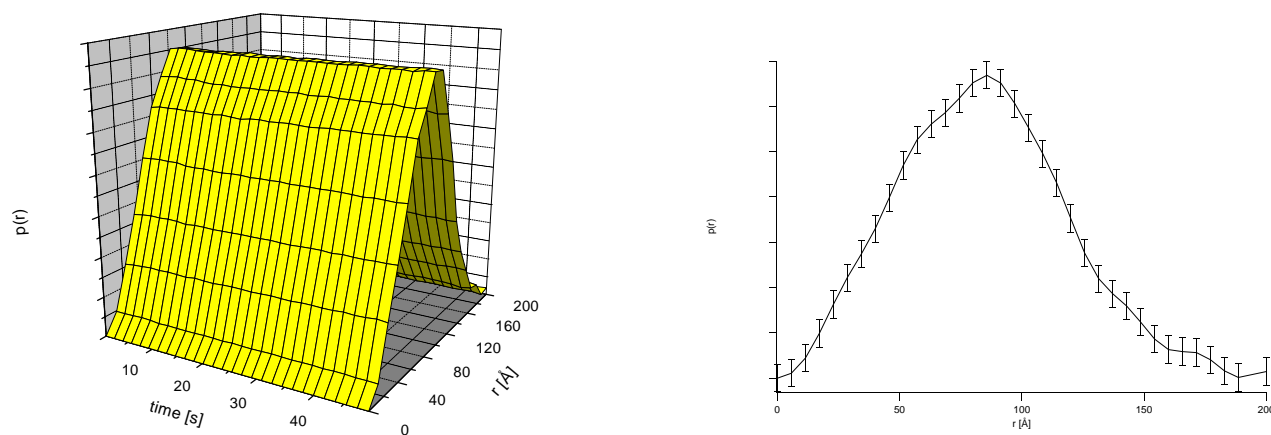


Fig. 6.36: $p(r)$ functions of GroEL mixed with GroES in the presence of high ATP

The $p(r)$ functions show the characteristic shape of the GroEL-GroES complex. The remarkable shoulder at $\approx 60 \text{\AA}$, and the increase at higher distances is due to the GroES binding.

The analysis of the R_g -values is shown in figure 6.37. The time progression of the radius of gyration shows a more or less stable value at $R_g \approx 66.5 \text{\AA}$ over the whole time range of the experiment. This value is between the proposed GroEL-GroES-ADP₇ ($R_g \approx 66.2 \text{\AA}$) and the GroEL-GroES-ATP₇ ($R_g \approx 66.8 \text{\AA}$)

states. The reason therefore is first the non synchronicity of the ATP binding and hydrolysis and second

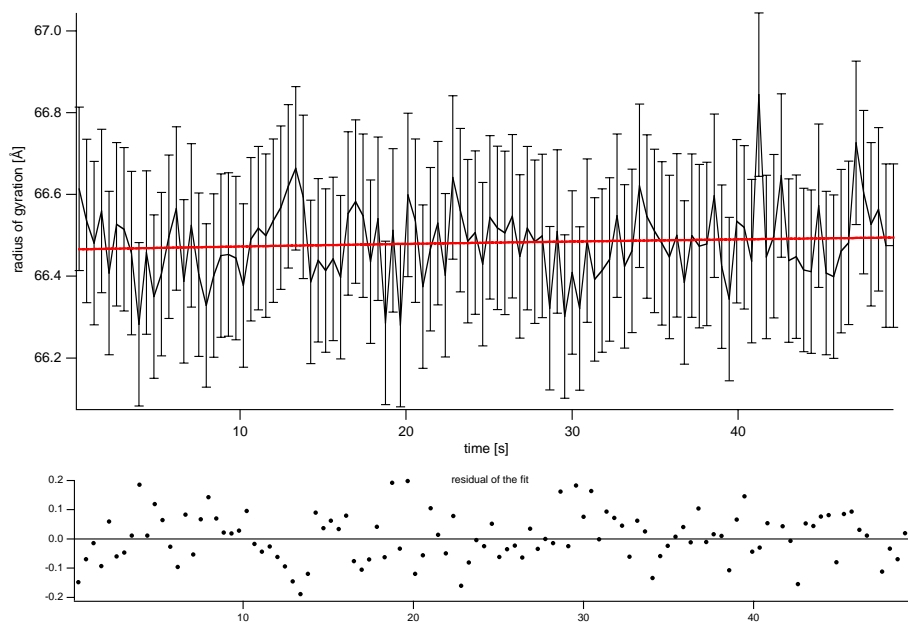


Fig. 6.37: Time progression of the radius of gyration for the formation of the GroEL-GroES asymmetric complex in the presence of high ATP.

the limitation in the time resolution of 150ms of the CCD-detector system (see chapter "Detectors"). This two problems result in a consequent averaging over the whole ensemble of the protein molecules in the state of the ATP binding and hydrolysis.

From the $p(r)$ function a difference $\Delta p(r)$ function was calculated using the asymmetric GroEL-GroES-ADP₇ complex as reference. The plot of this $\Delta p(r)$ is shown in the next figure (fig. 6.43)

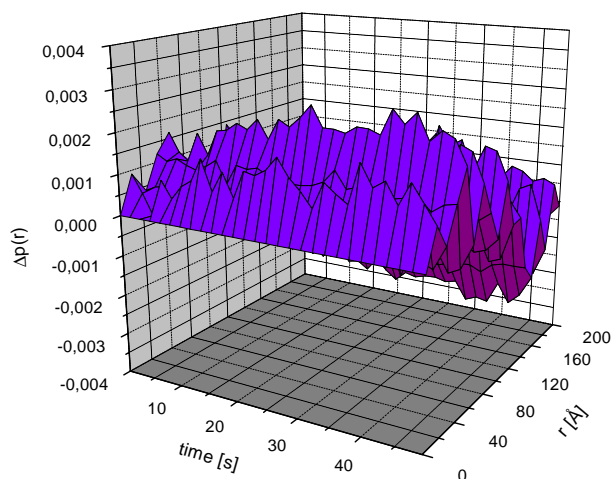


Fig. 6.38: Difference $p(r)$ function of the asymmetric GroEL-GroES complex mixed with ATP ($c_{ATP} = 0.5mM$).

6.2.2 Dynamics of the asymmetric GroEL-GroES complex in the presence of ATP

While the binding of the GroES to the GroEL was traced in the chapters above, also the behaviour of this asymmetric GroEL-GroES complex in the presence of ATP was investigated. For this the preformed complex (GroEL-GroES-ADP₇) was mixed together with ATP using the stopped-flow apparatus as discribed. In analogy with the previous experiments the following data sets were obtained.

1. The asymmetric complex under a single turnover ATP concentration ($c_{ATP} = 0.05mM$)
2. The asymmetric complex under multiple turnover ATP concentration ($c_{ATP} = 0.5mM$)

The asymmetric complex under single turnover ATP concentration

According the experiments with low ATP the preformed GroEL-GroES-ADP₇ complex was mixed with a solution of 0.1mM ATP, resulting a final ATP concentration of 0.05mM after mixing. The experiments were repeated four times and the obtained data sets were averaged after the radial integration, as described. From the scattering intensity function $I(q)$ the radius of gyration and the $p(r)$ were calculated. The resulted $I(q)$ and $p(r)$ functions are shown in figure 6.44 to 6.47. Also this data shows a good statistic quality.

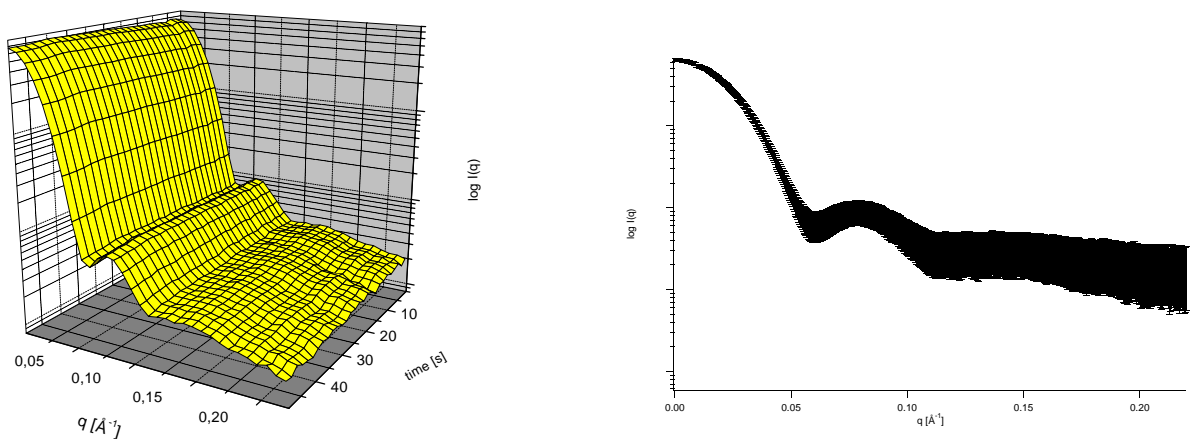


Fig. 6.39: $I(q)$ function for the asymmetric complex in the presence of a single turnover ATP concentration, with estimated errors (right)

Out of the scattering data the radius of gyration was calculated via the Guinier approximation. The time progression of the R_g is shown in the next figure.

In the time progression of the R_g -value shows first an increase to $\approx 66.6\text{\AA}$ indicating the formation of the GroEL-GroES-ATP₇ complex. This complex decays within the 20s to the GroEL-GroES-ADP₇, whereby the dissociation of the GroES from the GroEL does not occur within this time scale and is therefore not visible. In difference to the binding experiment of GroES to GroEL under the same, low ATP conditions, the R_g -value do not go up within the 50s experimental time window.

The difference $\Delta p(r)$ function was derived by subtracting the asymmetric GroEL-GroES-ADP₇ complex from the $p(r)$ function shown in fig 6.49.

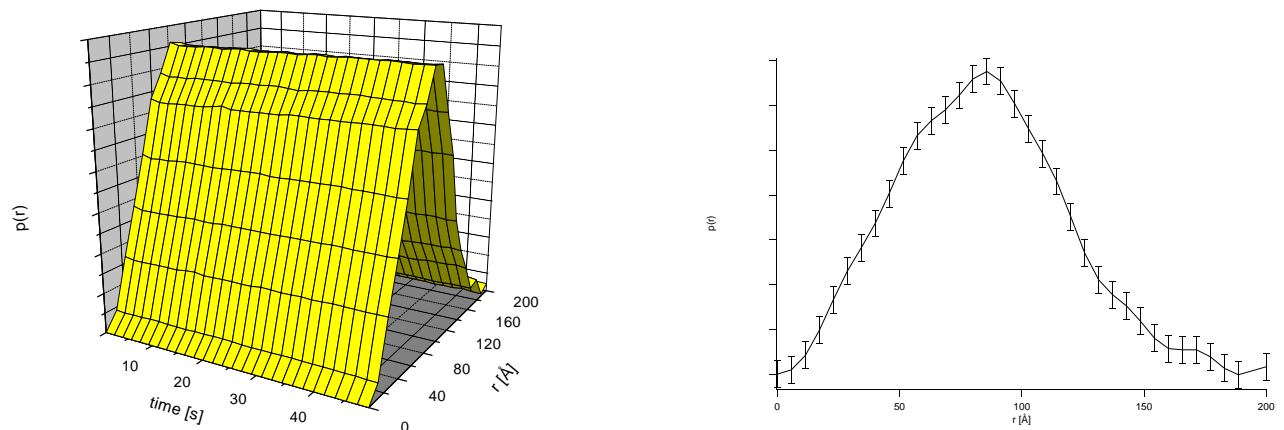


Fig. 6.40: $p(r)$ functions of the asymmetric GroEL-GroES complex of a single turnover ATP concentration, with estimated errors (right)

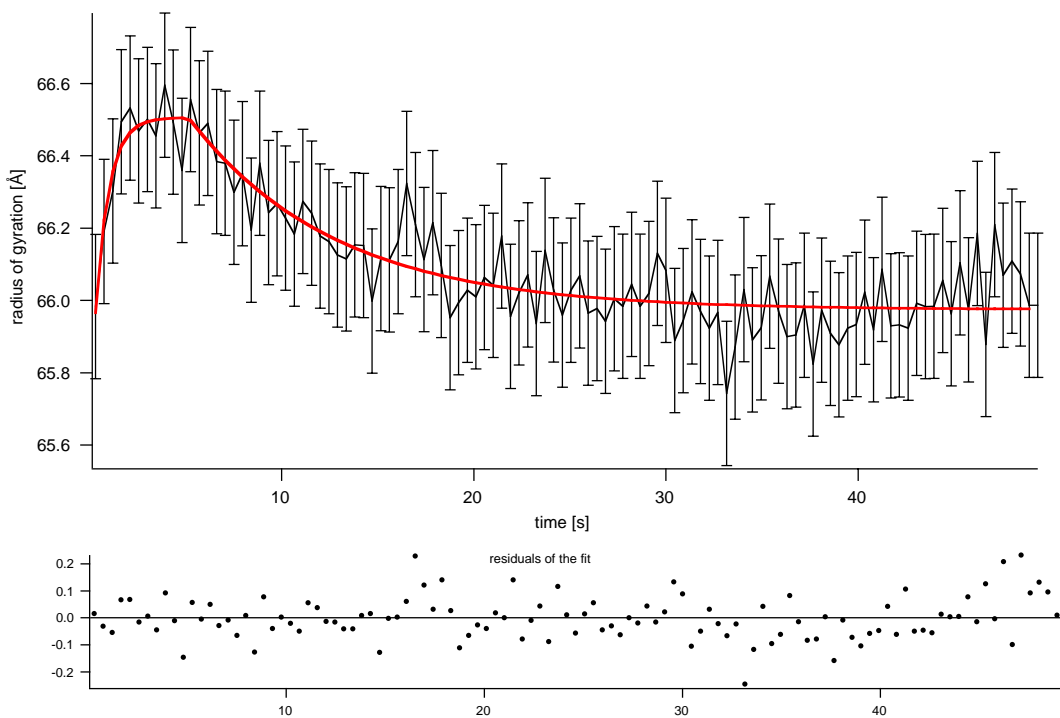


Fig. 6.41: Time progression of the radius of gyration of the asymmetric GroEL-GroES complex in the presence of low ATP.

Additional the distances of the $\Delta p(r)$ for the experiment at low ATP concentrations for $r=40$ Å, $r=120$ Å and $r=143$ Å were analyzed. In figure 7.14 the time progression of the three distances are shown.

The selected distances show a different behavior as for the formation of the complex. Only the $\Delta p(r)$ for $r=40$ Å shows a bi-phasic progression, while the other distances stay stable in time. The amplitudes of the deviations are in the same range like the starting amplitudes in the mixing experiment before, but no further deviation can be observed. This finding indicates that the formation of the activated GroEL-

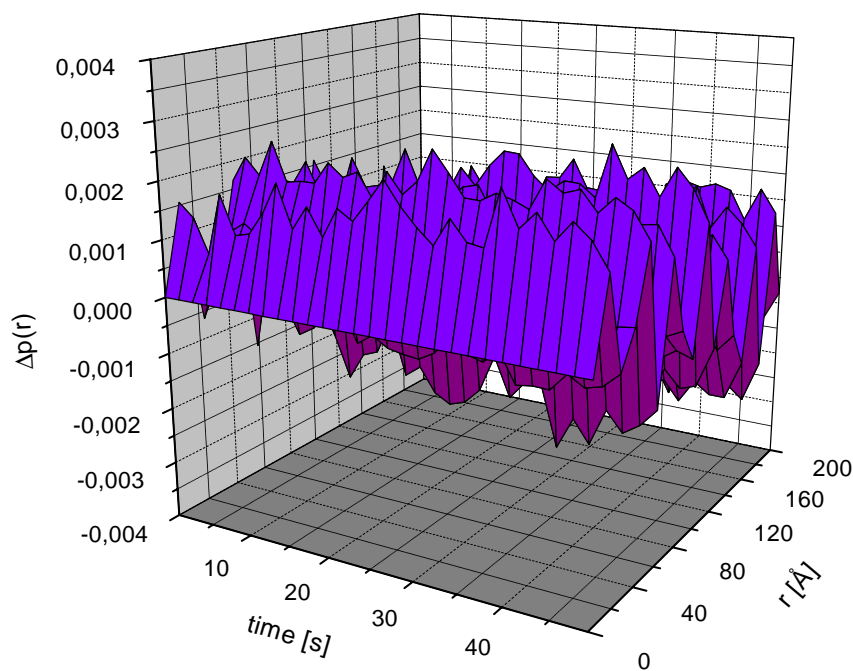


Fig. 6.42: Difference $p(r)$ function of the GroEL-GroES complex mixed with a low ATP concentration.

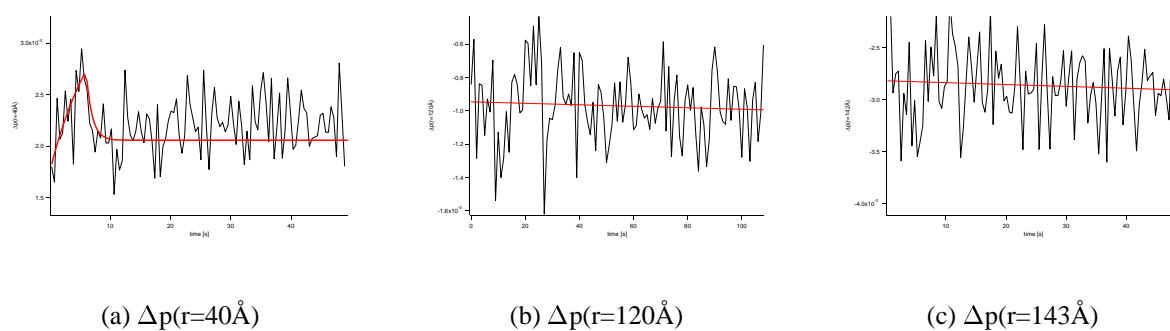


Fig. 6.43: Modulation of selected distances of the $\Delta p(r)$ function for the reaction of the GroEL-GroES-ADP₇ complex in the presence of low ATP.

GroES-(ADP)₇ complex is inhibited by ADP. It is remarkable, that the progression of the distance at 40Å reflects in the presence of GroES the progression of the Rg-values.

The asymmetric complex under multiple turnover ATP concentration

In analogy with the experiments above the asymmetric GroEL-GroES-ADP₇ complex was mixed with a solution containing a concentration of 1mM ATP (final concentration $c_{ATP} = 0.5mM$) using the setup described above. From four independent data sets the $I(q)$ as well as the $p(r)$ were calculated and analysed after the averaging. The resulting data for the scattering intensity and the distance distribution function is shown in figure 6.44.

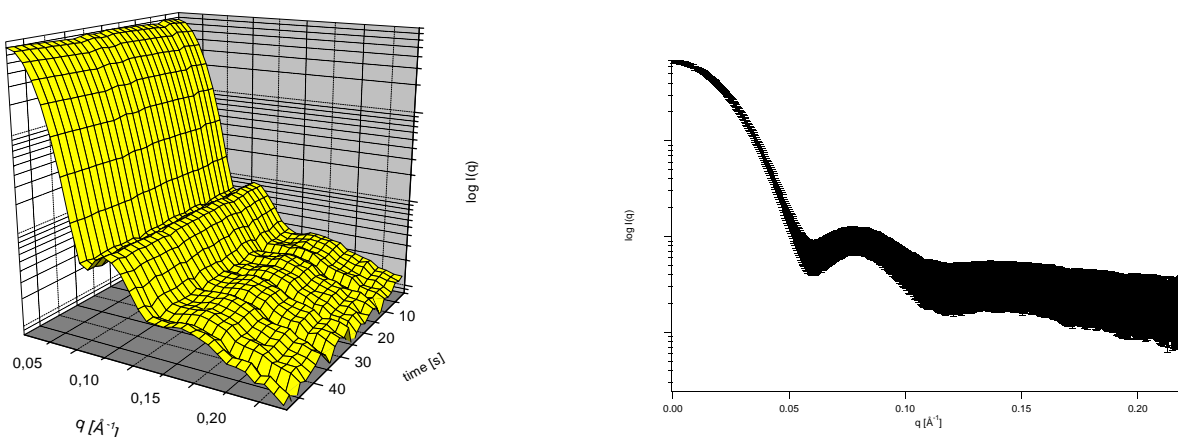


Fig. 6.44: The asymmetric GroEL-GroES complex in the presence of high ATP

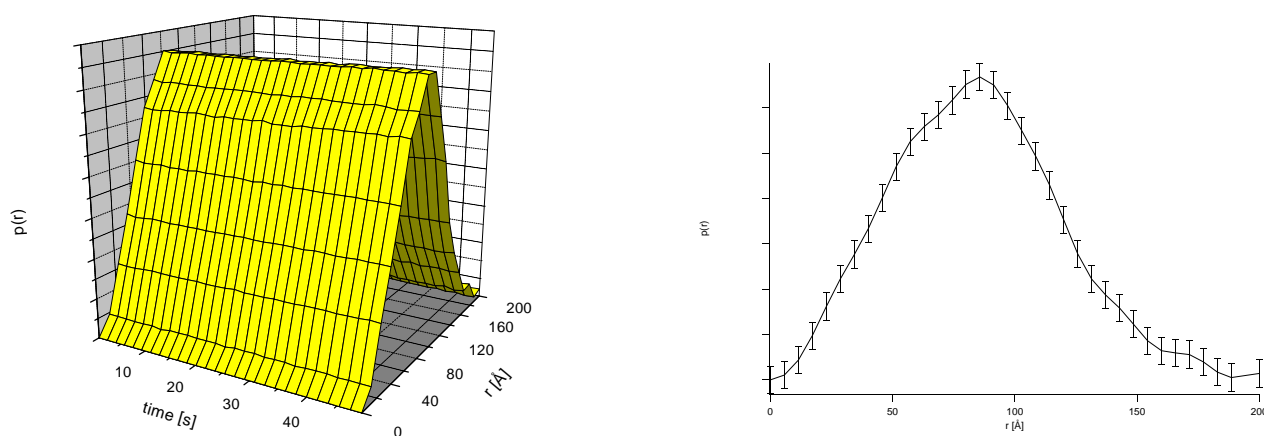


Fig. 6.45: The asymmetric GroEL-GroES complex in the presence of high ATP

The data is further analyzed by calculating the R_g for every single time point. This time progression of the radius of gyration is shown in the figure 6.45.

Like the time progression of the R_g -values for the binding of the GroES to the GroEL under 10-fold multiple turnover ATP concentration, the R_g -value starts up at 66.6\AA , but do not remains stable over the experimental duration of 50s. The slight decrease within the 50s from 66.6\AA to 66.4\AA indicates a different ATP hydrolysis behavior for the two intermediate states.

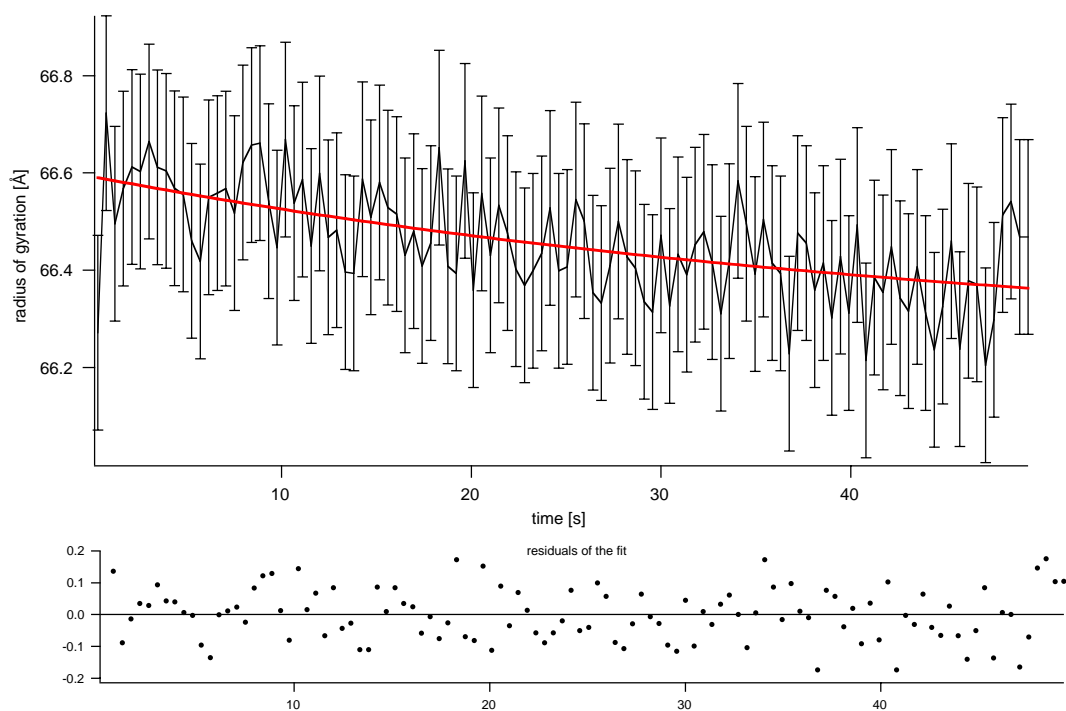


Fig. 6.46: Time progression of the radius of gyration and the molecular weight for the conformation of the GroEL-GroES asymmetric complex in the presence of high ATP.

This differences can also be observed at the $\Delta p(r)$ calculated using the stable, asymmetric complex as reference.

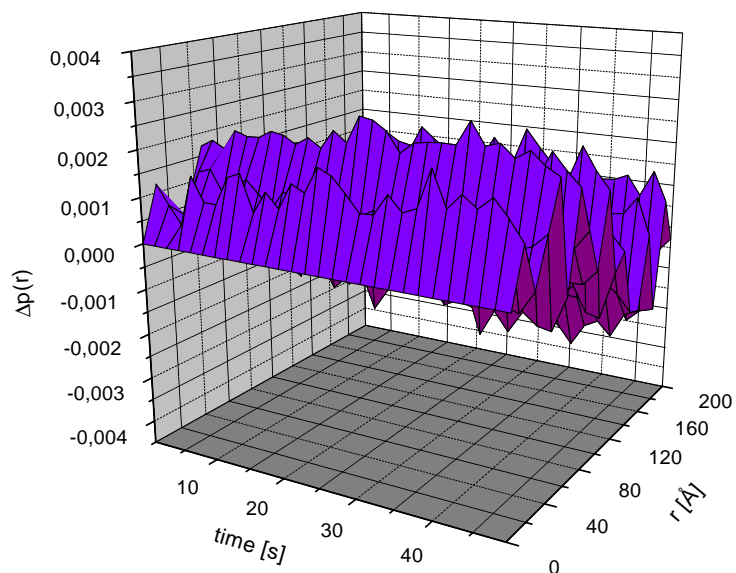


Fig. 6.47: Difference $p(r)$ function of the GroEL-GroES complex mixed with a high ATP concentration.

6.3 Time-Resolved Small Angle Neutron Scattering - First Results

In general the time-resolved small angle scattering technique is not restricted to X-rays, but the limiting step is the flux of scattered particles. While third generation synchrotron sources provide a flux of $5 \times 10^{12} ph/s$, the SANS instrument D22 at the Institut Laue-Langevin in Grenoble provides a neutron flux of $3 \times 10^7 s^{-1} cm^{-2}$ ($\lambda=8\text{\AA}$; collimation 4m). Another difference between TR-SAXS and TR-SANS is the sizes of the neutron and X-ray beam. The beamsizes at ESRF's SAXS beamline is $0.6 \times 0.2 mm^2$ while the beamsizes of the D22 is $20 \times 9 mm^2$. For the optimal use of these beam parameters a flat cell has to be used, and the experiment has to be repeated several times. In order to minimize the consumption of protein the exposure times are restricted to 1s, and an averaging over ten independent experiments leads to sufficient statistics of the scattering data.

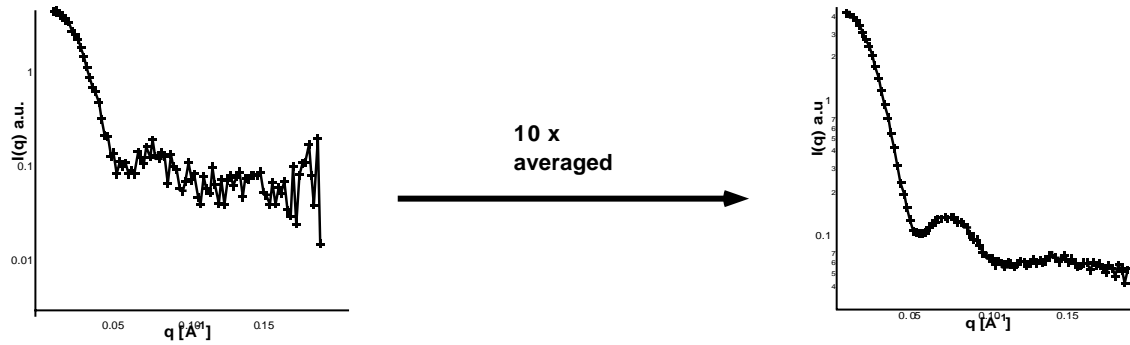


Fig. 6.48: Neutron Scattering intensities of a single experiment and the averaging over 10 independent experiments

The advantages of neutrons are firstly that neutrons do not damage the protein, and secondly the use of the contrast variation method. This powerful method takes advantages of the different scattering behavior of the hydrogen- and deuterium nucleus for neutrons. If the hydrogens of a protein are exchanged with deuterium atoms by growing bacteria in D_2O media, D-labeled proteins with a different scattering behavior, compared to the normal unlabeled H-protein, can be obtained [75, 56]. In figure 4.49 the different contrast $\Delta\rho (= \rho_{solution} - \rho_{protein})$ of H-proteins and D-proteins is shown.

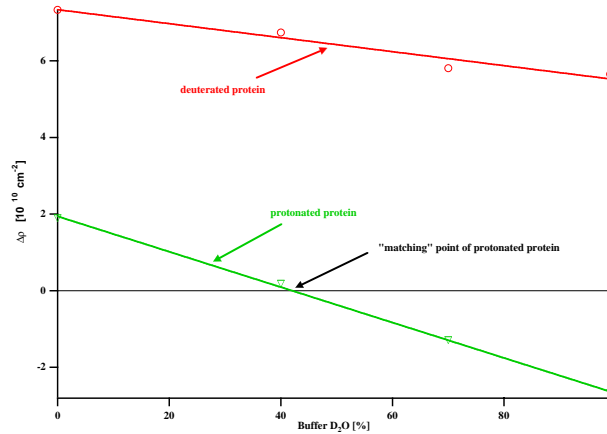


Fig. 6.49: Contrast $\Delta\rho$ of protonated protein and deuterated protein in different D_2O buffer solution. At 99% D_2O the contrast of the protonated protein is still positive while the deuterated protein has a negative contribution.

This large difference in the scattering behavior is mainly used for neutron scattering under contrast matching conditions where the scattering contribution of the protonated protein is equal to zero, while the deuterated protein is still visible. In TR-SANS the difference in the scattering behavior can be used to enhance the signal for the protein-protein interaction by performing scattering experiments of H-protein and D-protein in 99% D₂O buffer. In this experiment the protonated protein has a strong negative scattering contrast while the deuterated protein has a positive contribution. In the case of the H-GroES-D-GroEL complex the radius of gyration of this assembly is decreased with respect to the homogenous GroEL-GroES complex. The decrease of the R_g-values in time can be used to following the binding reaction of the two proteins. In figure 4.50 the radius of gyration for the binding of H-GroES to D-GroEL in the presence of a high concentration (5mM) of the non hydrolysable ATP analog AMP-PNP ($c_{AMP-PNP}$) is shown. In the presence of this nucleotide substitute the symmetric GroES-GroEL-GroES complex is formed.

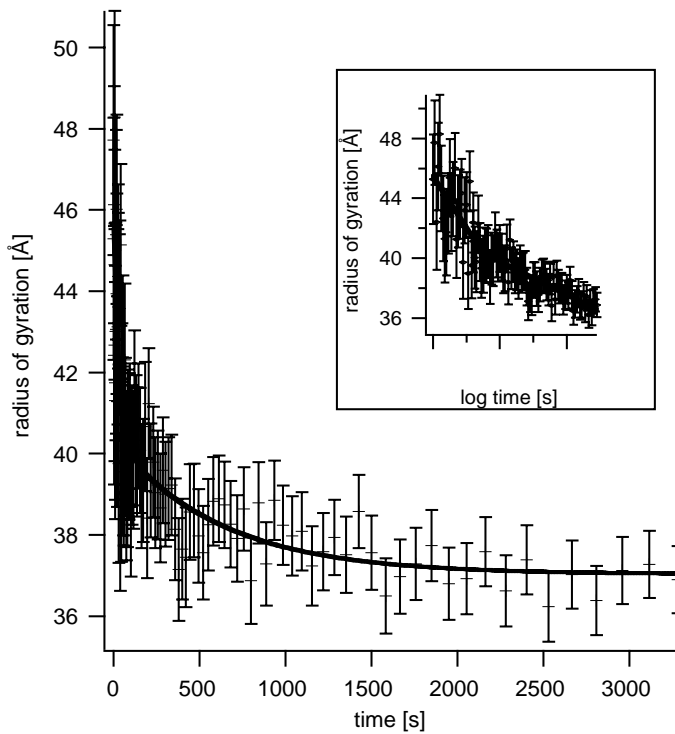


Fig. 6.50: Time progression of the radius of gyration for the formation of the symmetric GroEL-(GroES)₂ complex.

The time progression can be fitted to a double exponential function, indicating the binding of the second GroES molecule to the GroEL.

These first results on the chaperonin system GroE indicate the power of TR-SANS for the investigation of protein-protein interactions. Starting from these results, further investigation using, TR-SANS, are being made by Dipl. Biol. Jörg Holzinger at the ILL. The special interests at this project are the binding of substrate-protein to the chaperonin using neutrons and differently labelled proteins.

7. DISCUSSION

7.1 *Time Resolved Small Angle Scattering - A Proper Method for Protein Kinetics and Dynamics?*

The investigation of static protein structures with atomic resolution led to detailed insights of the structure and function of proteins[76, 77]. Complimentary and more detailed information about the function of the protein can be obtained by tracing structural changes upon the reaction cycle in time. The different time-resolved methods for the investigation of structural changes show several limitations on the time-scale, the size of the protein and the triggering of the reaction of interest[11, 12]. For instance, association and dissociation reactions as well as large conformational rearrangements are in a crystal often sterically blocked and not accessible by protein X-ray crystallography.

Time-resolved small angle scattering is a method for the investigation of kinetics and structural relaxation dynamics of large protein assemblies, whereas the time resolution is limited to the subsecond range. Shape changes of the proteins due to association and dissociation processes as well as large conformational changes within the proteins can be analysed and transiently formed protein conformations identified. Since small angle scattering is a solution scattering method, the triggering of these reactions can be achieved very simply by mixing of reactants. The random orientation of the proteins in solution leads to a loss of information and no 3-dimensional structure with atomic resolution can be calculated from the scattering data. This loss of information can be partly compensated if high resolution structures for the starting and the final conformation upon the reaction are available. Thus, time-resolved small angle scattering of proteins in solution closes the gap between the investigation of small conformational changes on the ps time scale and large changes which occur in the subsecond range. Structural differences often result in very small deviations of the small angle scattering data. In static experiments the significance of these small deviations is very low. In time-resolved small angle scattering the trend of these deviations can be traced and enhances the significance.

The sensitivity of small angle scattering using X-rays and neutrons is limited by two factors. Firstly, by the number of scattered particles such as X-ray photons or cold neutrons and secondly by the readout time of the capable detectors. The use of small angle X-ray and neutron scattering for the investigation of protein kinetics, the advantages and disadvantages as well as results on chaperonin system GroEL/GroES are discussed in the next chapters.

7.1.1 *Short Times, Low Contrast and a Lot of Photons: Time Resolved Small Angle X-ray Scattering*

The development of synchrotrons enhanced the possibilities in structure research in several ways. Due to the high flux of X-ray photons produced by synchrotron radiation, methods such as small angle scattering were now capable for time resolved analysis. A typical beamline at a third generation synchrotron source, such as the ESRF in Grenoble or the ELETTRA in Trieste, produce a flux of $10^{12} - 10^{13}$ photons per second (@12keV $\hat{=}$ 1Å wavelength). Due to this high flux two problems arise. Firstly, the radiation

damage of the protein due to huge amount of high energetic photons, and secondly the detector has to be able to detect a high flux of scattered photons.

The radiation damage problem could be overcome by the development of a so called "continuous" stopped-flow device. While in a conventional stopped-flow device two syringes, containing the two reactants, facilitates the mixing, the advanced "continuous" stopped-flow consists of three syringes. This additional, third syringe produces a slow flow of already mixed sample through the irradiated capillary in order to push non damaged sample in the X-ray beam.

For the detection of the flux a CCD detector was found to be the best choice. This detector represents a compromise between a high counting rate and a fast readout. Whereas the CCD detector FRELON at the ESRF can be readout within 150ms, but shows no deadtime effects such as a standard gas-filled delay line detector.

The synchrotron radiation at a third generation source can be produced by insertion devices such as wigglers and undulators. The radiation produced by these two insertion devices differs mainly in the beamsize, and consequently in the irradiated sample volume. For instance the irradiated volume for a typical undulator beam is 0.12mm^3 ($0.6\text{mm} \times 0.2\text{mm}$ beamsize, capillary with 1mm diameter). Using this standard setup for small angle scattering, a number of irradiated molecules of $\approx 7 \times 10^{10}$ can be estimated in the case of the small undulator beam. A wiggler beam of typical beamsize of $5\text{mm} \times 2\text{mm}$ increases the number of molecules to $\approx 5 \times 10^{12}$. This enhances the number of scattered photons and shorter exposure times can be achieved. In any case the detection of the scattered photons is the rate limiting step of small angle scattering. Recently several projects for enhanced X-ray detectors, which are able to handle the high flux of photons combined with a short readout are initiated (status autumn 2000).

7.1.2 Short Times, High Contrast and Dripping Neutrons: Time Resolved Small Angle Neutron Scattering

In contrast with X-ray photons of 12keV ($\approx 1\text{\AA}$), cold neutrons ($\lambda=8\text{\AA}$) are used for the structural studies. Since the kinetic energy in these cold neutrons is in the meV range, neutrons do not damage the proteins. The recently available neutron sources produce a much lower flux of neutrons, compared to a third generation synchrotron source. For instance, the small angle scattering beamline D22 at the Institute Laue-Langevin (ILL) in Grenoble provides a flux of 3×10^7 neutrons per second ($@8\text{\AA}$ wavelength and 4m collimation), which is four orders of magnitude lower compared to SAXS beamlines at the ESRF or the ELETTRA. This lower flux can be partly compensated by:

1. The large beamsize of the neutron beam $20 \times 9\text{ mm}^2$
2. Enhancing the contrast of the protein in a D_2O environment
3. Using selectively D-labeled protein

As calculated for the X-ray scattering, increases the beamsize of $20 \times 9\text{mm}^2$ the number of scattering particles to 1×10^{14} . The use of D-labeled proteins in buffer containing 99% D_2O increases the scattering contrast by a factor of 3, and the amount of scattered neutrons can be further enhanced.

The large beamsize requires a larger cuvette, which results in an enlarged mixing volume. The larger mixing volume causes two problems. Firstly the need of more protein, which is special in the case of D-labeled protein not easy to obtain, and secondly in an extended mixing time. However, under the conditions described above, scattering data with sufficient statistics can be obtained within 1s. The statistics can be enhanced by repeating and averaging over several independent experiments.

Despite this disadvantages, small angle neutron scattering provides additional detailed information about proteins in solution by the method of contrast variation. This method is based on the different scattering crosssections of protons and deuterons, and can not be applied to X-rays. From this data, complementary to X-ray scattering experiments, can be obtained.

7.2 The ATP-ase Activity of GroEL

The GroEL chaperonin shows a various interplay between cooperative and anticooperative ligand binding. The nucleotide binding breaks the symmetry of the otherwise non distinguishable GroEL heptameric rings. The switching between symmetric and antisymmetric stages seems to play an important role in the function of the chaperonins during their refolding cycle. The different states are defined as a T(ense)-state where the nucleotide can bind, and the R(elaxed)-state where no nucleotide can bind or is bound. The kinetic constants of the ATP-ase cycle of the GroEL were investigated by several biochemical and biophysical methods. These kinetic constants were verified by small angle scattering and further information about cooperative and anti-cooperative nucleotide binding and the resulting structural changes was obtained.

7.2.1 Allosteric Effect of the Cooperative ATP Binding

If proteins are build of several identical subunits the cooperative binding of ligands is often facilitated by an allosteric enhanced binding behavior. An allosteric effect of the nucleotide binding is also proposed for the GroEL subunits. For this the binding of one single ATP molecule to a GroEL subunit should switch the whole GroEL heptameric ring into a state with an enhanced affinity for ATP. The other ATP molecules can bind to the remaining six allosterically switched GroEL subunits, while the opposite GroEL heptameric ring is blocked for ATP binding. The allosterically switched GroEL as well as the ATP hydrolysis and the relaxation to a the ADP bound ground state were investigated by small angle scattering. The formation of a transient GroEL state upon ATP binding and hydrolysis can be identified

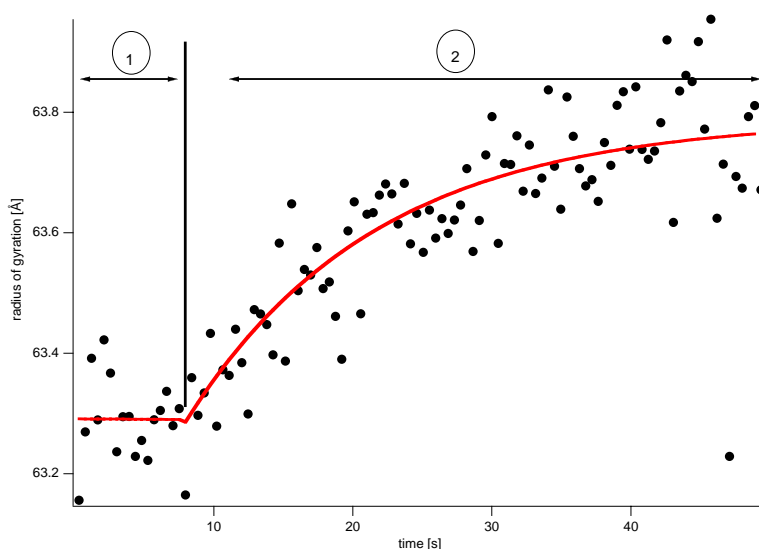


Fig. 7.1: The bi-phasic time trend of the radius of gyration indicates intermediate states of the GroEL upon ATP binding in the radius of gyration (phase 1 in fig. 7.1). The Rg-value is decreased from 63.7Å, the initial

R_g-value of the GroEL, to 63.3 Å. The formation of the nucleotide bound GroEL shows no binding kinetics within the first 150ms. These data support the model of the allosteric effect for the ATP binding. The binding of a single ATP molecule shifts the whole GroEL molecule into the allosterically switched state, and the overall shape changes of the GroEL appear immediately. Another remarkable feature is the stable period of the binding and hydrolysis phase. In the case of a single turnover ATP concentration this period is about 8s, and is prolonged for the 10-fold multiple turnover to 30s. This stable phase indicates, that ATP hydrolysing GroEL ring remains in the allosterically switched state until the hydrolysis is finished. The relaxation of this GroEL ring to the ADP-bound ground state occurs afterwards.

Besides the radius of gyration, a very sensitive parameter for shape changes, the allosteric switch can be investigated by the $\Delta p(r)$. Model calculations had shown that the binding of nucleotides results in changes of distances at 120 Å. Hence, the $\Delta p(r)$ at 120 Å provide direct insights to the nucleotide binding pockets upon ATP binding. Since there is no kinetics for the ATP binding visible, the GroEL seems to be switched into the enhanced ATP binding state directly after ATP binding. Remarkable is the bi-phasic decay in the $\Delta p(r)$. This first phase of the decay correlates with the first phase seen in the R_g-values. Taking into account the biochemical result, that the ATP hydrolysis starts immediately after the ATP binding, this first phase can be denoted to the ATP hydrolysis. The overall GroEL shape does not change upon hydrolysis, indicated by the stable R_g-values within this phase. Thus, the GroEL subunit remains after the hydrolysis in an "activated T-state", which is similar to the ATP state. An another interesting feature can be remarked in the $\Delta p(r)$ during the hydrolysis phase. If the hydrolysis appears in a concerted manner, the data would stay stable and the relaxation starts afterwards. The linear decay of the distances within the first 8s indicates that this is not the case and the hydrolysis occurs in a non concerted way. The second phase is the relaxation of the activated GroEL_{ADP}^{*} state, back to the GroEL_{ADP} ground state. If in the activated ADP state the cleaved γ -phosphate is still located in the nucleotide binding site, can not be decided from this data.

As mentioned above, the ATP hydrolysis does not cause the shape change of the GroEL, but the allosteric switch after the binding of a single ATP molecule to a GroEL subunit. From the R_g-values of the single turnover ATP experiment, the hydrolysis time of 8s for one GroEL ring can be derived. Therefore a prolonged stable phase of 80s seconds can be estimated for the 10-fold turnover. However, the stable phase is only 30s. Consequently the second GroEL ring have to be taken into account. During the ATP binding this ring remains empty in the R-state and is blocked by the anti-cooperativity between the two rings. After the binding of seven ATP and their instant hydrolysis in the T-state ring, the GroEL subunits of the R-state ring starts to bind ATP, and the GroEL is shifted into the "activated T-state". From the data can be concluded, that for the ATP hydrolysis the second GroEL ring has to remain free, but in the case of the multiple turnover the dissociation of the ADP from the GroEL nucleotide binding pockets seems to be more and more inhibited by the increasing amount of produced ADP. The relaxation from the activated GroEL state to GroEL ground state is slowed down by this product inhibition and can be remarked in the R_g-values as well as in the $\Delta p(r)$.

From this two different sets of data the following model for the hydrolysis cycle of the GroEL can be derived:

1. The GroEL binds an ATP rapidly followed by an allosteric switch of the GroEL ring where the ATP is bound
2. The conformational change of the GroEL is caused by nucleotide binding and not by the hydrolysis

2. The ATP hydrolysis starts immediately after the binding in a non concerted mode
3. The ATP hydrolysis is a highly cooperative reaction where all seven subunits have to finished their hydrolysis reaction before the next cycle or the relaxation starts
4. The binding of ATP to the opposite GroEL ring switches the GroEL in the enhanced ATP binding state and inhibits the relaxation to the GroEL_{ADP} ground state

7.2.2 Comparison of the Small Angle Scattering Data for the GroEL-ATP Complex with Structures from X-ray Crystallography and Electron Microscopy

The ATP bound state of the GroEL is not a static structure, since the ATP-ase cycle starts directly after the nucleotide binding. Therefore, static methods have to use kinetically stalled intermediated using non hydrolysable ATP analogues which acts as substitutes for the ATP.

For the GroEL in complex with such a the slow hydrolysable ATP analogue $\text{ATP}\gamma\text{S}$, a crystal structure is available (see fig. 7.1 left)[78]. This structure was used for a comparison between the ATP bound state and the non ligated GroEL. As pointed out above, the changes at the nucleotide binding pockets of the GroEL upon ATP binding and hydrolysis are visible in the $\Delta p(r)$ at $r=120\text{\AA}$. Indeed the $\text{GroEL}-(\text{ATP}\gamma\text{S})$ structure shows conformational changes mainly at the nucleotide binding sites, indicated by the maximum at $\approx 120\text{\AA}$ in the $\Delta p(r)$ function (see fig. 7.1 right: blue line).

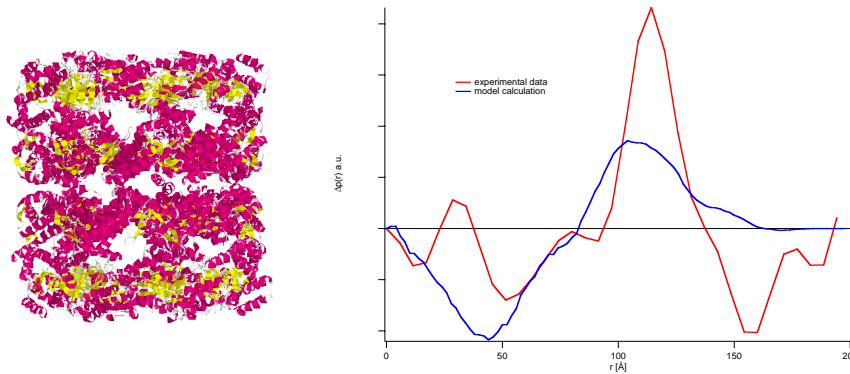


Fig. 7.2: left: The $\text{GroEL}-(\text{ATP}\gamma\text{S})_7$ structure from X-ray crystallography. right: The difference $p(r)$ derived from model-calculation of GroEL non ligated and in complex with $\text{ATP}\gamma\text{S}$ (blue) and experimental data (red).

However, the difference $\Delta p(r)$ between the two structures shows differences in the range of 90\AA to 120\AA as expected, but also large changes at $\approx 50\text{\AA}$. These differences are also found in the experimentally derived $\Delta p(r)$, but not that pronounced (fig. 7.1 right: red line). The high peak at 120\AA indicates larger changes at this distances. Since no conformational changes of the apical and intermediate domains of the $\text{GroEL}_{\text{ATP}\gamma\text{S}}$ upon nucleotide binding are described for the crystal structure[78], the changes in the range of 50\AA could also be induced by nucleotide binding. Hence, the amplitude of the differences at 50\AA are consequently in the same range like the amplitude of the changes at 120\AA ¹. In the small angle scattering data no significant changes at 50\AA are visible. If they do not occur or if they have not significant amplitudes can not be decided from the experimental data. However, high resolution electron microscopic data report for the GroEL-ATP complex not only changes in the equatorial domain. These data shows large conformational changes of the GroEL-ATP_7 complex compared to the

¹ The integrated area of the $\Delta p(r)$ has to be zero, because the molecular weight of the molecules does not change.

un-ligated structure. In figure 7.2 a comparison between EM-images of the GroEL-ATP state and the GroEL-ADP state is shown.

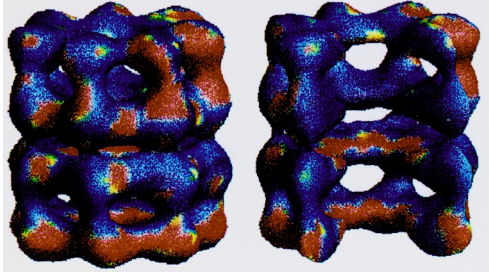


Fig. 7.3: Comparison of high resolution electron microscopy of the GroEL-ATP and the GroEL-ADP state. The differences are encoded in red (significant change) and blue (no difference). The apical domains of both rings shows significant changes as well as the nucleotide binding sides located in the equatorial domain. (Roseman M.A., et al. Cell 97(3):325-38, 1999 Apr 30)

Remarkable in the EM-structures is, that the binding of nucleotide to one ring causes changes in the apical domains of the opposite ring. This behavior would lead to changes in the small angle scattering data at larger distances than 150\AA . On the other hand changes at the apical domains in one ring would indeed result in changes in the range of 120\AA . According to these changes the distances at $\approx 120\text{\AA}$ would increase and result in a high peak at this point, whereas the distance at 50\AA would not be involved. This might be the explanation for the high peak at 120\AA in the small angle scattering data.

7.3 The GroEL-GroES nucleotide cycle

The GroEL-GroES nucleotide cycle is dominated by the binding of the co-chaperonin GroES, even in a structural analysis. Thus, besides the kinetic constants for the formation of the complexes structural data were calculated out of the time resolved data.

7.3.1 Asymmetric binding of the GroES in the presence of ADP

The GroEL-GroES asymmetric complex is stably formed in the presence of ADP. The formation shows an association constant of $k_{Ass} = 4 \times 10^5 M^{-1} s^{-1}$. This finding is in line with biochemical data derived by other methods[79]. The experimentally derived radius of gyration of 66.1\AA after 10s corresponds with experimental data from static small angle X-ray and neutron scattering. For the asymmetric GroEL_{ADP}-GroES complex two possible structures are reported. Firstly a model derived from small angle neutron scattering[56] and a secondly the crystal structure[60]. The model of the neutron scattering was obtained using selectively labeled proteins under contrast matching conditions (see chapter 6.3). This approach allows to investigate selectively the GroES while it is bound to the GroEL.

From these experiments differences between the bound GroES in the solution structure and the crystal structure were found. While the GroES in the crystal structure shows only small changes at the "mobile loops" which facilitate the binding to the GroEL, the GroES in solution undergoes large conformational changes. The dome shaped GroES heptameric molecule opens its structure and enlarges the hydrophobic surface for the binding to the GroEL. On the other hand shows the GroEL an overall conformational change which is not visible in the small angle neutron scattering. The contrast variation technique can not be adapted for X-ray scattering. Thus, small angle X-ray scattering can not distinguish if changes occur in the GroES or in the GroEL, because only the superpositions of all changes are visible. The rather small conformational changes of the GroES are overridden by the huge overall changes upon the binding reaction.

If the experimental data for the asymmetric GroEL-GroES complex from small angle neutron and X-ray scattering are compared, only little differences were found. Fig. 7.3 shows this comparison of the experimentally derived $p(r)$ functions for the chaperonin complex from SAXS and SANS.

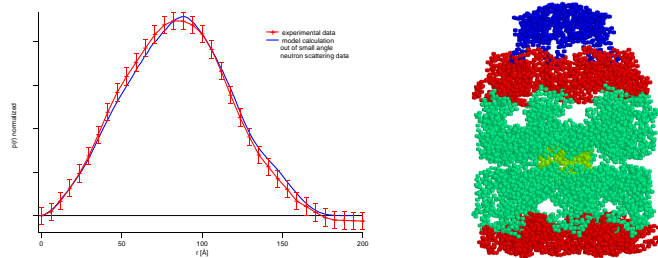


Fig. 7.4: The comparison of experimental data and model calculation of the asymmetric chaperonin complex (image right: model derived from small angle neutron scattering based on the crystal structure).

The data show a good agreement between the SANS and the SAXS data. Small deviations between the SANS and SAXS patterns of proteins in solution are reported by several authors[80, 81] and are due to the different contrast of proteins in aqueous environment. Whereas the different contrast of the interface protein - water envelop plays an important role. This might be an explanation for the small deviations in the $p(r)$ functions of the SANS and the SAXS experiment.

7.3.2 The Chaperonin Two-Stroke Mechanism and its Structural Intermediates

While the known structures of the asymmetric chaperonin complex are stable states in the presence of ADP, ATP introduce a kinetic behavior. From the analysis of the ATP-ase activity of the GroEL is known, that nucleotides are necessary for breaking the initial symmetry between the two GroEL heptameric rings. On the other hand facilitates the ATP the dissociation of the GroES from the GroEL. This process and the fact that the asymmetric complex shows a high affinity to hydrophobic surfaces indicates the important role of the ATP reaction for the chaperonin mediated protein folding. As shown

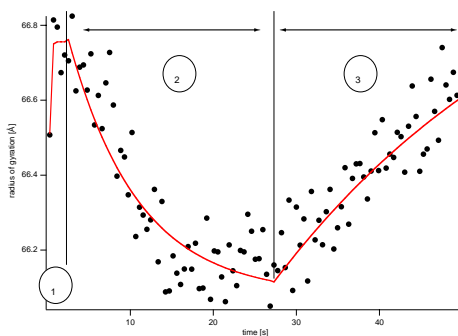


Fig. 7.5: The multi-phasic binding kinetics of the GroES to GroEL complex in the presence of ATP.

for the GroEL not the hydrolysis reaction itself causes the conformational changes, but the binding of the different nucleotides. The formation of the $\text{GroEL}_{\text{ATP}_7}$ -GroES transient state shows an kinetic constant of $k_{\text{Ass}} = 13 \times 10^5 \text{ M}^{-1} \text{ s}^{-1}$ (phase 1 in fig. 7.5), which is increased by a factor of four compared to the ADP. This fast phase within the first seconds of the multi-phasic kinetics indicates the binding of

the GroES to the allosterically switched GroEL after the ATP binding, forming the GroEL_{ATP₇}-GroES complex. Since biochemical data show, that the ATP-ase activity of the asymmetric GroEL-GroES complex starts immediately after the binding of ATP, the fast phase indicates that the GroEL-GroES-ATP₇ hydrolyses its ATP within 4s ($k_{con} = 0.25s^{-1}$). Thus, the kinetic constant indicates an enhanced ATP binding and hydrolysis due to the GroES binding. If the relaxation (phase 2 in fig. 7.5) of the hydrolyzing state to the ADP-bound ground state is caused by dissociation of the cleaved γ -phosphate can not be evidenced from this data. The hydrolysing GroEL_{ADP}-GroES relaxes to the ADP bound R-state within the next 20s.

It is known from the mixing experiment GroEL with ATP, that only one GroEL ring can bind and hydrolyse ATP, while the other is blocked. Therefore, the reaction should be halted after the relaxation in the GroEL_{ADP}-GroES complex. However, the time progression of the radius of gyration shows an increase after 28s, which can not be explained by an additional ATP binding reaction (phase 3 in fig. 7.5). This increase of the Rg-values after 28s can only be explained by the introduction of a third conformation. Indeed this third "activated" GroEL_{ADP}-GroES complex was proposed by Burston 1993[64] and investigated by Rye et al. using fluorescence labeled GroEL[40]. The formation of the activated complex is a slow reaction ($k_b = 0.05s^{-1}$) and the rate limiting step in the ATP-ase cycle. This finding is also in line with experimental data from the multiple ATP turnover. The stable Rg-values at 66.5Å indicates a steady state behavior. The increased concentration of the ATP allows the second GroEL ring to bind ATP. This restrains the system in the faster ATP hydrolysing state and the formation of the activated complex is inhibited. If the high concentration of ATP enhances the ATP hydrolysis, or if the _{ADP}GroEL_{ATP}-GroES state is a structure of a lower Rg-value can not be derived from this data.

From these results the following can be concluded:

1. The GroEL-ATP₇ state binds the GroES more rapid than the ADP-state
2. The GroES enhances the ATP hydrolysis reaction
3. An activated GroEL-GroES-ADP₇ complex is formed
4. The formation of this active complex is the slowest rate limiting step in the ATP-ase cycle.

A possible model for this reaction is shown in figure 7.6.

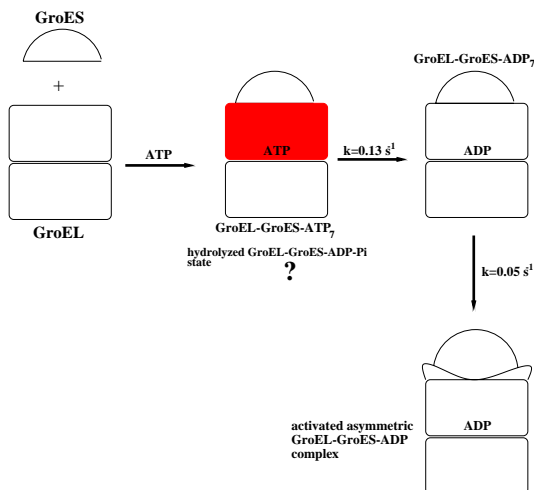


Fig. 7.6: Scheme for the reaction of GroEL with GroES in the presence of ATP

The biological relevance of the activated $\text{GroEL}_{ADP}\text{-GroES}$ complex is not quite clear. It is known from fluorescence measurements, that the formation of this complex is inhibited by substrate binding[40]. If the activated complex is the state of high affinity for substrate binding and acts like a tensed trap for denatured proteins, the nucleotide binding pockets of the trans GroEL ring should remain empty. The data for the multiple turnover experiment could fit into this model, because the binding pockets are occupied fast by ATP and the formation of the activated complex is inhibited. However the data for the kinetics of the preformed $\text{GroEL}_{ADP}\text{-GroES}$ complex in the presence of a single turnover ATP concentration provides a better insight to the reaction cycle. Indeed, the bi-phasic variation of the radius of gyration shows no formation of an activated complex.

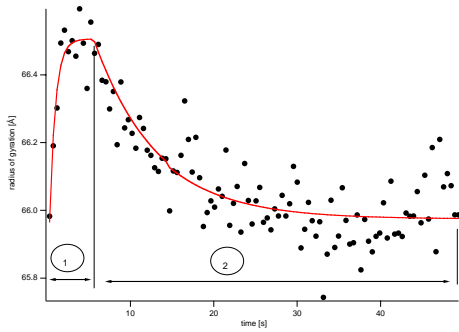


Fig. 7.7: The multi-phasic binding kinetics of the GroES to GroEL complex in the presence of ATP.

Further on the slower association rate of $k_{Ass} = 2.3 \times 10^5 M^{-1} s^{-1}$ indicates, that the anti-cooperativity of the GroEL rings force the ADP at the trans-GroEL ring to dissociate, before the cis-ring can completely hydrolyse the ATP (phase 1 in fig. 7.7). Whereas the lower Rg-value of 66.5 Å (compared to 66.8 Å for $\text{GroEL}_{ATP}\text{-GroES}$ hydrolysing state) indicates the $_{ADP}\text{-GroEL-}_{ATP}\text{-GroES}$ intermediate state. The flip of the GroES from the cis-ring to the trans ATP-bound ring can not be observed on this timescale. The GroES flip from the trans-ring to the cis-ring is the necessary step for the dissociation of the ADP. The relaxation from the hydrolysis state to the $\text{GroEL}_{ADP}\text{-GroES}$ state shows the same kinetic constant as for the ATP complex measured before (phase 2 in fig. 7.7). This suggests that the GroES flips to hydrolysing ATP-bound ring, because the system relaxes now in the same way as in the single turnover experiment with no additional ADP present. The third phase, the conversion to the activated complex can not be observed in this experiment. If the activated complex is strictly inhibited, or if the formation is retarded by the ADP can not be evidenced by this data.

From the results of the behavior of the stable GroEL-GroES-ADP_7 in the presence of ATP the following can be concluded:

1. The binding and hydrolysis of ATP to the trans ring of the chaperonin complex is retarded if ADP is bound on the cis ring.
2. A hydrolysing $(\text{ADP})_7\text{-GroEL-GroES-}(\text{ATP})_7$ complex is formed.
3. The ADP has to dissociate before the relaxation to the ADP-bound ground state starts
4. The formation of the activated chaperonin complex is retarded, or prohibited by the ADP

The possible reaction scheme for the kinetic behavior of the stable complex is shown in fig. 7.8:

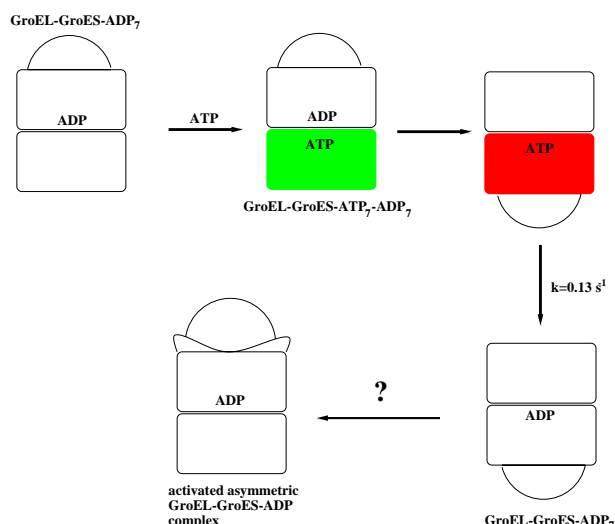


Fig. 7.8: Scheme for the reaction of stable chaperonin complex in the presence of ATP

7.3.3 Functional Relevance of the Intermediate GroEL-GroES-Nucleotide Complexes

From the data discussed above a switching mechanism between several major or transient conformations can be derived. The switching between these states is facilitated by the binding or conversion of nucleotides. While the analysis of the radius of gyration allows to identify the different states, the $p(r)$ (respectively the $\Delta p(r)$) functions detailed provide information about the rearrangements within the proteins. Since small angle scattering produces no data with atomic resolution, the structural intermediates formed during this "two stroke motor" movement (see also chapter 2.3) can be analysed in detail by using model calculation out of crystallographic data and images from electron microscopy. Differences between the ATP bound and the ADP bound states of GroEL-GroES are mainly reported by electron microscopic data. These data show overall deviation of the asymmetric GroEL-GroES complex upon ATP binding and hydrolysis.

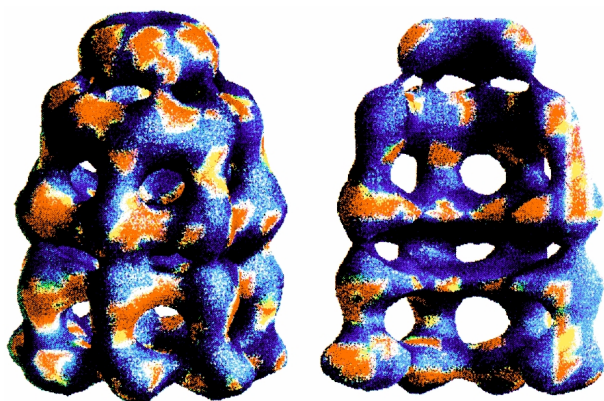


Fig. 7.9: Electron microscopic image of the GroEL-GroES-ATP₇ complex. The color decoding in blue and red indicates differences between the ATP bound state and the ADP state. (Roseman M.A., et al. Cell 97(3):325-38, 1999 Apr 30)

Since the GroEL-GroES-ATP complex is no longer a static structure and these cryo-EM data was not obtained using a time-resolved EM-method, it shows a mixture of ADP and ATP complexes. In difference to the crystallographic data, the EM-image shows a slight different GroES structure upon nucleotide binding. While in the crystal structure only a small part of the GroES, the so called "mobile

loops” are moved[66, 60], the red colored areas in the EM data indicate a shape change of the whole GroES dome due to ATP binding and hydrolysis (see fig. 7.9)[40].

This conformational changes of the GroES dome are also reported by static small angle neutron scattering studies[56]. In this static study the GroES was selectively investigated while it was bound to GroEL under contrast matching conditons (see Time resolved small angle neutron scattering). From this experiment a distance distribution function $p(r)$ for the GroES *in situ* (=bound to the GroEL in the presence of ADP) was derived (see fig. 7.10). The difference $\Delta p(r)$ (fig. 7.10(right)) between the

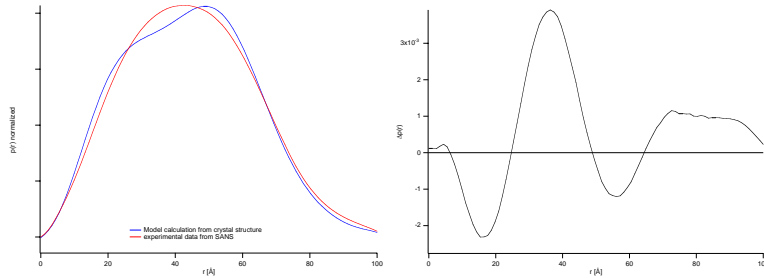


Fig. 7.10: Differences of GroES *in situ* structures. The experimental derived $p(r)$ for the GroES from SANS and the calculated out of the crystal structure show differences at 40Å.

GroES structure out of the crystallographic data (fig. 7.10(left): blue line) and the model structure from SANS (fig. 7.10(left): red line) show deviations mainly at 40Å. From model calculations was derived, that this deviations are linked to the opening and closing of the GroES dome[56, 82].

The conformational deviations between the ATP and ADP-bound state are dedicated due to the binding, hydrolysis and conversion of the ADP-bound state to the ”activated” complex. These three phases of the ATP cycle can be clearly distinguished in the data of the radius of gyration. The variation of the distances at 40Å can be denoted to the conformational changes within the GroES, while the changes at 120Å occur at the ATP hydrolysis. Like the EM data for the GroEL_{ADP}-GroES complex the crystal structure shows large conformational changes in both GroEL rings upon complex formation. These conformational changes within the GroEL rings are not visible in the small angle scattering. Figure 7.11 shows the differences in the $p(r)$ functions between the crystallographic structure and the small angle data. In $\Delta p(r)$ deviationes at 120Å.

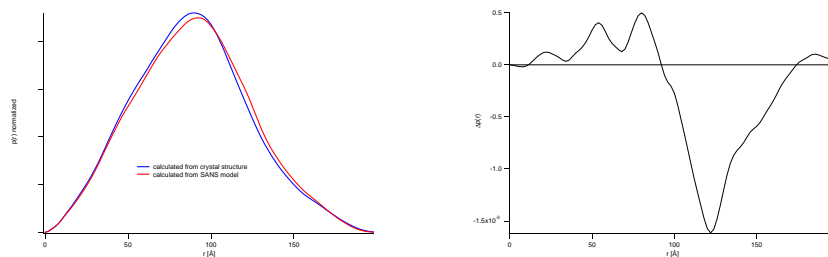


Fig. 7.11: Comparison of structures from X-ray crystallography and small angle neutron scattering. The differences $p(r)$ shows larger changes in the higher r -region.

These differences indicate overall changes within both GroEL rings upon the nucleotide cycle as remarked in the EM-images and the crystal structure. While crystallography and cryo-EM obtain only

stable or stalled structural intermediates, the experimental technique of time resolved small angle scattering provides the conversion between the intermediates. Therefore, the data suggest that the structure of the asymmetric GroEL-GroES-ADP₇ complex derived from X-ray crystallography is the activated complex, which is slowly build only after the ATP-hydrolysis.

8. CONCLUSIONS AND SUMMARY

Subject of this study is the time-dependent analysis of the ATP-ase reaction cycle of the *E. coli* chaperonins GroEL/GroES, using small angle scattering with X-rays and neutrons. The project comprised:

1. A technical task: The development of a stopped-flow device, suitable for the analysis of protein reaction in solution
2. A problem-oriented task: The analysis of the ATP-ase activity of the chaperonin system GroEL/GroES

Small angle scattering is a low resolution method. It provides information about the overall structure of the protein, as well as the distribution of distances within the protein. These data is not sufficient to derive 3-dim structural models. Detailed structural information can be obtained if the small angle scattering data can be compared with data from high resolution X-ray crystallography. If the comparison shows deviations between the small angle scattering data and the crystal structure, the crystal structure can be modified by model calculations and compared to the small angle scattering data. The result of the model calculation is an enhanced overall structure model for the solution structure.

This concept was applied to time-resolved small angle scattering. If the static X-ray structures of the proteins are used as starting and end conformations, the reaction can be traced by the deviations between the experimental data and the model calculations.

The chaperonin system GroEL/GroES fulfills the prerequisite of a successful time-resolved small angle scattering study. High resolution structural information from X-ray crystallography was available, and the kinetics of the system is well characterised by biochemical data. From these biochemical data structural intermediates are predicted for the chaperonin ATP-ase cycle. The verification of the kinetic data for the GroEL/GroES system as well as the identification and investigation of the predicted transient structure, were the second aim of this study.

8.1 *Time-Resolved Small Angle Scattering: Kinetic and Structural Data from Proteins in Solution*

The method of time-resolved small angle scattering can be used to follow the reaction of large protein assemblies. Since the classical small angle scattering methods, using a rotating anode, allow the taking of scattering patterns in the time range of hours, short exposure times can be obtained at high flux X-ray, or neutron facilities such as the synchrotrons ESRF and ELETTRA, or the high flux neutron reactor at the ILL. The use of third generation synchrotrons shifts the time-resolution into the sub-second time range, but causes problems due to radiation damage of the protein and limitations on the detector system.

X-rays: Problem of radiation damage and dead-time effects on the detector

The use of the high flux of X-ray photons produced by a synchrotron causes the problem of radiation damage. Under the high flux of 1×10^{11} ph/s the protein is damaged within the first 5s. This time range is not sufficient to follow the ATP-ase cycle of the chaperonins. The problem was overcome by the development of a continuous stopped-flow device. A conventional stopped-flow device consists of two syringes, which are used for the mixing of the reactants. The advanced continuous stopped-flow device consists of an additional syringe. Thus, the sequence of mixing of the advanced setup is slightly different. First the two mixing syringes fill an extended reaction loop. This premixed, non-irradiated sample is pushed through the X-ray beam by the third buffer-filled syringe. Using this enhanced device time-resolved data over 50s could be recorded.

Another problem for time-resolved small angle X-ray scattering is the dead-time effects of conventional gas-filled delay line detectors under high flux conditions. This problem was overcome by using a CCD-detector. The FRELON CCD-camera, developed by the ESRF detector group, is able to detect the full flux of photons, but has a slower readout of 150ms. This limits the time resolution to 150ms. During this study the FRELON CCD-camera was upgraded several times and adapted to the high flux conditions of the time-resolved small angle scattering technique.

Neutrons: No radiation damage, but low flux

The problem of radiation damage can be avoided completely by the use of cold neutrons. In contrast to X-ray photons of 12keV ($\approx 1\text{\AA}$ wavelength), cold neutrons of $\lambda=8\text{\AA}$ ($=1.3\text{meV}$) cause no radiation damage. However, the applicability of time-resolved small angle scattering is limited by the flux of neutrons. The available small angle neutron scattering beamlines (ILL, D22) provide a flux of about 3×10^7 neutrons/s. The lower flux of neutrons can partly be compensated by using deuterated proteins and buffer solutions containing D_2O , as well as with the larger beamsize of the neutron beam. Small angle neutron scattering patterns can be obtained with a time resolution of 1s. The method of contrast variation, which can only be applied to neutron scattering gives complementary data to the X-ray experiments and further information of the reaction kinetics of the proteins can be obtained.

The structural parameter of small angle scattering is firstly the radius of gyration (R_g) and secondly the distance distribution function $p(r)$. Whereas the R_g -value can be estimated directly from the scattering data, the $p(r)$ function has to be calculated via Fourier transformation of the scattering intensities. Since the recently available Fourier transformation programs are not capable of evaluating time-resolved data, the direct transformation method was used. This direct transformation allows the calculation of one single time resolved experiment of 110 time frames within 2h, and no difference to the well established indirect transformation method was found.

8.2 The Chaperonin "two-stroke" Engine at Work

The chaperonins GroEL and GroES are helper proteins which assist the protein folding by binding to hydrophobic patches of denatured proteins or nascent polypeptide chains. The main-chaperonin GroEL, a 14mer with a barrel-like double ring structure of 800kDa mass, binds to hydrophobic surfaces of denatured proteins, preventing protein aggregation and provides the refolding in the native structure. For the chaperon mediated protein refolding a "two-stroke engine" model was proposed by G. Lorimer (1997) and P.B. Sigler (1998)[65, 66]. In this study the first steps of this model, the nucleotide binding

and hydrolysis reaction were investigated.

Biochemical data from literature suggest a remarkable interplay between cooperativity and anti-cooperativity as a common regulatory scheme for the chaperonin ATP-ase activity. While the binding of nucleotides on one ring of the double ring GroEL is a highly cooperative reaction, the second ring anti-cooperatively blocks for nucleotide binding.

The cooperative ATP binding is allosterically regulated

The multi-phasic behavior of the GroEL - ATP kinetics, proves the existence of at least one structural intermediate. This state was identified as the ATP binding state during which the ATP-hydrolysis takes place. This state is formed immediately (<150ms) after the mixing and shows a stable phase of 8s (at single turnover ATP concentrations). From the stable phase of 8s a single turnover ATP hydrolysis rate of $k_{Hyd} = 0.13s^{-1}$ was determined, which is in line with biochemical data from literature. The rapid conformational change and the subsequent hydrolysis phase indicates that the cooperative ATP binding is facilitated by an allosteric switch of the GroEL. This allosteric switch transforms one GroEL heptameric ring into an ATP enhanced binding state, by binding a single ATP molecule to the nucleotide binding pockets of one GroEL subunit. This allosteric switch of the protein structure was proposed from biochemical data and by theoretical considerations, and is investigated in this study by a structural signal for the first time.

It is remarkable, that the GroEL subunit remains in the allosterically switched state until the ATP hydrolysis is finished in all seven subunits. The relaxation of the subunits to the GroEL ADP-bound ground state occurs afterwards as a statistical process. From these findings it can be concluded that, it is not the hydrolysis of the ATP to ADP, which facilitates the conformational change, but the binding of the ATP.

Breaking of the GroEL double ring symmetry is an important feature

Since the binding of ATP and its hydrolysis to ADP breaks the symmetry of the two non-distinguishable GroEL rings, symmetrical and antisymmetrical binding of ligands seems to play an important role in the ATP-ase cycle of the chaperonin. This view is supported by the binding behavior of the co chaperonin GroES. The 7-meric, dome shaped GroES molecule (molecular weight 70kDa) binds in the presence of ADP to one end of the GroEL cylinder, forming the asymmetric GroEL-GroES complex. The formation of this stable complex is known to be fast and a pseudo association constant of $k_{ass} = 4 \times 10^5 M^{-1}s^{-1}$ was obtained and verified by data from literature. The asymmetric GroEL-GroES complex shows a high affinity for denatured substrate protein and plays an important role in the chaperonin-mediated protein folding.

The binding of a second GroES molecule to the opposite ring of the GroEL, would not allow the binding of substrate protein. Thus, the formation of the symmetric GroES-GroEL-GroES complex is inhibited by the allosteric switch. Allosteric switching can enhance the binding of ligands (=cooperative binding), or inhibit the binding of ligands (=anti-cooperativity). In the case of GroEL the formation of the symmetric complex is found only in the presence of high ATP concentrations ($c_{ATP} > 5mM$). This high ATP concentration overrides the anti-cooperativity of the nucleotide binding and both GroEL rings can act as "single" rings. The suppression of the anti-cooperativity is reflected in a bi-phasic formation kinetics. In a fast phase, the asymmetric complex is formed and the symmetric complex is formed in a slower second phase. This bi-phasic behavior of the symmetric GroES binding was observed in this

study for the first time, using selectively labelled deuterated proteins and time-resolved small angle neutron scattering.

Interplay of GroES and nucleotides - the second allosteric switch?

The kinetics of GroEL shows an allosteric switch in the presence of ATP. The relevance of the allosterically activated GroEL is reflected in the multi-phasic kinetics of the GroEL/GroES system. The formation of the GroEL-GroES complex in the presence of ATP shows an elevated association rate of $k_{ass} = 13 \times 10^5 M^{-1} s^{-1}$ as for the formation of the asymmetric GroEL-GroES complex in the presence of ADP, and starts immediately after the mixing. This finding suggests, that the GroES binds to the allosterically switched GroEL, whereas the binding of GroES enhances the ATP hydrolysis rate for the single turnover to $k_{Hyd}=0.25s^{-1}$. Thus, small angle scattering would suppose a second allosteric switch upon GroES binding, which enhances the ATP hydrolysis. This finding is in line with a fluorescence study, which supposes that GroES "commits" the GroEL to hydrolyse ATP.

This transiently formed GroEL-GroES ATP hydrolysis complex relaxes to the GroEL-GroES ADP bound ground state afterwards. It is remarkable that after this decay a third GroEL-GroES complex is formed. This "activated" GroEL-GroES complex is formed very slowly ($k_{act} = 0.03s^{-1}$) and was proposed by biochemical data and investigated by fluorescence. The formation constant out of the small angle scattering data could be verified by fluorescence data from literature, but is measured in this study for the first time by a structural signal. The formation of the activated complex is the rate limiting step and is inhibited in the presence of an excess concentration of ADP. The physiological function of the activated complex is not quite clear, maybe it acts like a tensed trap for denatured protein. Maybe it is not a very physiological complex, because of the presence of \approx mM concentration of ADP in the cell.

9. OUTLOOK

This study shows, that time-resolved small angle scattering is a useful method for the investigation of protein-protein and protein-ligand interactions. The method is mainly limited by the mixing device and the detector system. For the investigation of processes in the ms time range, enhanced time-resolved techniques have to be applied. The use of a continuous flow device, a quite different technique for time-resolved small angle scattering, could overcome the problems of mixing and of the limiting readout structure of the detector. For this two different techniques are possible. Firstly the continuous flow of mixed sample through the X-ray beam, whereas the time resolution is defined by the flow of reactants. This method is capable for short time points, but needs a lot of material. It is already successfully used for time-resolved small angle scattering studies on protein folding.

The second continuous flow method is based on the idea not only to move the sample through the beam, but also the sample capillary. For this the first irradiation point is close to the mixing point and records a fixed time point in ms time range. The mixing of the cuvette is finished after a certain time, which have to be adjusted. After the flow is stopped, the capillary is scanned by the X-ray beam. The time points can be recalculated from the scanning velocity. This method would allow to investigate a longer time period by saving sample. The time resolution is limited by the beamsize of the X-ray beam. For the continuous flow without moving the capillary, a static detector system such as an image plate can be used. It has to be read-out after every time point, but can detect a high flux of photons with high efficiency and high spatial resolution. The moving capillary method would need a fast read-out camera as described for the classical time-resolved small angle X-ray scattering. Recent developments by the detector groups of the ESRF and the ELETTRA, try to overcome these problems.

The use of neutrons would enhance the time-resolved small angle neutron scattering technique, because of the contrast variation method. This technique would allow to trace the conformational changes of one reactant during a reaction cycle. However, the flux of neutrons is limited. Maybe, the new high flux neutron facilities increase the flux of neutrons and time-resolved small angle scattering becomes capable to the subsecond time range.

For the chaperonin system GroEL/GroES the important part of the chaperonin mediated protein folding has to be analysed, the binding and release of substrate protein. Due to the unspecific binding of denatured protein to the chaperonin, crystallographic structures of the chaperonin-substrate protein complex, may not be obtained. Thus, small angle scattering is the method of choice for this task.

Acknowledgement

I am especial grateful to Dr. Hermann Heumann, for the possibility to carry out this work in his group at the Max-Planck-Institut für Biochemie, for his attention, encouragement and last but not least the financial support.

I am also grateful to Prof. E. Sackmann for supporting me as an external Ph.D student at the Technischen Universität München/Physikdepartment.

I would like to thank Prof. P. Fromherz for the possibiltiy to use the facilities and the infrastucture of the Department "Membran und Neurophysik" at the Max-Planck-Institut für Biochemie.

Big thanks to Dipl.Chem Elena Manakova, she gave me insights into biochemistry and without her biochemical work the project would never be realizable.

I thank our collaborators on the time-resolved small angle scattering project, Dr. Thomas Nawroth and Dipl. Chem Iris Lauer from the Biochemischen Institut/Universität Mainz. They build up and maintained the temperatur controlled sample box. Also thanks a lot for the long and usefull discussions during the nightshifts at the synchrotrons and the friendly contact.

I would like to thank the scientific staff at the synchrotrons ESRF in Grenoble and ELETTRA in Trieste, especially Peter Bösecke, Olivier Diat, Pierre Panine and Theyencheri Narayanan from ESRF's ID2 and Sigrid Bernstorff and Heinz Amenitsch from ELETTRA's SAXS beamline.

The neutron scattering data were obtained together with Dr. R. May and Dipl.Biol. Jörg Holzinger at the Institut Laue-Langevin in Grenoble. Thanks a lot for the support and the very usefull discussions about small angle scattering of proteins!

I thanks the members of Hermann Heumanns group for interesting discussion, the friendly contact and all the other "little" things, which are necessary for scientific work. Thanks also to Dr. Renata Stegmann, she started with the project of small angle scattering on the chaperonin system GroEL/GroES and her static results were the starting point of the time-resolved project.

Special thanks to Walter Wagner and Robert Pabst from the mechanic workshop of the department "Membran und Neurophysik". The stopped-flow device would never run without the work of these two excellent mechanics!

Big thanks to Lynn Hromek and Elena Manakova, for carefull reading of the manuscript and the suggestions and corrections.

Special thanks to my family, Silvia and Leo, for the patient, the support and the encouragement.

BIBLIOGRAPHY

- [1] H. Frauenfelder, S.G. Sligar, and P.G. Wolynes. The energy landscapes and motions of proteins. *Science*, 254(5038):1598–603, 1991.
- [2] A.E. Garcia, J.A. Krumhansl, and H. Frauenfelder. Variations on a theme by Debye and Waller: from simple crystals to proteins. *Proteins.*, 29(2):153–60, 1997.
- [3] S. Cusack. Neutron and synchrotron radiation for condensed matter studies. Les editions de physique-Springer Verlag, 1994. Volume III.
- [4] S.A. Endow. Determinants of molecular motor directionality. [Review] [60 refs]. *Nature Cell Biology*. 1(6):E1, 1(6):163–7, 1999.
- [5] R.D. Vale and R.A. Milligan. The way things move: looking under the hood of molecular motor proteins. [review] [77 refs]. *Science*, 288(5463):95–100, 2000.
- [6] K. Jr. Kinoshita. Real time imaging of rotating molecular machines. [Review] [31 refs]. *FASEB Journal*, 13(Suppl. 2):201–8, 1999.
- [7] A. Mattevi, M. Rizzi, and M. Bolognesi. New structures of allosteric proteins revealing remarkable conformational changes. *Current Opinion in Structural Biology*, 6(6):824–9, 1996.
- [8] K.E. Neet. Cooperativity in enzyme function: equilibrium and kinetic aspects. *Methods in Enzymology*. 249:519–67, 1995. 95311753, 249:519–67, 1995.
- [9] J. Monod, J. Wyman, and J.P Changeux. On the nature of allosteric transitions: a plausible model. *Journal of Molecular Biology*, 12:88–118, 1965.
- [10] M.F. Perutz. Mechanisms of cooperativity and allosteric regulation in proteins. [review]. *Quarterly Reviews of Biophysics*, 22(2):139–237, 1989.
- [11] K. Moffat. Time-resolved crystallography. [Review]. *Acta Crystallographica - Section A - Foundations of Crystallography*, 54(Pt6-Pt1):833–41, 1998.
- [12] I. Schlichting. Crystallographic structure determination of unstable species. [Review]. *Accounts of Chemical Research*, 33(8):532–8, 2000.
- [13] B. Perman, V. Srajer, Z. Ren, T. Teng, C. Pradervand, Ursby T., D. Bourgeois, F. Schotte, M. Wulff, R. Kort, K. Hellingwerf, and K. Moffat. Energy transduction on the nanosecond time scale: early structural events in a xanthopsin photocycle. *Science*, 279:1946–1950, 1997.
- [14] B. Perman, S. Anderson, M. Schmidt, and K. Moffat. New techniques in fast time-resolved structure determination. [Review]. *Cellular & Molecular Biology*, 46(5):895–913, 2000.

- [15] M.H. Chestnut, D.P. Siegel, J.L. Burns, and Y. Talmon. A temperature-jump device for time-resolved cryo-transmission electron microscopy. *Microscopy Research & Technique*, 20(1):95–101, 1992.
- [16] E.M. Mandelkow, E. Mandelkow, and R.A. Milligan. Microtubule dynamics and microtubule caps: a time-resolved cryo-electron microscopy study. *Journal of Cell Biology*, 114(5):977–91, 1991.
- [17] H.R. Saibil. Conformational changes studied by cryo-electron microscopy. [review] [31 refs]. *Nature Structural Biology*. 7(9):711-4, 2000, 7(9):711–4, 2000.
- [18] A.K. Bhuyan and J.B. Udgaonkar. Stopped-flow NMR measurement of hydrogen exchange rates in reduced horse cytochrome c under strongly destabilizing conditions. *Proteins*, 32(2):241–247, 1998.
- [19] M. Roessle, E. Manakova, I. Lauer, T. Nawroth, J. Holzinger, T. Narayanan, S. Bernstorff, H. Amenitsch, and H. Heumann. Time-resolved small angle scattering: Kinetic and structural data from proteins in solution. *Journal of Applied Crystallography*, 33(3):548–551, 2000.
- [20] J. Trewella. Insights into biomolecular function from small-angle scattering. *Current Opinion in Structural Biology*, 7(5):702–8, 1997.
- [21] A. Neidhart, T. Nawroth, M. Huetsch, and K Dose. Structural dynamics in F1ATPase during the first reaction cycle of ATP hydrolysis. *FEBS Letters*, 280(1):179–82, 1991.
- [22] M. Roessle, E. Manakova, I. Lauer, T. Nawroth, R. Gebhardt, T. Narayanan, and H. Heumann. Time-resolved SAXS study of the conformational changes in the chaperonin system GroE. *ESRF Newsletters*, 33:10–11, Oktober 1999. Experimental Report.
- [23] C.B. Anfinsen. Principles that govern the folding of protein chains. *Science*, 181:223–230, 1973.
- [24] G.W. Farr, E.C. Scharl, R.J. Schumacher, S. Sondek, and A.L. Horwich. Chaperonin-mediated folding in the eukaryotic cytosol proceeds through rounds of release of native and nonnative forms. *Cell*, 89(6):927–37, 1997.
- [25] F.U. Netzer, W.J. Hartl. Protein folding in the cytosol: chaperonin-dependent and -independent mechanisms. [Review] [34 refs]. *Trends in Biochemical Sciences*, 23(2):68–73, 1998.
- [26] S.B. Zimmermann and A.P. Minton. Macromolecular crowding: Biochemical, biophysical and physiological consequences. *Annu. Rev. Biophys. Biomol. Struc.*, 22:27–65, 1993.
- [27] S.B. Zimmermann and S. O Trach. Estimation of macromolecular concentrations and excluded volume effects for the cytoplasm of escherichia coli. *Journal of Molecular Biology*, 222:599–620, 1991.
- [28] J. Martin and F.U. Hartl. The effect of macromolecular crowding on chaperonin-mediated protein folding. *Proceedings of the National Academy of Sciences of the United States of America*, 94(4):1107–12, 1997.

- [29] J. Zeilstra-Ryalls, O. Fayet, and C. Georgopoulos. The universally conserved GroE (Hsp60) chaperonins. *Ann. Review of Microbiology*, 45:301–325, 1991.
- [30] A.J. Macario and E.C. de Macario. The archaeal molecular chaperone machine: peculiarities and paradoxes. [Review] [56 refs]. *Genetics*, 152(4):1277–83, 1999.
- [31] J. Martin and F.U. Hartl. Chaperone-assisted protein folding. *Current Opinion in Structural Biology*, 7(1):41–52, 1997.
- [32] D. Ruggero, A. Ciammaruconi, and P. Londei. The chaperonin of the archaeon *Sulfolobus solfataricus* is an RNA-binding protein that participates in ribosomal RNA processing. *EMBO Journal*, 17(12):3471–7, 1998.
- [33] A.L. Fink. Chaperone-mediated protein folding. [Review] [274 refs]. *Physiological Reviews*, 79(2):425–49, 1999.
- [34] W.A. Houry, D. Frishman, C. Eckerskorn, F. Lottspeich, and F.U. Hartl. Identification of in vivo substrates of the chaperonin GroEL. *Nature*, 402(6758):147–54, 1999.
- [35] R.J. Ellis. Molecular chaperones. opening and closing the anfinen cage. *Current Biology*. 4(7):633-5, 1994, 4, 1994.
- [36] R.J. Ellis. Revisiting the anfinen cage. *Folding & Design*. 1(1):R9-15, 1, 1(1):9–15, 1996.
- [37] P. Csermely. Chaperone-percolator model: a possible molecular mechanism of Anfinsen-cage-type chaperones. *Bioessays*, 21(11):959–65, 1999.
- [38] O. Llorca, A. Galan, J.L. Carrascosa, A. Muga, and J.M. Valpuesta. GroEL under heat-shock. Switching from a folding to a storing function. *Journal of Biological Chemistry*, 273(49):32587–94, 1998.
- [39] M.S. Goldberg, J. Zhang, S. Sondek, C.R. Matthews, R.O. Fox, and A.L. Horwich. Native-like structure of a protein-folding intermediate bound to the chaperonin GroEL. *Proceedings of the National Academy of Sciences of the United States of America*, 94(4):1080–5, 1997.
- [40] H.S. Rye, A.M. Roseman, S. Chen, K. Furtak, W.A. Fenton, and A.L. Saibil, H.R. and Horwich. GroEL-GroES cycling: ATP and nonnative polypeptide direct alternation of folding-active rings. *Cell*, 97(3):325–38, 1999.
- [41] O. Yifrach and A. Horovitz. Nested cooperativity in the atpase activity of the oligomeric chaperonin groel. *Biochemistry*. 34(16):5303-8, 1995 Apr 25., 34(16):5303–8, 1995.
- [42] O. Yifrach and A. Horovitz. Coupling between protein folding and allostery in the GroE chaperonin system. *Proceedings of the National Academy of Sciences of the United States of America*., 97(4):1521–4, 2000.
- [43] O. Llorca, M.G. Smyth, J.L. Carrascosa, K.R. Willison, M. Radermacher, S. Steinbacher, and J.M. Valpuesta. 3D reconstruction of the ATP-bound form of CCT reveals the asymmetric folding conformation of a type II chaperonin. *Nature Structural Biology*, 6(7):639–42, 1999.

- [44] I. Gutsche, L.O. Essen, and W. Baumeister. Group II chaperonins: new TRic(k)s and turns of a protein folding machine. [Review] [109 refs]. *Journal of Molecular Biology*, 293(2):295–312, 1999.
- [45] I. Gutsche, J. Holzinger, M. Roessle, H. Heumann, W. Baumeister, and R.P. May. Conformational rearrangements of an archaeal chaperonin upon ATPase cycling. *Current Biology*. 10(7):405-8, 2000, 10(7):405–8, 2000.
- [46] R.J. Ellis. Proteins as molecular chaperones. *Nature*, 328:378–379, 1987.
- [47] R.J. Ellis, editor. *The Chaperonis*. Academic Press, 1996.
- [48] H.R.B. Pelham. Speculations of the major heat shock and glucose-regulated proteins. *Cell*, 46:956–961, 1986.
- [49] E.S. Bochkareva, N.M. Lissin, and A.S. Grishovich. Transient association of newly synthesized unfolded proteins with the heat-shock proteins GroEL. *Nature*, 336:254–257, 1988.
- [50] J.P. Hendrick and F.U. Hartl. Molecular chaperone functions of heat shock proteins. *Annual Review of Biochemistry*, 62:349–384, 1993.
- [51] T. Langer, G. Pfeifer, J. Martin, W. Baumeister, and F.U. Hartl. Chaperonin mediated protein folding: GroES binds to one end of the GroEL cylinder, which accomodates the protein substrate within its central cavity. *EMBO*, 11:4757, 1992.
- [52] K. Braig, Z. Otwinowski, R. Hedge, D. C. Boisvert, A. Joachimiak, A. L. Horwich, and P. B. Sigler. The crystal structure of the bacterial chaperonin GroEL at 2.8Å resolution. *Nature*, 371:578–586, 1994.
- [53] Z. Lin, F. Schwarz, and E. Eisenstein. The hydrophobic nature of GroEL-substrate binding. *Journal of Biological Chemistry*, 270:1011–1014, 1995.
- [54] J.L. Feltham and L.M. Gierasch. Groel-substrate interactions: molding the fold, or folding the mold?. [Review] [19 refs]. *Cell*, 100(2):193–6, 2000.
- [55] K. Braig, P. D. Adams, and A. T. Bruenger. Conformational variabilty in the refined structure of the chaperonin GroEL at 2.8Å resolution. *Nature Structural Biology*, 2:1083–1094, 1995.
- [56] R. Stegmann, E. Manakova, M. Roessle, H. Heumann, S. E. Nieba-Axmann, Pluckthun A., T. Hermann, R. P. May, and A. Wiedenmann. Structural changes of the Escherichia coli GroEL-GroES chaperonins upon complex formation in solution: a neutron small angle scattering study. *Journal of Structural Biology*, 121(1):30–40, 1998.
- [57] P. Thiagarajan, S.J. Henderson, and A. Joachimiak. Solution structures of Groel and its complex with rhodanese from small angle neutron scattering. *Structure*, 4(1):79–88, 1996.
- [58] J. F. Hunt, A. J. Weaver, S. J. Landry, L. Gierasch, and J. Deisenhofer. The crystal structure of the GroES co-chaperonin at 2.8Å resolution. *Nature*, 379:37–45, 1996.

- [59] S. Landry, A. Taher, C. Georgopoulos, and S.M. van der Vies. Interplay of structure and disorder in the co-chaperonin mobile loops. *Proceedings of the National Academy of Sciences of the United States of America*, 93:11622–11627, 1996.
- [60] Z. Xu, A.L. Horwich, and P.B. Sigler. The crystal structure of the asymmetric GroEL-GroES-(ADP)₇ chaperonin complex [see comments]. *Nature*, 388(6644):741–50, 1997.
- [61] M.K. Hayer-Hartl, K.L. Ewalt, and F.U. Hartl. On the role of symmetrical and asymmetrical chaperonin complexes in assisted protein folding. *Biological Chemistry*, 380(5):531–40, 1999.
- [62] M.J. Cliff, N.M. Kad, N. Hay, P.A. Lund, M.R. Webb, S.G. Burston, and A.R. Clarke. A kinetic analysis of the nucleotide-induced allosteric transitions of GroEL. *Journal of Molecular Biology*, 293(3):667–84, 1999.
- [63] J. Ma, P.B. Sigler, Z. Xu, and M. Karplus. A dynamic model for the allosteric mechanism of GroEL. *Journal of Molecular Biology*, 302(2):303–13, 2000.
- [64] G.S. Jackson, R.A. Staniforth, D.J. Halsal, T. Atkinson, J.J. Holbrook, A.R. Clarke, and S. G. Burston. Binding and hydrolysis of nucleotides in the chaperonin catalytic cycle: Implications for the mechanism of assisted protein folding. *Biochemistry*, 32:2554–2563, 1993.
- [65] G. Lorimer. Protein folding. Folding with a two-stroke motor [news; comment]. *Nature*, 388(6644):720–1, 1997.
- [66] Z. Xu and P.B. Sigler. GroEL/GroES: structure and function of a two-stroke folding machine. [Review] [63 refs]. *Journal of Structural Biology*, 124(2-3):129–41, 1998.
- [67] P. Debye. Scattering of non-crystallin substances. *Ann. Phys.*, 46:809–823, 1915.
- [68] S.J. Perkins. Protein volumes and hydration effects. *European Journal of Biochemistry*, 157:169–180, 1986.
- [69] O. Glatter. Skriptum für die Vorlesung Streumethoden. Institut für phys. Chemie, Karl-Franzens-Universität.
- [70] A. Guinier and G. Fournet. *Small angle scattering of X-ray*. Wiley & sons, New York, 1955.
- [71] O. Glatter. A new method for the evaluation of small angle scattering data. *Journal of Applied Crystallography*, 10:415–421, 1997.
- [72] F.J. Corrales and A.R. Fersht. Kinetic significance of GroEL₁₄.(GroES₇)₂ complexes in molecular chaperone activity. *Folding & Design*, 1(4):265–73, 1996.
- [73] S.E. Nieba-Axmann, M. Ottiger, K. Wuthrich, and A. Pluckthun. Multiple cycles of global unfolding of GroEL-bound cyclophilin A evidenced by NMR. *Journal of Molecular Biology*, 271(5):803–18, 1997.
- [74] H. Grallert and J. Buchner. Analysis of GroE-assisted folding under nonpermissive conditions. *Journal of Biological Chemistry*, 274(29):20171–7, 1999.

- [75] H. Lederer, R. P. May, J. K. Kjems, W. Schaefer, H. L. Crespi, and H. Heumann. Deuterium incorporation into *Escherichia coli* proteins. A neutron-scattering study of DNA-dependent RNA polymerase. *European Journal of Biochemistry*, 156(3):655–9, 1986.
- [76] J. Drenth. *Principles of Protein X-ray Crystallography*. Springer, 1999.
- [77] D. Blow. So do we understand how enzymes work?. [Review]. *Structure*, 8(4):R77–81, 2000.
- [78] D.C. Boisvert, J. Wang, Z. Otwinowski, A.L. Horwich, and P.B. Sigler. The 2.4 Å crystal structure of the bacterial chaperonin GroEL complexed with ATP gamma S. *Nature Structural Biology*, 3(2):170–7, 1996.
- [79] M.K. Hayer-Hartl, J. Martin, and F.U. Hartl. Asymmetrical interaction of GroEL and GroES in the ATPase cycle of assisted protein folding. *Science*, 269:836–841, 1995.
- [80] D.I. Svergun, S. Richard, M.H. Koch, Z. Sayers, S. Kuprin, and G. Zaccai. Protein hydration in solution: experimental observation by x-ray and neutron scattering. *Proceedings of the National Academy of Sciences of the United States of America*, 95(9):2267–72, 1998.
- [81] D. I. Svergun, M. H. Koch, J. S. Pedersen, and I. N. Serdyuk. Structural model of the 50S subunit of *E. coli* ribosomes from solution scattering. *Basic Life Sciences*, 64:149–74, 1996.
- [82] M. Roessle. Untersuchungen zur Struktur und Funktion des *E. coli* Chaperoninsystems GroEL und GroES mit Hilfe der Neutronenkleinwinkelstreuung. Master's thesis, Ludwigs-Maximilians-Universitaet Muenchen, 1997.

APPENDIX

The Debye Equation

The overall scattering amplitude of an ensemble of scattering points can be calculated by superposition of all scattered waves.

$$A(\vec{q}) = \sum_k A_k = \sum_k b_k e^{-i\vec{q} \cdot \vec{r}} \quad (.1)$$

Whereas the \vec{q} describes the momentum transfer vector of the scattered wave, \vec{r} the difference vector from one scattering center to the other and the b_k the scattering length (see fig. ??). For the scattering on proteins the discrete scattering length b_k has to be transformed to the electron density $\rho(\vec{r})$:

$$\rho(\vec{r}) = \frac{1}{V} \sum_k f_k \delta(\vec{r} - \vec{r}_k) \quad (.2)$$

Thus, the superposition of the scattered waves from scattering centers within the volume V can be described in integral form:

$$A(\vec{q}) = \int_V \rho(\vec{r}) e^{-i\vec{q} \cdot \vec{r}} dV \quad (.3)$$

The result of a scattering experiment is the scattering intensity $I(\vec{q})$. The scattering intensity represents the multiplication of the overall scattering amplitude $A(\vec{q})$ with its complex conjugated $A^*(\vec{q})$.

$$I(\vec{q}) = A(\vec{q}) \cdot A^*(\vec{q}) \quad (.4)$$

The multiplication described in (4) convolutes equation (3) and the integral

$$I(\vec{q}) = \int_{V'} \int_{V''} \rho(\vec{r}') \rho(\vec{r}'') e^{-i\vec{q} \cdot \vec{r}'} e^{-i\vec{q} \cdot \vec{r}''} dV' dV'' \quad (.5)$$

is obtained.

The substitution with

$$\vec{r} = \vec{r}' - \vec{r}''$$

leads to

$$I(\vec{q}) = \int_{V''} \int_V \rho(\vec{r}'') \rho(\vec{r}'' - \vec{r}) e^{-i\vec{q} \cdot \vec{r}} dV'' dV \quad (.6)$$

Whereas the convolution integral of $\rho^*(\vec{r}'')$ defines the auto correlation function and can be written as

$$I(\vec{q}) = \int_V \rho^*(r)^2 e^{-i\vec{q} \cdot \vec{r}} dV \quad (.7)$$

In the theoretical considerations above the assumption was made, that there is only one vector \vec{r}_k . This is true for a single molecule, or for a perfect crystal. In a perfect single crystal, many vectors \vec{r}_k exists, but all of these vectors have the same orientation and length. This is not the case, if the scattering

particles are in solution. In an ideal solution all orientations of the vector \vec{r}_k occur, and the \vec{r}_k has to be averaged of all possible orientations.

Thus, in equation (7) the convoluted $\rho^*(\vec{r})^2$ and the exponential equation have to be spatial averaged.

$$\langle e^{-i\vec{q}\cdot\vec{r}} \rangle = \int_{Orient.} e^{-i\vec{q}\cdot\vec{r}} d\vec{r}_{Orient.} \quad (.8)$$

Using $d\vec{r}_{Orient.} = \frac{1}{2} \sin\varphi d\varphi$, the spatial averaging results in:

$$\langle e^{-i\vec{q}\cdot\vec{r}} \rangle = \int_0^{2\pi} e^{-iq \cdot r \cos\varphi} \frac{1}{2} \sin\varphi d\varphi \quad (.9)$$

$$= \int_0^{2\pi} \frac{1}{2} \cos(qr \cos\varphi) \sin\varphi d\varphi + i \int_0^{2\pi} \frac{1}{2} \sin(qr \cos\varphi) \sin\varphi d\varphi \quad (.10)$$

$$= \frac{1}{2qr} \int_{qr}^{-qr} \cos(u) du + \frac{i}{2qr} \int_{qr}^{-qr} \sin(u) du \quad (.11)$$

$$= \frac{1}{2qr} (\sin(qr) + \sin(qr)) + \frac{i}{2qr} (\cos(qr) - \cos(qr)) \quad (.12)$$

$$\langle e^{-i\vec{q}\cdot\vec{r}} \rangle = \frac{\sin(qr)}{qr} \quad (.13)$$

Whereas $q = |\vec{q}| = \frac{2\pi}{\lambda} \sin 2\Theta$ describes now the norm of the \vec{r} .

The spatial averaging of the auto-correlation function in (7) results in:

$$\langle \rho^*(\vec{r})^2 \rangle = \rho(|\vec{r}|)^2 = \rho^*(r)^2 \quad (.14)$$

And the **Debye equation** can be calculated after the transforming into spherical coordinates.

$$I(q) = \int_V \rho^*(r)^2 \frac{\sin(qr)}{qr} dV \quad (.15)$$

$$I(q) = 4\pi \int_0^\infty \rho^*(r)^2 r^2 \frac{\sin(qr)}{qr} dr \quad (.16)$$

Debye 1915

The Debye equation (16) has to be calculated over infinite r -range. However, scattering particles have finite dimensions. Out of the maximal dimension (D_{max}) of the molecule no electron density can be defined. Using this, the averaged auto-correlation function in (16) can be simplified to the so-called correlation function $\gamma(r)$

$$\rho^*(r) = \gamma(r) + \text{const} \quad (.17)$$

$$I(q) = 4\pi \int_0^{D_{max}} \gamma(r) r^2 \frac{\sin(qr)}{qr} dr \quad r < D_{max} \quad (.18)$$

Defining the $\gamma(r)r^2$ as the distance distribution function,

$$p(r) := \gamma(r)r^2 \quad (.19)$$

the scattering intensity of a randomly oriented ensemble of molecules in an ideal solution can be written as:

$$I(q) = 4\pi \int_0^{D_{max}} p(r) \frac{\sin(qr)}{qr} dr \quad (.20)$$

The $p(r)$ function can be extracted from the equation (20) via Fourier Transformation and results in,

$$p(r) = \frac{1}{4\pi} \int_0^{q_{max}} I(q) qr \sin(qr) dq \quad (.21)$$

This distance distribution function gives how frequently a distance r_k appears within the scattering molecule. Thus, it provides direct structural information of this molecule.

The Guinier Approximation

As showed in the derivation of the Debye equation, the scattering intensity function $I(q)$ can be expressed by the equation:

$$I(q) = 4\pi \int_0^{D_{max}} p(r) \frac{\sin(qr)}{qr} dr \quad (.22)$$

Starting from this, the $\frac{\sin(qr)}{qr}$ in (22) can be expressed by a series expansion.

$$I(q) = 4\pi \left\{ \int_0^{D_{max}} p(r) dr - \frac{q^2}{3!} \int_0^{D_{max}} p(r) r^2 dr + \dots \right\} \quad (.23)$$

In analogy with mechanics the radius of gyration (R_g) is defined as the second moment of the distance distribution function (in mechanics: of the mass distribution).

$$R_g^2 = \frac{1}{2} \frac{\int_0^{D_{max}} p(r) r^2 dr}{\int_0^{D_{max}} p(r) dr} \quad (.24)$$

Using this, the equation (23) can be written in terms of the R_g -values:

$$I(q) = 4\pi \int_0^{D_{max}} p(r) dr \left\{ 1 - \frac{R_g^2 q^2}{3!} - \dots \right\} \quad (.25)$$

The integral over the $p(r)$ function acts only as a multiplicative factor, and is equal to the boundary value of the scattering intensity for $q \rightarrow 0$.

$$I(q = 0) = \lim_{q \rightarrow 0} 4\pi \int_0^{D_{max}} p(r) \frac{\sin(qr)}{qr} dr = 4\pi \int_0^{D_{max}} p(r) dr \quad (.26)$$

Thus, equation (25) can be further simplified, and the series expansion in (23) results in the equation::

$$I(q) = I(0) \left\{ 1 - \frac{R_g^2 q^2}{3!} - \dots \right\} \quad (.27)$$

For small values of ($R_g q$), the series expansion in (27) can also be written as an exponential by neglecting the terms of higher order. From this procedure the **Guinier approximation** for the inner part ($q \rightarrow 0$) can be obtained.

$$I(q) = I(0) e^{-\frac{(R_g q)^2}{3}} \quad (.28)$$

From the Guinier approximation can be derived, that the inner part of the scattering function, of a molecule in ideal solution can be described as a Gaussian function.

Besides this finding, the Guinier approximation is used to obtain the radius of gyration directly out of an experimental derived scattering function. For this procedure the scattering intensity function $I(q)$ is plotted logarithmic versus the momentum transfer vector q^2 ($\ln I(q)$ vs. q^2).

$$\ln\{I(q)\} = \underbrace{\ln\{I(0)\}}_{\substack{\text{Cross section} \\ \text{with y-axis}}} - \underbrace{\frac{Rg^2}{3}}_{\text{slope}} q^2$$

In this presentation the inner part of the scattering function can be directed to fitting procedure using a straight line fit. The radius of gyration can be derived directly from the slope of the fitting function. The scattering intensity at $q=0$ is given by the cross section of the fit function with the y-axis.

Protein Purification Procedure

The procedure was developed and enhanced by Dipl. Chem. Elena Manakova.

Frozen cells were thawed in ice in lysis buffer (100 mM Tris-HCl, pH 8,1, 1 mM DTT, 0,1 mM EDTA, 0,2 mg/ml PMSF, 0,02 NaN₃, 3mg/ml lysozyme). Cells were disrupted using French Pressure Cell (American instrument company, USA). The crude lysate was cleared by centrifugation (30000 x g, 1 hour-40 min, at 4 °C) and applied directly on DE-52 cellulose Servacel (Serva) column, equilibrated with 30 mM Tris-HCl pH 7,8 buffer, containing 50 mM NaCl, 1 mM EDTA, 1 mM DTT and 0,02% NaN₃. GroEL and GroES were eluted in gradient of NaCl (0-500 mM) at 250 mM and 350 mM respectively. These fractions are rather crosscontaminated. The GroEL containing fractions were 5-6 times diluted with 50 mM Tris-HCl buffer, pH 5,8 - 5,6 for two reasons: to decrease salt concentration till 50-100 mM of NaCl and to adjust pH for next chromatography.

The second chromatographic step was performed on the same column, DEAE-Cellulose, equilibrated with 25 mM His-HCl, pH 5,7, 1 mM DTT. GroEL was eluted with gradient of NaCl (0-500mM) at 300-400 mM NaCl (GroES is eluted at 200-300 mM NaCl). Pooled GroEL fractions were supplemented with 0,4 M AS and loaded on Butyl-Sepharose column (Pharmacia), equilibrated with 20 mM K-MOPS, pH 7,2, 1 mM DTT and 0,4 M SA. GroEL was eluted with long gradient (0,4 M SA - 0 M). Main part of contaminations was removed at washing step (0,4 M SA). This step is of special importance when some GroES is still present. GroES normally does not bind to this column. GroEL is eluted also at the beginning of reverse gradient.

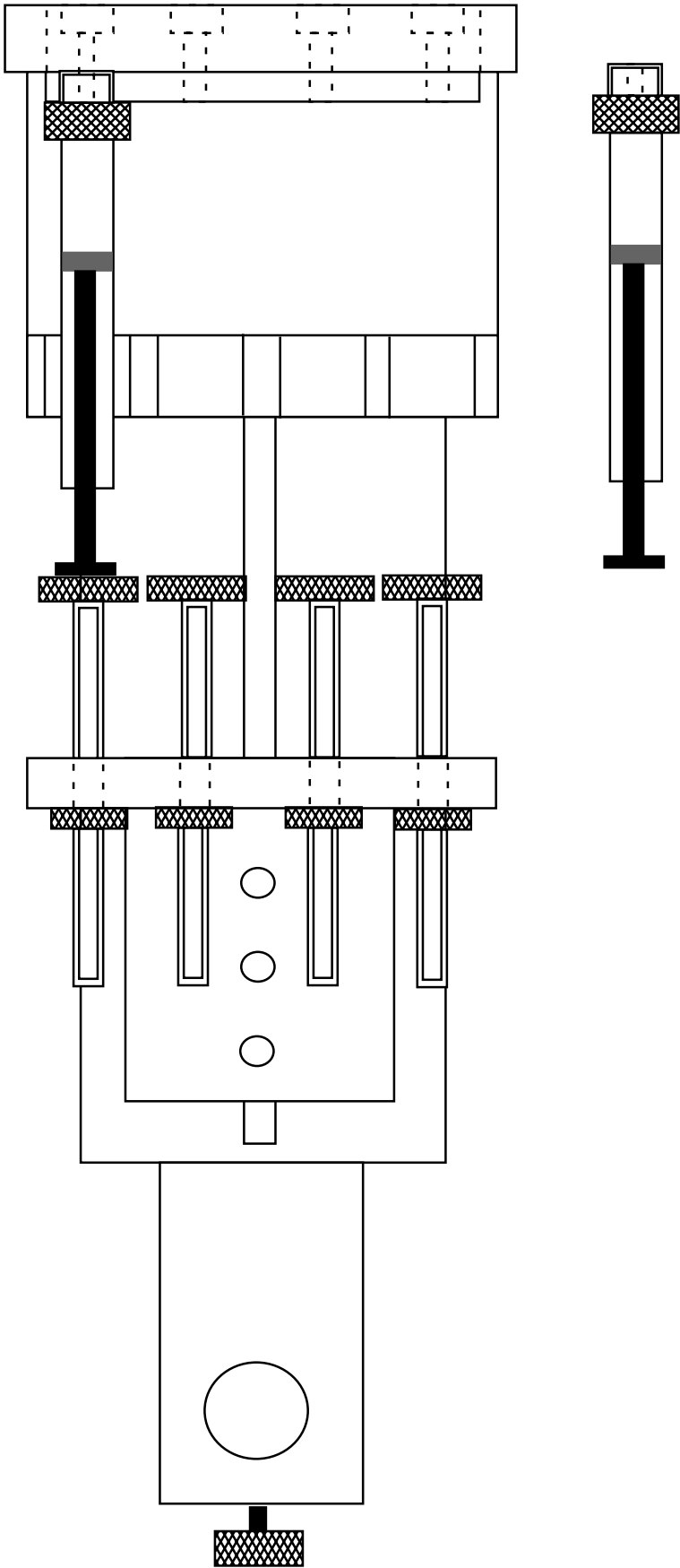
The rather diluted GroEL fractions, after the Butyl-Sepharose column, were concentrated (by ultrafiltration in Amicon stirring cell and Filtron membran with 10 kDa cut-off or with AS precipitation) and applied on gel filtration Sephacryl S-300 column (Pharmacia), equilibrated with storage buffer of choice (typically, 30 mM Tris-HCl, pH 7,8, 150 mM NaCl, 1 mM DTT, 0,1 mM EDTA, 0,02% NaN₃, 10% Glycerol). Pooled fractions of oligomeric GroEL were frozen in liquid N₂ and stored at -80 °.

Main GroES fraction, containing no or very small amount of GroEL after first DEAE chromatography were proceeded mainly as described below.

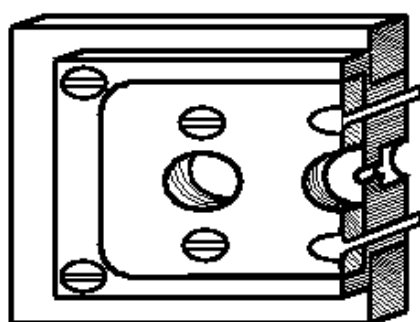
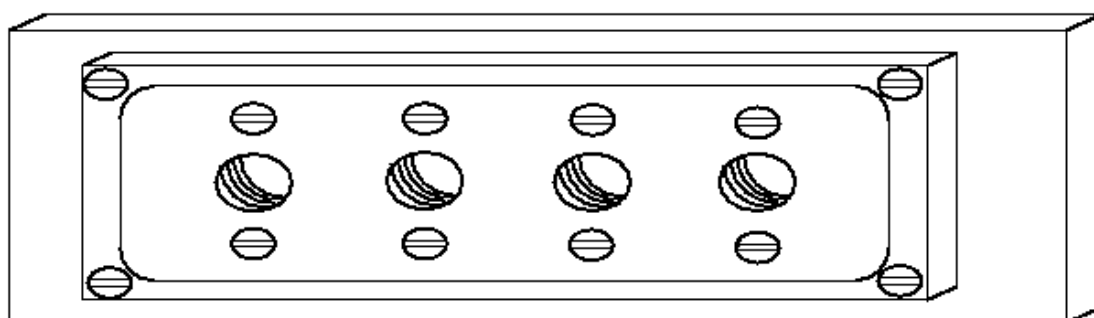
The GroES fractions were incubated at 56 ° for 20-30min. Precipitated material was removed by centrifugation (10000 x g, 1hour, at 4 °). After this treatment GroES is already about 90% pure. As a final purification step GroES solution was supplemented with 0,8 M AS and loaded on Phenyl-Sepharose column (Pharmacia) equilibrated with 20 mM K-MOPS pH 7,2, 0,8 M SA, 1 mM DTT, 0,02% NaN₃. GroES was eluted by reverse AS gradient (0,8 M - 0 M SA) as a broad peak. The GroEL binds very tightly to a Phenyl-sepharose column, it can be eluted only at salt-free washing step. After concentration (ultrafiltration with membran cut-off 10 kDa or precipitation with SA 70% of saturation) GroES was loaded of gel-filtration Sephacryl S-300 (Pharmacia) column and eluted with storage buffer of following composition: 30 mM tris-HCl, pH 7,8, 150 mM NaCl, 10% glycerol, 1 mM DTT, 0,1 mM EDTA, 0,02%NaN₃ and after concentration stored at -80 °.

Super-pure GroEL can be obtained by using an active Red agarose column (Sigma):

About 20-30 mg Of GroEL (concentration not more than 10 mg/ml) was applied on the column about 50 ml. Column at room temperature was thoroughly (> 500 ml) washed with 20 mM K-MOPS, pH 7,5, containing 10 mM MgAc₂. When protein completely entered the gel, column was leaved closed for 20 minutes. Then protein was eluted with 2 column volumes of buffer, pooled, concentrated, supplemented with salt (at least 50 mM), DTT, NaN₃ and glycerol, controled for purity and stored at -80°. Important is not to exceed GroEL concentration 10 mg/ml. It might start to aggregate after elution. But can be rescued by adding NaCl about 100-200 mM.



Linerarvorschub mit Spritzenaufnahme		
Masstab: ca. 1:2	21.03.98	
	MPI Biochemie	M. Rößle
Material: ISEL Linearvorschub 600mm Aluminium mit Teflon Spritzenaufnahme		



Spritzenaufnahmekopf zur Montage auf Linearvorschub		
Masstab: ca. 1:2	21.03.98	
	MPI Biochemie	M. Rößle
Material: Teflonblock mit Aluminiumgewinde einsatz und Halterung aus Aluminium zum Einsatz mit Hamilton AccuDill-Spritzen auf ISEL Linearvorschub		